

POLITECNICO DI TORINO

Master of Science in Petroleum and Mining Engineering



Application of in-hole camera and photogrammetry to create calibrated discrete fracture networks and obtain the in-situ block size distribution of a rock mass to blast

Supervisor:

Prof. Cardu Marilena

Tutor:

Maurizio Bernardini

Candidate:

Stefano Zocca

Academic year 2020-2021

Ringraziamenti

Ho sognato a lungo questo momento.

Prima di tutto vorrei ringraziare le due persone che hanno reso possibile la stesura di questa tesi. La prima persona è la professoressa Marilena Cardu, per la sua continua disponibilità e per avermi ispirato a intraprendere questo percorso di studi. La seconda è Maurizio Bernardini, vorrei ringraziarlo per l'incredibile dedizione verso il suo lavoro e per avermi aiutato in ogni momento di difficoltà durante la realizzazione di questo progetto.

Un grazie va alla mia fidanzata, che mi ha insegnato che nulla è impossibile se lo si vuole veramente.

Un grosso grazie va ai miei amici, che hanno reso ogni giorno migliore. Nei momenti più difficili e duri della mia vita ci siete sempre stati, non lo dimenticherò mai. Non importa dove andremo a lavorare e quante volte ci vedremo in un anno, sono sicuro che nulla tra noi cambierà.

Desidero ringraziare mio fratello, che mi ha spinto ogni giorno a dare il meglio e a raggiungere questo traguardo. La bontà che mette in tutto ciò che fa è qualcosa che ho sempre ammirato, spero che non la perda mai.

Un ringraziamento va anche a tutti i miei parenti, chi è presente e chi non c'è più. Ognuno a modo suo ha contribuito nel raggiungimento di questo traguardo.

Questo successo voglio però dedicarlo a mia madre, che ogni giorno ha creduto in me. Tutti i sacrifici che ha fatto in questi anni mi hanno permesso di diventare quello che sono e se avrò successo nella vita sarà solamente grazie a lei.

Vorrei anche ringraziare Golder Associates per aver incluso gli autori di questo progetto nel programma di licenze accademiche di FracMan® 7.90 suite.

Acknowledgement

I have long dreamed of this moment.

First of all, I would like to thank the two people who made the writing of this thesis possible. The first person is Professor Marilena Cardu, for her continuous availability and for having inspired me to undertake this course of study. The second person is Maurizio Bernardini, I would like to thank him for his incredible dedication to his work and for helping me in every moment of difficulty during the realization of this project.

Thanks go to my girlfriend, who taught me that nothing is impossible if you really want it.

A big thank you goes to my friends, who have made every day better. In the hardest and most difficult times of my life you have always been there, I will never forget that. Doesn't matter where we will work and how many times we will see each other in a year, I'm sure nothing between us will change.

I would like to thank my brother, who pushed me every day to do my best and to reach this goal. The kindness he puts into everything he does is something I have always admired, I hope he never loses it.

A thank you also goes out to all my relatives, those who are present and those who are gone. Each in their own way has contributed to the achievement of this goal.

However, I want to dedicate this success to my mother, who believed in me every day. All the sacrifices she has made in these years have allowed me to become what I am and if I succeed in life it will be only thanks to her.

I would also like to thank Golder Associates for including the authors of this project in the FracMan® 7.90 suite academic licensing program.

Index

Figure index	4
Table index	7
1 Introduction	8
1.1 Slim project	9
1.2 El Aljibe quarry	10
1.3 Geology of the area	11
1.4 Description of the campaigns	13
1.5 Thesis objectives	14
2 Theoretical concepts	16
2.1 Discontinuities	16
2.2 Stereographic projection	21
3 Methods	24
3.1 Televiewer	24
3.1.1 Equipment	25
3.1.2 Procedures for acquisition data	31
3.1.3 Principles	34
3.1.4 WellCAD analysis	36
3.1.5 Structure features	44
3.1.6 Limitations	48
3.1.7 Results	48
3.2 Photogrammetry	51
3.2.1 Equipment	51
3.2.2 Procedures for acquisition data	51
3.2.3 Principles	52
3.2.4 Limitation input data	53
3.2.5 Data analysis	54
3.2.6 Results	58
3.3 Outcrop measurement	59
3.4 FracMan software	60
3.4.1 Definitions	60
3.4.2 Input data	61
3.4.3 Data analysis	66
3.4.3.1 ISIS analysis	66

3.4.3.2	Spacing	69
3.4.3.3	Linear fracture intensity	71
3.4.3.4	Areal fracture intensity	73
3.4.3.5	Trace length analysis	74
3.4.4	Model simulation	77
3.4.4.1	Region box definition	77
3.4.4.2	Iterations	77
3.4.4.3	Fracture generations	79
3.4.4.4	P₂₁ Calibration	82
3.4.4.5	P₁₀ Calibration	83
3.4.4.6	Results	85
3.4.4.7	Model generation	89
3.4.5	In-situ block size distribution (IBSD)	91
3.4.5.1	Results	93
4	Conclusions	95
5	References	97
6	Sitography	98
	Appendix A	
	Appendix B	

Figure index

Figure 1: Image of El Aljibe quarry after the two blast campaigns.

Figure 2: Almonacid de Toledo [Map, 2021].

Figure 3: El Aljibe quarry (Arno company) [Arno,2020].

Figure 4: First: Dominant fault rock lithologies function of the stress regime [Segarra, 2018].
Second: Temperature/pressure diagram with different facies [Metamorphic, 2021].

Figure 5: Conceptual flow-chart of the thesis.

Figure 6: Geometrical properties of discontinuities.

Figure 7: Dip angle and dip direction [WellCAD].

Figure 8: From top to bottom: total spacing, set spacing, normal set spacing.

Figure 9: Persistence of the fracture.

Figure 10: Bilinear shear criterion for discontinuities [Hack, 2003].

Figure 11: Equatorial nets [Rockmechanics].

Figure 12: Polar nets [Rockmechanics].

Figure 13: Stereographic representation of density poles without areal distortions.

Figure 14: Head of the televiewer with the centralisers entering in a borehole [Gomes,2017]

Figure 15: General aspect of the QL40 OBI-2G [User Guide OBI, 2017].

Figure 16: Optical assembly and principle of measurement [User Guide OBI, 2017].

Figure 17: Fixed centralizer [Gomes,2017].

Figure 18: Mini-winch and controller [Gomes,2017].

Figure 19: Mini-winch and tripod [Gomes,2017].

Figure 20: BBox acquisition tool [Gomes,2017].

Figure 21: Starting depth [Gomes,2017].

Figure 22: Command window [Gomes,2017].

Figure 23: Logger Program [Gomes,2017].

Figure 24: planar representation of a discontinuity [WellCAD].

Figure 25: Graphical representation of the influence of the calliper [WellCAD].

Figure 26: Measuring of the dip direction [WellCAD].

Figure 27: Window to open different image.

Figure 28: WellCAD image at the beginning of the analysis.

Figure 29: WellCAD image, minimum value of the scale.

Figure 30: Apparent to true dip and Azimuth.

Figure 31: On the left the discontinuity, in the middle the marked trace and on the right the correct trace.

Figure 32: Image of WellCAD at the end of the analysis.

- Figure 33: Projection of the planes.
- Figure 34: Discontinuous fracture marked.
- Figure 35: Continuous fracture marked.
- Figure 36: Open fracture marked.
- Figure 37: Discontinuous fracture marked.
- Figure 38: Internal structure marked.
- Figure 39: Filing material marked.
- Figure 40: Presence of water in hole.
- Figure 41: Void.
- Figure 42: Weakness area marked.
- Figure 43: Stereo projection first campaign televiewer.
- Figure 44: Stereo projection second campaign televiewer.
- Figure 45: Instruments: Canon EOS70D camera (left) and six targets (right) [Bernardini, 2019].
- Figure 46: Data acquisition [SfM,2021].
- Figure 47: Scheme of photogrammetry acquisition [Bernardini, 2019].
- Figure 48: Model of the considered surface [Bernardini, 2019].
- Figure 49: Trimmed and referenced 3D model [Bernardini, 2019].
- Figure 50: Manual mapping of the joint sets [Bernardini, 2019].
- Figure 51: Automatic cluster assignment [Bernardini, 2019].
- Figure 52: Stereographic projection first campaign (photogrammetry).
- Figure 53: Stereographic projection second campaign (photogrammetry).
- Figure 54: Stereographic projection outcrop.
- Figure 55: Position and inclination of the borehole (first campaign on the left and second campaign on the right).
- Figure 56: Overall view of the boreholes location (first campaign in green and second campaign in red).
- Figure 57: Discontinuities imported in the boreholes.
- Figure 58: Borehole with outcrop discontinuities (P1).
- figure 59: Imported surfaces.
- Figure 60: Borehole generated with the discontinuity's surfaces.
- Figure 61: Imported tracemaps.
- Figure 62: Stereographic projection first campaign with boundaries defined by the user.
- Figure 63: Stereographic projection second campaign with boundaries defined by the user.
- Figure 64: Real length, measured length, distance first last joint.
- Figure 65: Surfaces taken into consideration in calculation [Bernardini,2020].
- Figure 66: log- normal distribution from trace length analysis, first campaign.
- Figure 67: log- normal distribution from trace length analysis, second campaign.

Figure 68: Region box containing all the objects.

Figure 69: Set Random Seed Tool.

Figure 70: Fracture from different sets with same seed.

Figure 71: Fracture set definition window.

Figure 72: Generation model of the set fracture.

Figure 73: Fracture properties.

Figure 74: Set properties.

Figure 75: Fractures dimensions.

Figure 76: Iteration to reach less than 5 % of error.

Figure 77: P_{10} in function of the radius (mean and deviation).

Figure 78: P_{21} in function of the fractures.

Figure 79: P_{10} in function of the fractures.

Figure 80: Graph P_{10} - P_{21} .

Figure 81: Model simulation with P_{21} value first campaign.

Figure 82: Model simulation with P_{10} value first campaign.

Figure 83: Model simulation with P_{21} value second campaign.

Figure 84: Model simulation with P_{10} value second campaign.

Figure 85: Graph equivalent spherical diameter (log-log).

Figure 86: Fracture simulation with P_{21} values (From top left to bottom right: Sh, ShNE, SvSE, SvNE).

Figure 87: Fracture simulation with P_{10} values (From top left to bottom right: Sh, ShNE, SvSE, SvNE).

Figure 88: Fracture simulation with P_{21} values (From top left to bottom right: Sh, ShNE, SvSE, SvNE).

Figure 89: Fracture simulation with P_{10} values (From top left to bottom right: Sh, ShNE, SvSE, SvNE).

Table index

Table 1: Number of holes mapped during the acquisition data.

Table 2: Structure table.

Table 3: Data extracted from WellCAD analysis (Borehole 1, 6th blast).

Table 4: Total Discontinuities.

Table 5: Value inserted during the analysis.

Table 6: Position of outcrops measurement (European terrestrial reference system).

Table 7: Limit of each family defined by the user.

Table 8: Data relative to the ISIS analysis (first campaign).

Table 9: Data relative to the ISIS analysis (second campaign).

Table 10: Spacing result first campaign.

Table 11: Spacing results second campaign.

Table 12: P_{10} measured first campaign.

Table 13: P_{10} measured second campaign.

Table 14: Total area surfaces.

Table 15: P_{21} measured first campaign.

Table 16: P_{21} measured second campaign.

Table 17: Length and radius first campaign.

Table 18: Length and radius second campaign.

Table 19: P_{21} calibration.

Table 20: P_{21} calibration.

Table 21: P_{10} calibration.

Table 22: P_{10} calibration.

Table 23: Mean value of calibration fractures.

Table 24: Test with different radius.

Table 25: Input value for MDS analysis.

Table 26: Median and maximum diameter for the two type of detection for each campaign.

Table 27: All values of P_{21} Analysis.

Table 28: All values of P_{10} analysis.

Table 29: All values of spacing analysis.

1 Introduction

This thesis was carried out thanks to a collaboration between the Polytechnic of Turin and the School of Mines and Energy of the Technical University of Madrid (UPM). The study was carried out in the El Aljibe quarry near Almonacid de Toledo (Spain), a quarry used for the extraction of aggregates. The data of this study was carried out during the European project "SLIM", funded by the European Union with a budget of 6,979,200 euros involving 13 EU partners (Section 1.1). The first part of this study is to describe the functioning and analysis of the borehole optical televiewer data. For this purpose, field data from in-hole photography obtained with optical televiewer for 11 line of blasthole were analysed. The acquisition of the image of the holes were carried out during two different campaigns. The second part of this study is to describe the functioning and the acquisition methods with the photogrammetry. The acquisition of the photogrammetry data was carried out simultaneously with the data acquisition of the borehole optical televiewer. Only the images acquired in hole were directly analysed in this study, while for the photogrammetry the data were processed in the study "Application of LiDAR and photogrammetry methods at El Aljibe quarry (Toledo, Spain) to characterize the rock mass for fragmentation prediction in rock blasting through Kuz-Ram and xp-frag models" [Bernardini, March, 2019]. The calculations also used manually measured discontinuity data taken on natural outcrops outside the excavation area. This data, after being processed and filtered, were used for the processing of in-situ block size distribution. This was calculated using the FracMan [FracMan 7.90] program developed by Golder Associate Inc which allows the construction of a Discrete Fracture Network (DFN). The software, after data input, allows the generation of a 3D model that represents, as accurately as possible, the conditions of the analysed rock mass. The models were generated through a careful calibration using the linear fracture intensity P_{10} (derived from the televiewer analysis) and the areal fracture intensity P_{21} (derived from photogrammetry). Then, the four different models generated were used to define the volume distribution of the rock blocks generated by the fracture intersection. Finally, using a MATLAB [MATLAB, 2019] filter (used to transform volume distribution into equivalent diameter distribution), the in-situ block size distribution for both campaigns and methods was generated.



Figure 1: Image of El Aljibe quarry after the two blast campaigns.

1.1 Slim project

The SLIM project ("*Sustainable Low Impact Mining solution for the exploitation of small mineral deposits based on advanced rock blasting and environmental technologies*") is a 48-months European project under the Horizon2020 programme (starting in 2016, under grant agreement No.730294).

Thirteen different European partners were involved in this study (Austria, Denmark, Sweden, France and Spain) and the mines and quarries of Toledo, Granada (Spain) and Eisenerz (Austria) were the subject of study and testing field for new technologies. The SLIM project was developed thanks to the partner organizations 3GSM, Benito Arno and Hijos, Bureau de Recherches Géologiques et Minières, VA Erzberg GmbH, Gate2Growth, Luleå Tekniska Universitet, Maxam Corp. International, Minpol GmbH, Montan Universität Leoben, Minera de Orgiva, Technische Universitaet Graz and ZABALA Innovation Consulting and coordinated by the School of Mines and Energy of the Technical University of Madrid (Universidad Politécnica de Madrid).

The aim of the project is to increase extraction from small deposits on the European continent through the development of low cost and low environmental impact mining solutions. This goal has been achieved through the study of rock cluster fragmentation. A new generation of explosives and an advanced automatic explosion design model will be applied for the intended purpose.

1.2 El Aljibe quarry

The exploitation of the quarry is reserved to Benito Arnó e Hijos S.A.U. and is used for the extraction of aggregates used for the construction of high-speed and conventional trains. El Aljibe quarry is located close to Almonacid de Toledo (Castilla-La Mancha, Spain), a small town far 100 km from Madrid (Figure 2).



Figure 2: Almonacid de Toledo [Map, 2021].

El Aljibe quarry is an open-pit quarry of metamorphic rocks (mylonite) and was fundamental for the construction of the high-speed train way in Spain.

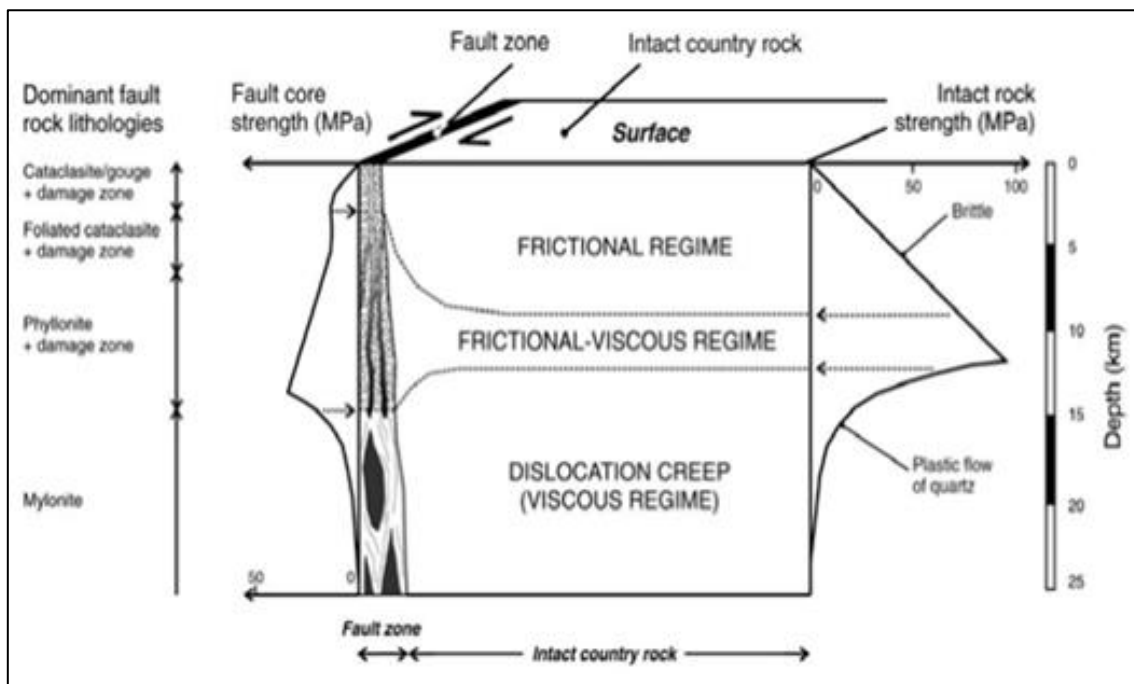
The products that are extracted, processed and marketed are ballast for high-speed and conventional trains (fraction 32/56 mm), for high-strength concrete and asphalt mixes (fraction 6/12 mm), and for substrates and base tracks (fraction 0/25 mm) in road and track construction.



Figure 3: El Aljibe quarry, (Arno company) [Arno, 2020].

1.3 Geology of the area

The aggregates extracted from the El Aljibe quarry were formed during the final tectonic event in the Hercinian Orogeny which generated a ductile shear zone [Enrile, 1981]. This zone generated mylonite and cataclasmite. The pressure and temperature conditions (450° C and 0.4 GPa) generated the mylonite bringing the migmatite into amphibolite facies conditions (Figure 4).



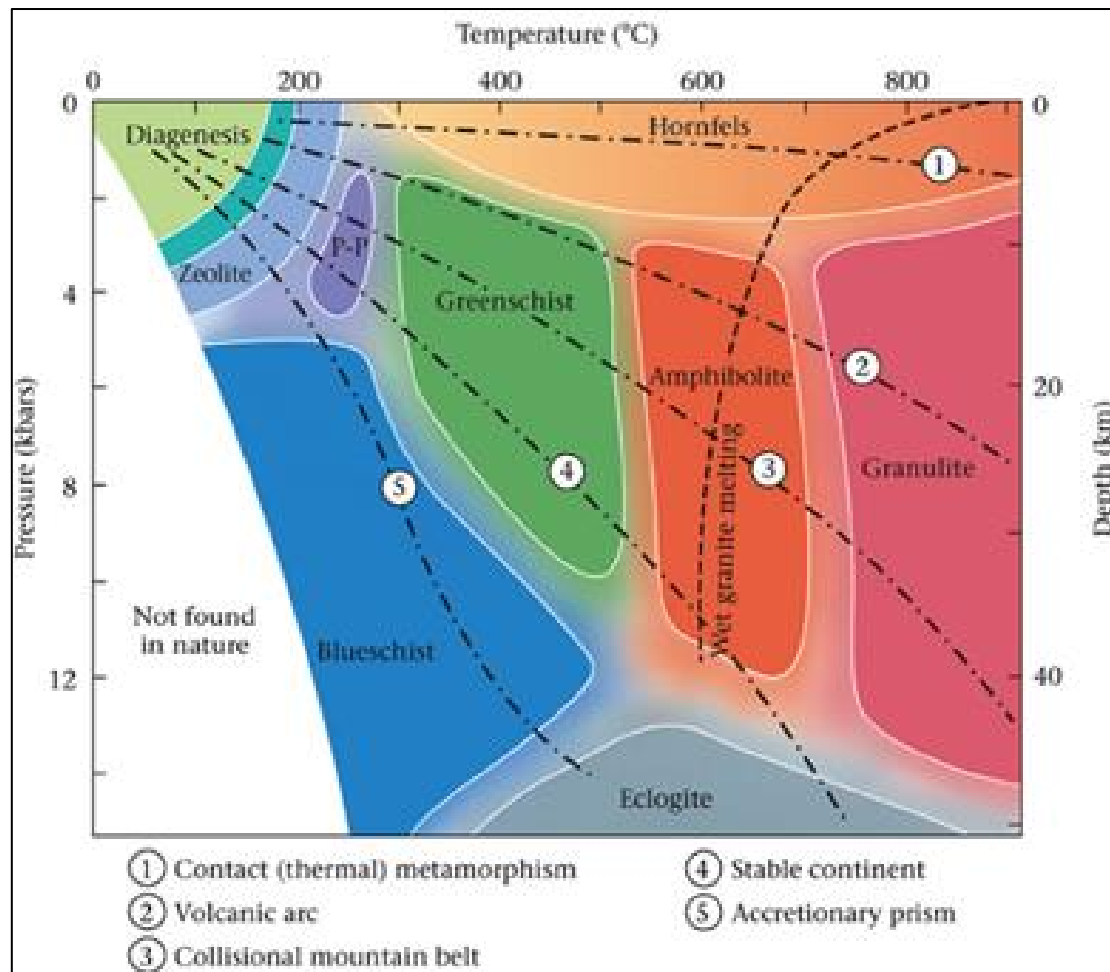


Figure 4: First: Dominant fault rock lithologies function of the stress regime [Segarra, 2018].

Second: Temperature/pressure diagram with different facies [Metamorphic, 2021].

In the quarry there are present:

- **Ultramyylonite:** a rock that has undergone considerable grain reduction, composed of quartz and mica. The ultramyylonite is hard, dark and can resemble pseudotachilite and obsidian.
- **Protomyylonite:** mylonite that has undergone a limited grain reduction, therefore generated at the first stages of deformation, containing more than 50 % porphyroclasts. Since mylonitisation is not complete, it can present rock fragments (sharped) and crystals immersed in a fine-grained matrix.
- **Orthomyylonite:** it is developed in ductile shearing of granites in the initial stages. Contain around 25 % of porphyroclasts with a fine siliceous matrix.
- **Ultracataclasite:** has a breccia texture, without foliation and with siliceous composition (quartz and feldspars).

At the extraction point of the quarry orthomyylonite is the most present.

1.4 Description of the campaigns

The data collection of the campaigns was carried out during the extraction process. Before the mine holes were loaded with explosives, they were mapped using the televiewer camera. During the drilling process for the blast, control holes were drilled to detect damage to the rock mass. The holes in each blast were 89 mm in diameter, drilled on 12 m benches, with a spacing and burden of 3 m and each image from the televiewer has a different length, due to the presence of water or obstruction. Two different data acquisition campaigns were carried out, in Table 1 the actual number of images from the televiewer analysed in the study is shown.

Table 1: Number of holes mapped during the acquisition data.

	N° blasthole	N° Televiewer hole
Blast 1	7	5
Blast 2	7	5
Blast 3	Broken window	Broken window
Blast 4	5	2
Blast 5	5	2
Blast 6	4	2
Blast 7	5	1
Blast 8	5	3
Blast 9	7	3
Blast 10	5	4
Blast 11	6	4
Blast 12	6	4

The acquisition of the images using the photogrammetry method was carried out pre-blast. The technique of photogrammetry is based on the use of images (to which a position is assigned) to generate a 3D model of the free surface. In order to have a real model the images were taken from different positions, to compensate for the possibility of blind spots.

1.5 Thesis objectives

The objective of this study is to define the block size distribution of a rock mass. The data were collected in two campaigns of 6 blasts each at El Aljibe quarry. The investigation work is based on two different techniques: digital photogrammetry and borehole optical televiewer. In this way, the rock mass can be modelled through a DFN built using the statistical values of the discontinuity sets visible on the highwalls (photogrammetry) and on the wall of the boreholes (optical televiewer). Through an analysis of the images detected in the field, it is possible to trace the number of fractures that can characterize the rock mass. In this study, the images from the camera of the televiewer were analysed through the WellCAD [ALT, 2017] program. The photogrammetry data come from a study carried out previously in the same extraction site [Bernardini, 2019]. Moreover, fracture data from manual surveys carried out on natural outcrops that present outside the quarry have been considered for the statistical analysis of the sets. An effective result is generated by comparing two different methods, which present advantages and different limitations. The method of digital photogrammetry is reliable but has limitations due to the detection of discontinuities only on the outcrop surface. On the other hand, the acquisition with the televiewer allows a better knowledge of the “inside” of the rock mass, but at the same time it provides data only on the fractures that intersect the boreholes and does not provide information about fracture length. Both have limitations due to the arbitrariness of the data analysis performed, because each fracture must be traced manually. The difference in the number of fractures traced depends on the different sampling scale and the different resolution of image acquisition (televiewer allows an analysis with a GDS resolution of 1 mm while photogrammetry allows a resolution of 8.5 mm). Therefore, the model values generated will be a representation of the same rock mass with different scales and errors. One of the aims of this study will be also to define a methodology for the use of the programs and the calibration of the parameters to be included in the software.

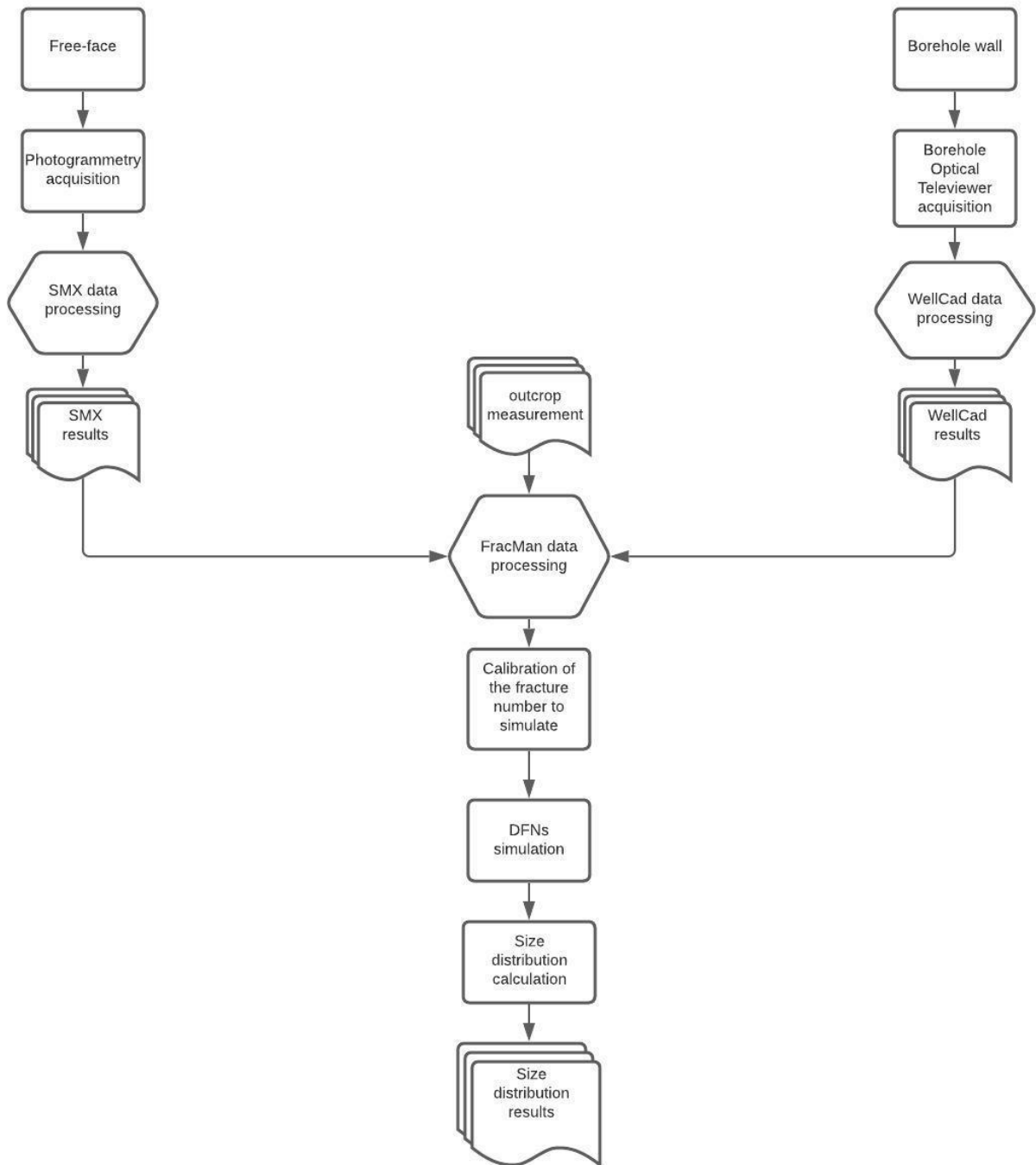


Figure 5: Conceptual flow-chart of the thesis.

2 Theoretical concepts

The rock masses that present on the earth's surface are for the most partly discontinuous and therefore largely conditioned in their mechanical behaviour by discontinuities. The mechanical behaviour depends on the contribution of the interaction of the intact rock and the discontinuities within it. The greater heterogeneity and anisotropy of intact rock generates better mechanical properties of the rock mass resulting discontinuities as planes of weakness. The characterization of a rock mass is divided into several phases: it starts with laboratory tests to measure the mechanical parameters on a small scale and reaches the real parameters through the rock mass classification technique. The scale effects are not negligible in rock masses. The main processes that generate discontinuities usually lead to a decrease in the mechanical properties of the rock mass. Discontinuities such as joints and faults are defined as relevant discontinuities, while discontinuities such as foliations or grain segregation, due to metamorphic processes, are defined as integral discontinuities (they do not generate a relevant decrease in mechanical properties)[Slob,2010] . Pre-existing fractures define an alteration of the compact rock that may cause a change in the direction of the stress regime. Due to this reason, the in-situ block size distribution is a key parameter for an optimised blast design.

The size and shape of the rock blocks are due to the number of discontinuities, their orientation, their persistence and the number of intersections that are generated. In fact, many parallel planes can influence the overall characteristics less than a smaller number of discontinuities but with a favourable orientation.

2.1 Discontinuities

The forces applied on the rock mass over long periods of time can have different effects, for example they can generate deformation and distortion or if they exceed the strength of the rock materials, they can give rise to fractures. In all cases, several factors, with chemical and physical nature, affect the resulting of the deformation [Slob,2010]:

- The magnitude of the strain forces
- Temperature
- The confining pressure
- The rate at which the deforming forces are applied
- Pore pressure due to the presence of fluids
- The rate at which the deformation proceeds
- Composition of the rock and pore fluids

In order to make blast a fundamental aspect is identify and define the characteristics of the discontinuities.

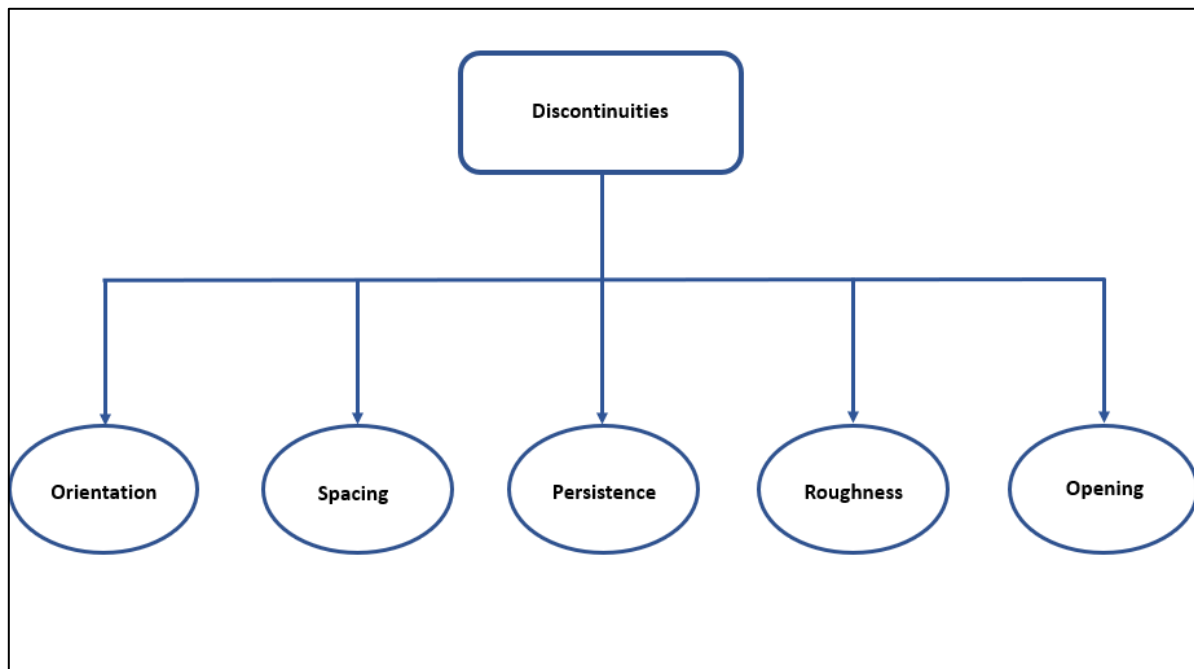


Figure 6: Geometrical properties of discontinuities.

The following characteristics are representative of a rock discontinuity:

Orientation: is given by two different angles, known as dip angle and dip direction. The orientation as a property by itself does not influence the mechanical behaviour of a rock mass [Slob,2010], but becomes important for the stability during the excavation. Discontinuities characterised by similar values of orientation belong to the same "family". The dip angle is defined between the horizontal plane and the discontinuity plane, while the dip direction is defined as the azimuth value, with clockwise rotation respect to the North of the projection of the discontinuity plane on the horizontal plane. If the plane of a fracture surface is defined, its orientation can be readily determined.

The dip direction is defined as the positive angle from the North direction and it ranges between 0° and 360° while the dip angle between 0° (horizontal planes) and 90° (vertical planes). Values greater than 90° generates an inversion of the immersion of the discontinuity. The plane orientation is always defined by the two angles, dip direction/dip angle (for example a horizontal plane can be written as 120/00). The data can then be plotted using polar or equatorial hemispheric projections (section 2.2).

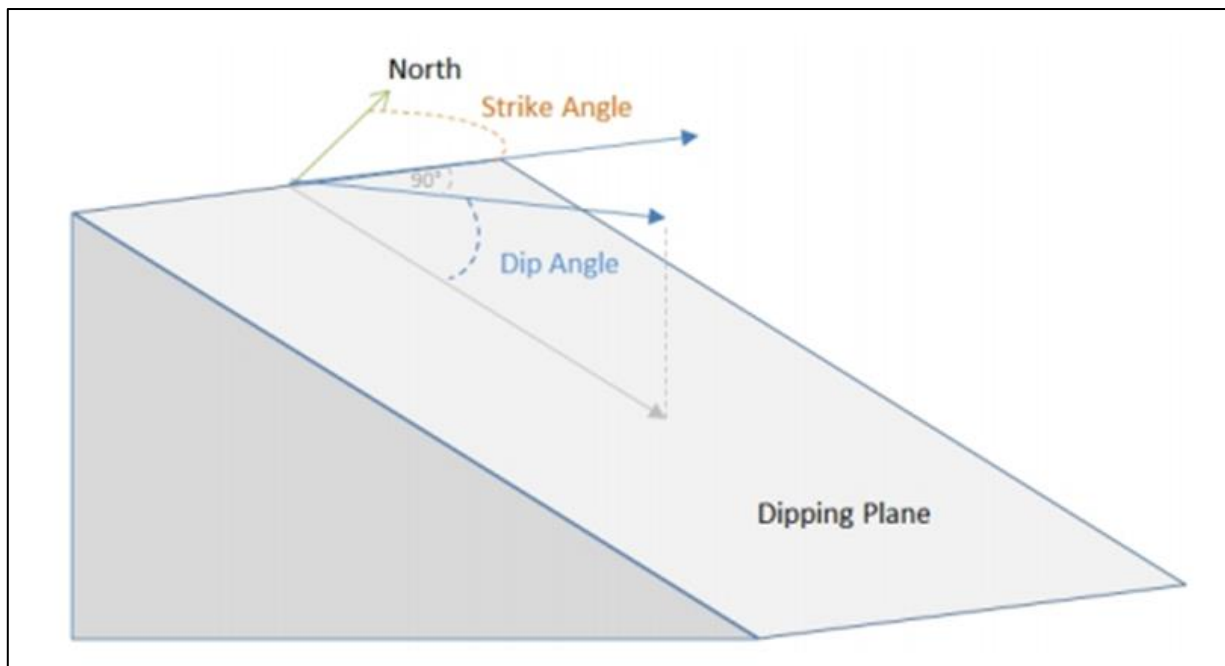


Figure 7: Dip angle and dip direction [WellCAD].

Spacing: defines the distance between the different discontinuities providing a trend in the mechanical behaviour of the rock mass and a maximum block size. The combination of spacing and orientation data is very important to define a block size distribution value.

Since the discontinuity planes are not parallel to each other, three different measurement methods can be defined: *total spacing*, *set spacing* and *normal set spacing* [Slob,2010]. The total spacing gives a generic indication about the rock mass fracturing and is defined the distance between a pair of immediately adjacent discontinuities measured along a scanline. The set spacing define the distance between a pair of immediately adjacent discontinuities from a particular set discontinuity, and when is measured along a scanline that is perpendicular to the average orientation it is called normal set spacing.

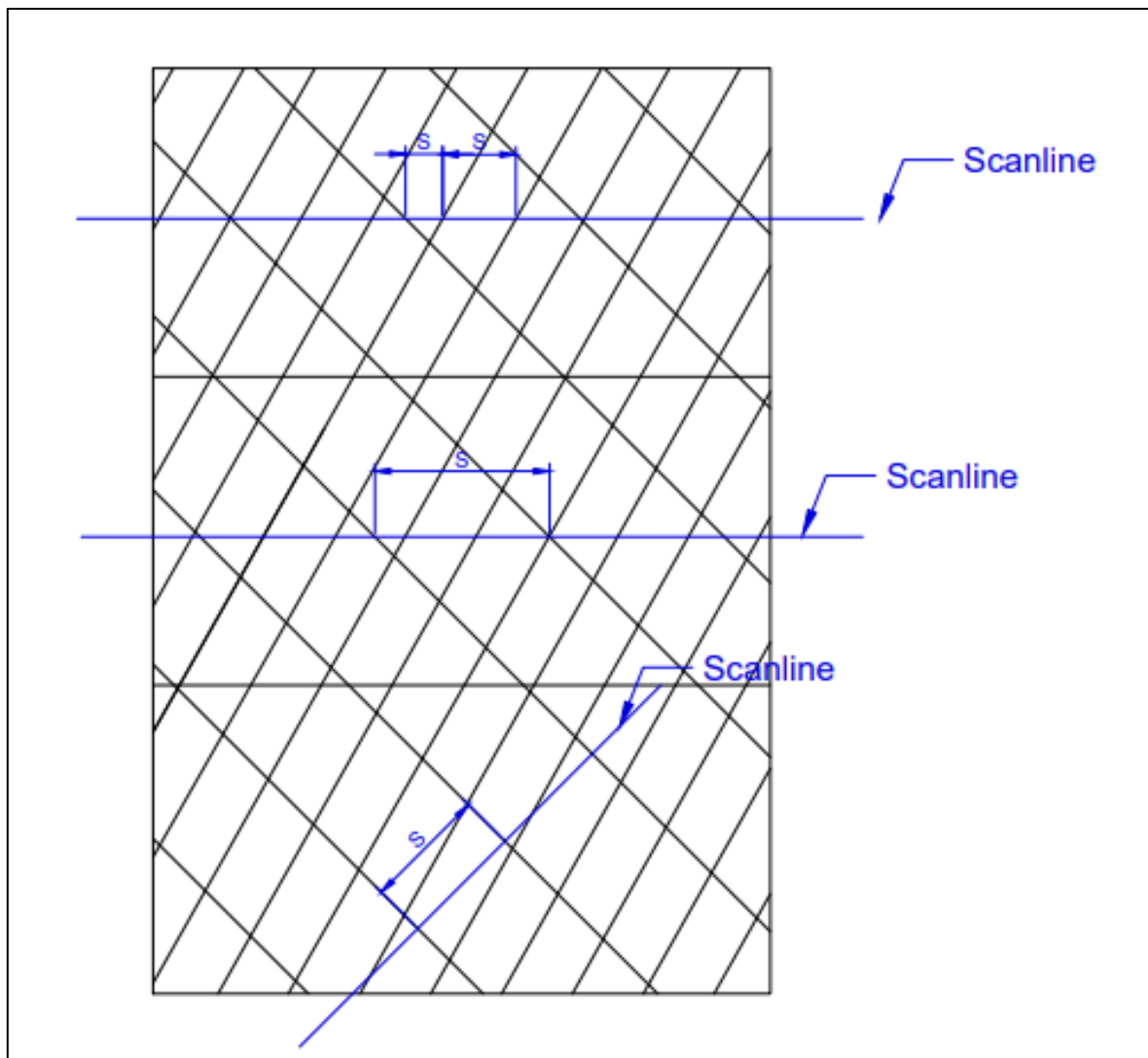


Figure 8: From top to bottom: total spacing, set spacing, normal set spacing.

Persistence: is the length of the discontinuity trace in all the directions. The discontinuities are distinguished according to their termination: discontinuities extending for all the length of the exposed rock (persistent discontinuities), discontinuities ending in the intact rock (non-persistent discontinuities) and discontinuities ending against other discontinuities (abutting discontinuities). The orientation, spacing and persistence of the discontinuities condition the shape and size of the blocks determined by the intersection of the different families of fractures.

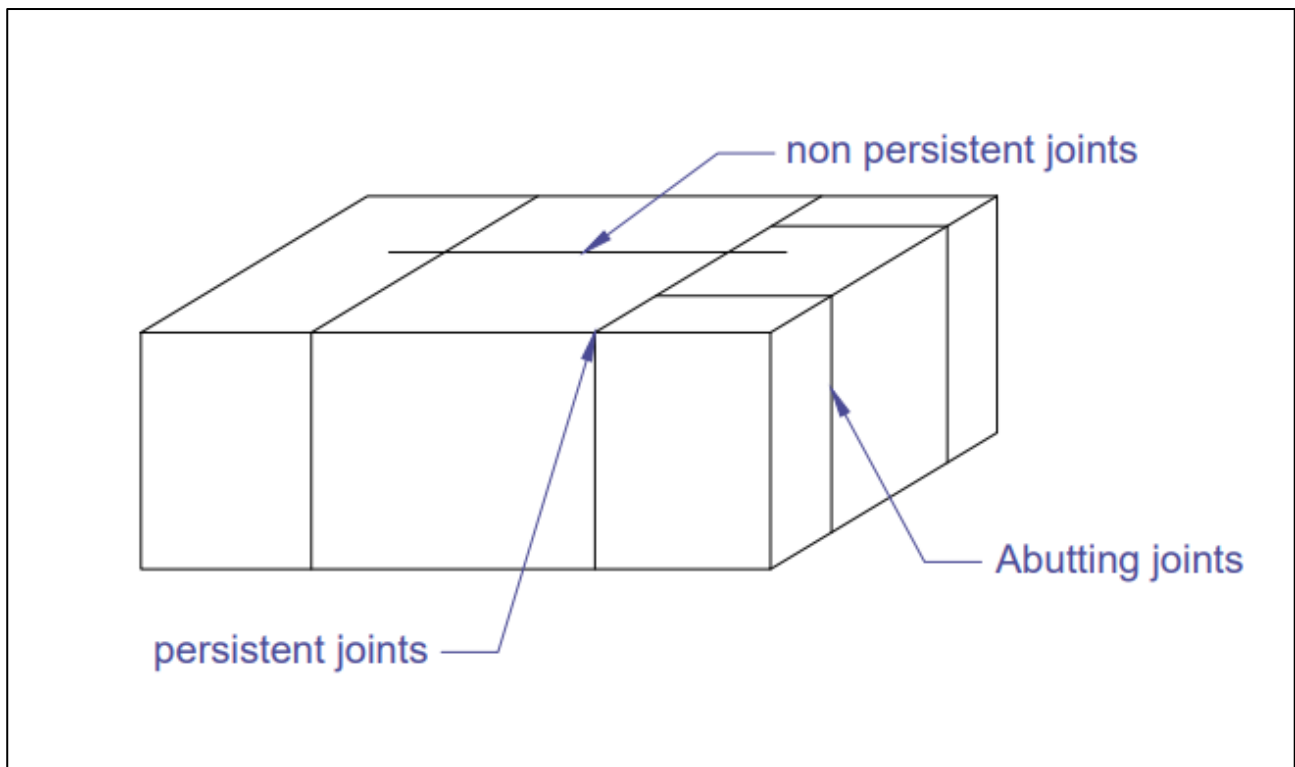


Figure 9: Persistence of the fracture.

Roughness: is used for to assess shear strength along discontinuities without cohesion, which can be estimated from data collected in the campaign and empirical formulas. The term roughness is used to refer to the undulation of the surfaces of discontinuities and to small-scale irregularities, so requires two observation scales: Metric scale (flat, undulating or stepped surfaces) and millimetric scale (polished, smooth or rough surface)[Slob,2010]. The shear strength is impossible to be calculated by test on site, due to the big dimensions of the surfaces, so must be derived using the roughness. Small displacements are governed by small scale asperities, while large displacements are governed by large scale asperities (Figure 10).

Small displacement:

$$\tau = \sigma * \tan (\phi_{discwall} + i)$$

Large displacement:

$$\tau = \sigma * \tan (\phi_m)$$

Where:

- τ is the shear strength
- σ is the normal stress
- ϕ_m is the angle of friction along the discontinuity

- $\phi_{discwall}$ is angle of friction of intact rock
- i angle of roughness (only used if is governed by dilatancy, otherwise is 0)
- δ_v is the dilatancy

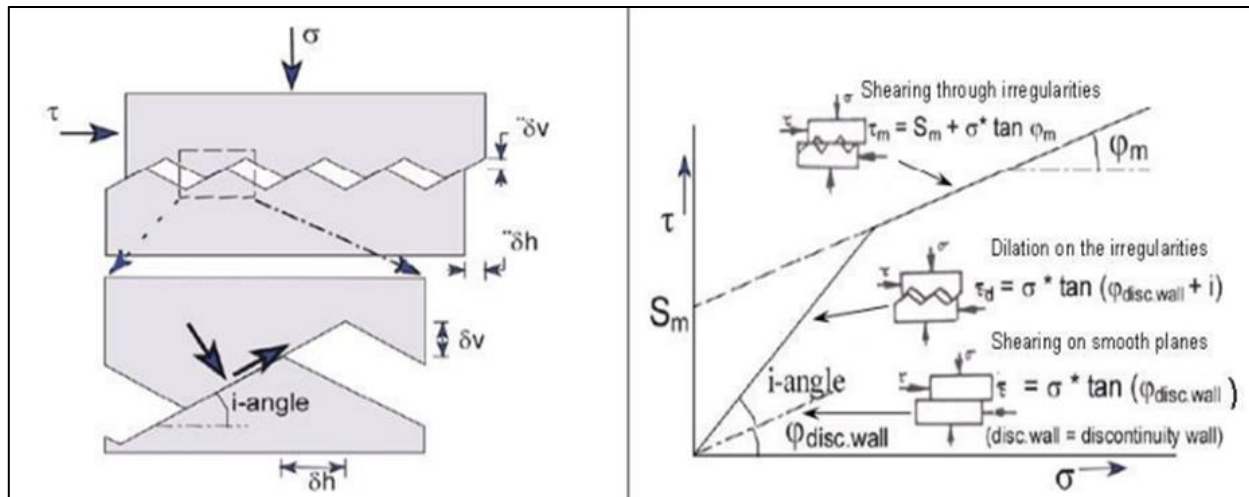


Figure 10: Bilinear shear criterion for discontinuities [Hack, 2003].

Opening: The opening of a discontinuity is the distance between its faces [Rock mechanics,2019]. The influence of the opening in the shear resistance of the joint is also important due to the presence of filling (weathered material), water and air. Displacement processes along the discontinuity can lead to considerable opening.

2.2 Stereographic projection

To represent the surface of a sphere on a plane, we need to use stereographic projections. The planes of discontinuity are projected onto a horizontal plane like poles or big circles. In this study, only the lower hemisphere will be considered due to the irrelevance of the sense of the vectors. Two different nets can be applied to represent planes or poles:

- Equatorial net: The equatorial plane in the hemisphere is positioned at an angle of 90° to the Nord-South. The equatorial grid represents the projection of the grid on the horizontal plane which dip angle with the maximum value is in the centre (90°), represented with the small circle, and the minimum value is in the external circumference (0°), represented with the great circles.

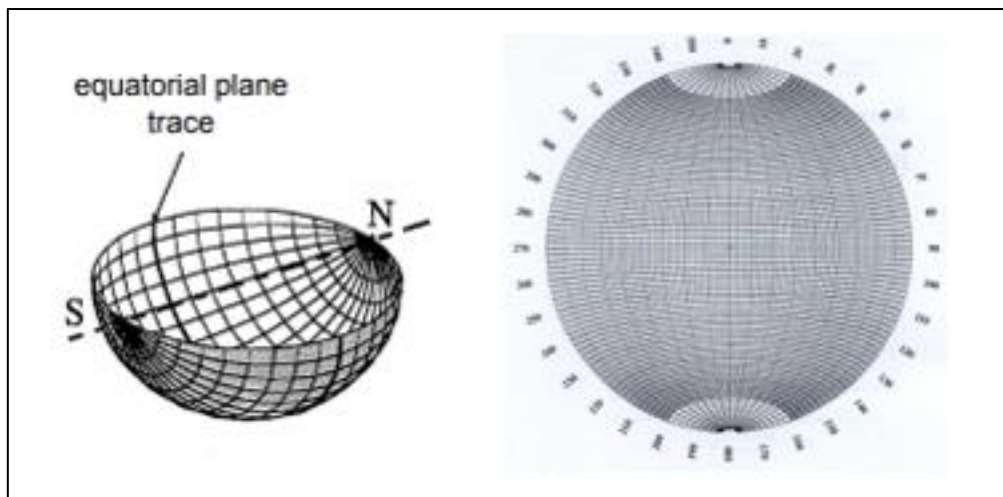


Figure 11: Equatorial nets [Rock mechanics, 2019].

- Polar net: is used for greater representation of the plane poles. The same is created by circles that are concentrating towards the centre going from the maximum value, the top outer circumference, to the minimum value, the centre of the pole.

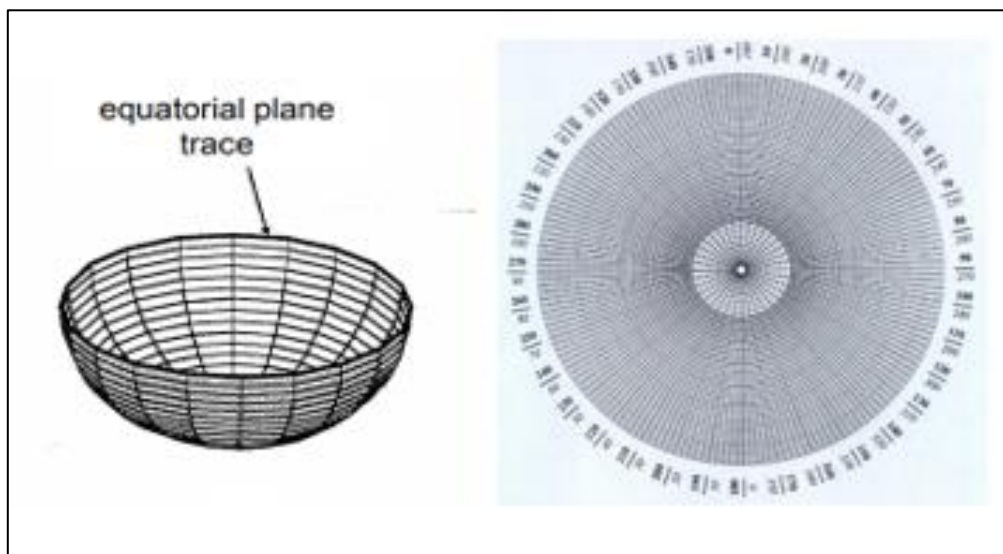


Figure 12: Polar nets [Rock mechanics, 2019].

Two different types of projections can be used to represent pole density:

- Wulff projection is mostly used for pole representation because of its ability to create equiangular representation, which results with keeping the angles undistorted. Is done by projecting the points that are in the lower hemisphere on a horizontal plane using the top pole of the sphere as its projection pole. There is a probability of a distorting the density conditions because of the sensitive areal distortion from the projection. The equiangular representation is

obtained by the intersection of the large circles with the smaller ones which always form angles of 90° .

- Schmidt/Lambert projection: is mainly used for representation of the density of the poles, because of its ability to avoid occurrence of distortion, which is a case in the Wulff projection. It is succeeded by modification of the distance between the projected point and the centre of the circle.

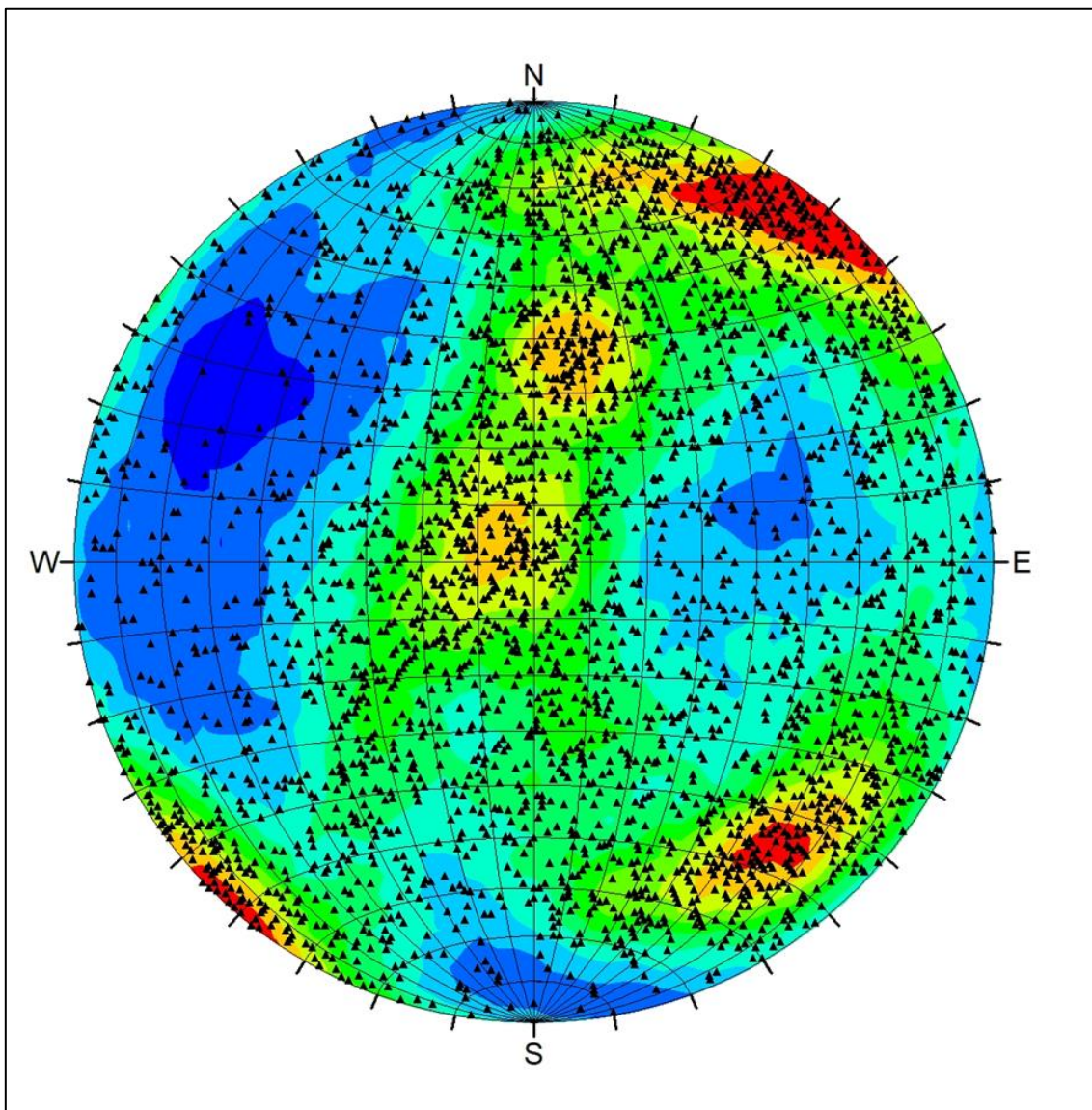


Figure 13: Stereographic representation of density poles without areal distortions.

Schmidt's projection and equatorial network are used in this study to represent the density of the poles without areal distortion.

3 Methods

The data acquisition in this study was carried out with two different procedures: *optical borehole televiewer* and *photogrammetry*. The two methods require different procedures to be performed and have different limitations. Considering both datasets, which are collected with a different sampling scales, as input for the in-situ block size distribution generation, provide a more complete result. Both methods require manual mapping of discontinuities, for this reason, the off-site analysis takes much longer than the on-site sampling operation. Then the processed data were processed by FracMan program to generate a simulated model to describe the rock mass.

3.1 Televiewer

The optical borehole televiewer is a probe with a camera capable of generating a 360° image of the internal surface of the holes. The main reasons why it is used are:

- Determine the properties of the rock mass, the distribution of the fracture, orientation and spacing between the fractures.
- Compare the results with studies carried out with other methods (in this study the photogrammetry).
- Collect accurate data to determine the in-situ rock size distribution of the blocks.
- Understand the damage suffered by the rock mass due to the blasts made for the extraction.

The images produced during the field measurements were subsequently analysed through the WellCAD program that allows to manually map the discontinuities present in each hole. No model was generated using this analysis independently, due to the fact of the inability to determine fracture persistence from borehole walls analysis.



Figure 14: Head of the televiwer with the centralisers entering in a borehole [Gomes, 2017].

3.1.1 Equipment

The optical televiwer is composed by four components:

- The logging tool
- The mini-winch with 200 m of 1/8'' wireline
- The data acquisition system
- A computer with the software ATL Logger Suite 11.2: is fundamental for data acquisition because it allows you to set the parameters for and to record the images of the walls of the hole.

Logging tool

Features of the QL40 OBI-2G quick link recording tool:

- Length: 1.47 m
- Mass: 5.3 kg
- Diameter: 40 mm
- Top part: wire connectors, centralizers which prevents the camera of touching the walls and causing damage to the televiewer
- Central part: optical deviation monitoring system
- Bottom part: image acquisition system, sensors for deflection of the hole
- Incorporates a CMOS (complementary metal-oxide-semiconductor) digital image sensor.

Is used for acquiring images of holes with a diameter of 63 mm and more because of its centralizers which are increasing the diameter, but it is not recommended to use it below a dimension of 55m diameter because of the high risk of trapping the televiewer.

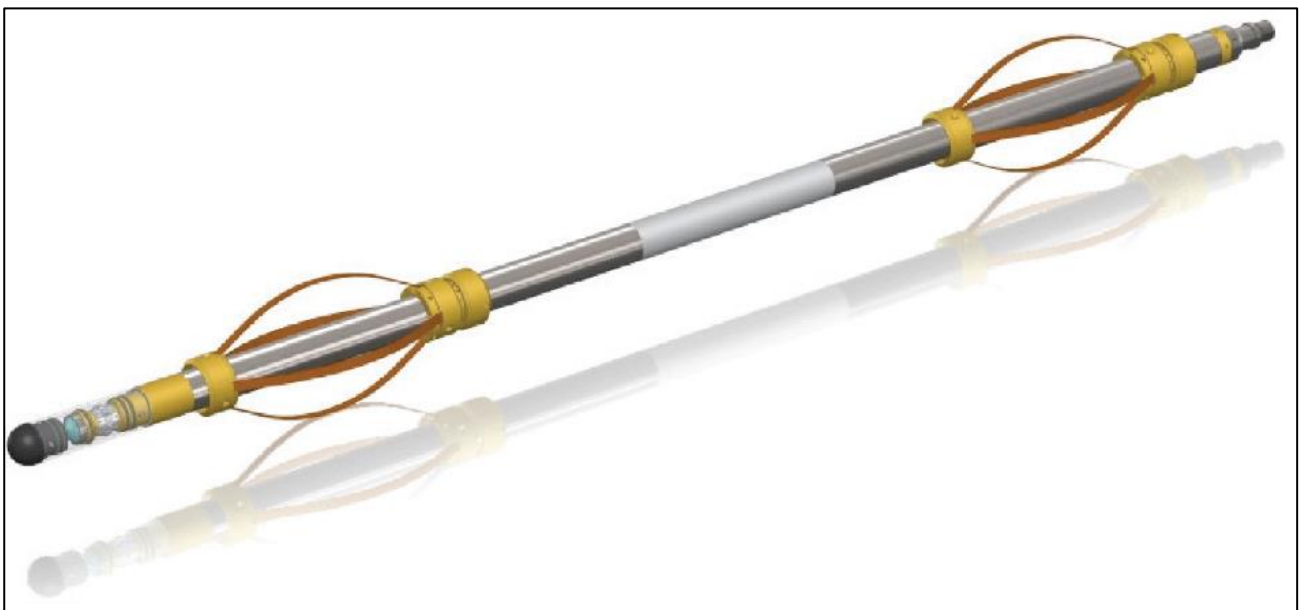


Figure 15: General aspect of the QL40 OBI-2G [User Guide OBI, 2017].

The CMOS consists of an active pixel array of 1.2 Mega Pixel and fisheye matching optics. The displayed log image is created from a single annulus extracted from the active pixel array which can be seen in Figure 16. Its light source is provided by ten LEDs and the azimuthal available resolutions are 60, 120, 180, 600, 900 and 1800 pixels/revolution [Gomez, 2017].

The optical deviation monitoring system located in the central part is composed by 3 axis magnetometers and accelerometers. The measurement's accuracy is varying between $\pm 1.2^\circ$ in the azimuth and $\pm 0,5^\circ$ in the inclination [Gomez, 2017].

The logging tool generated 360° oriented colour images by using the processed digital images in the combination with deviation data.

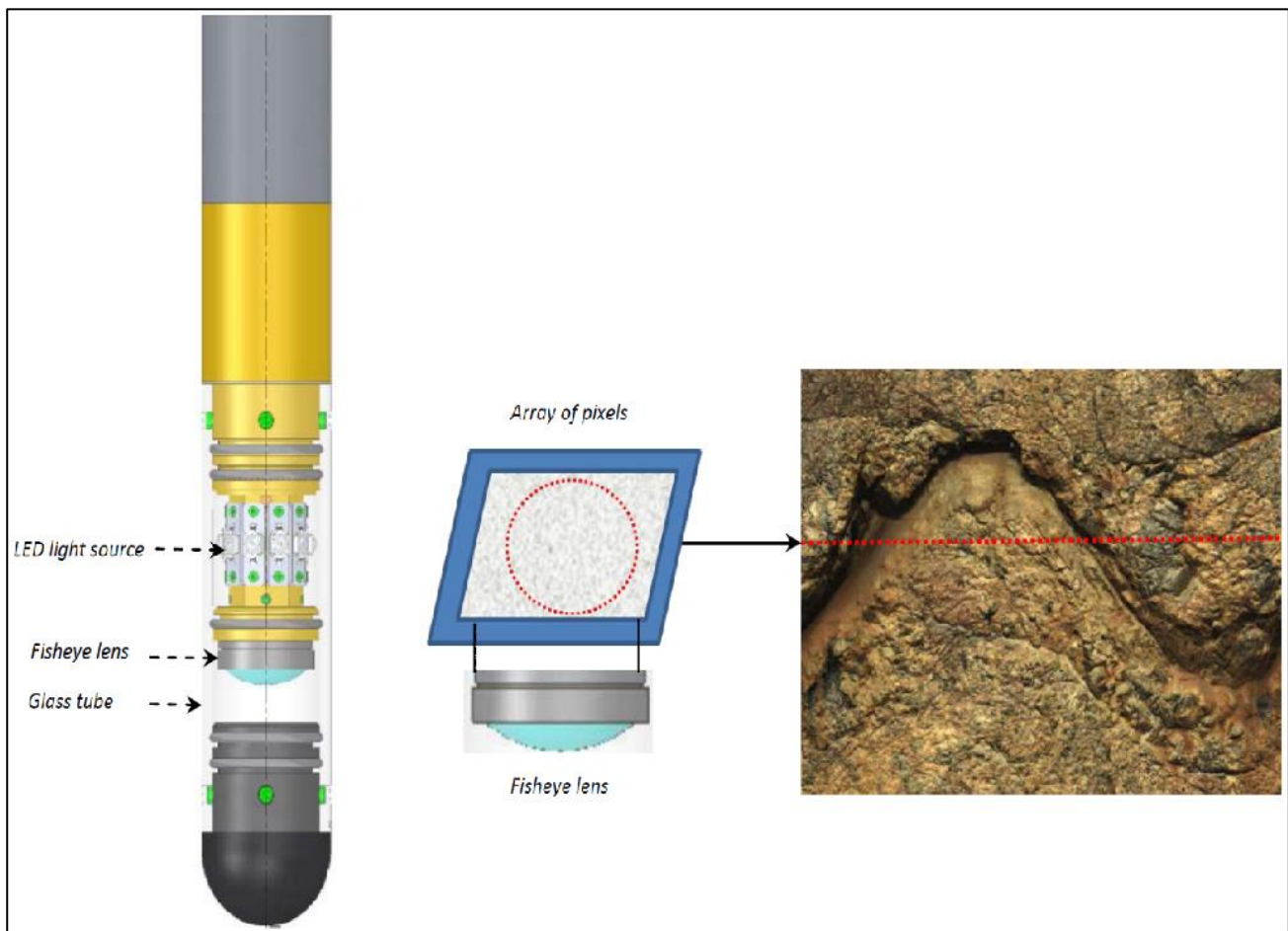


Figure 16: Optical assembly and principle of measurement [User Guide OBI, 2017].

To be positioned in the borehole, the adjustment tool must be equipped with two centralizers, one at the bottom and one at the top. It serves to ensure the most accurate coaxiality between borehole and tool.

In the El Aljibe quarry, 3" blades were used because the holes were 89mm in size. During placement, the centralizers must not be aligned with the blades so the instrument can have more points of contact with the hole wall. Each centralizer consists of two fixing rings in which 4 blades made of non-

magnetic material are placed. One ring must be fixed and the other mobile, to allow the system to compensate for irregularities in the walls of the hole.



Figure 17: Fixed centralizer [Gomes, 2017].

Mini winch

Features:

- Maximum speed: 8 m/mm
- Weight: 38kg
- Size: 66 x 46 x 46 cm
- Central part: insulated conductor covered by a steel cable which has isolating tape on the head where is connected to the logging tool

The steel cable of the insulated conductor allows data exchange between the surface and transport of energy for the instrument. It has a length of 200 m and a diameter of 0.125". The cable is wound on the drum of a mini winch, manufactured by Mount Sopris Instruments.

A tripod is used as a guideline for the wire through the borehole and the instrument allows the adjusting of the up and down speed and locking the instrument to the desired depth.

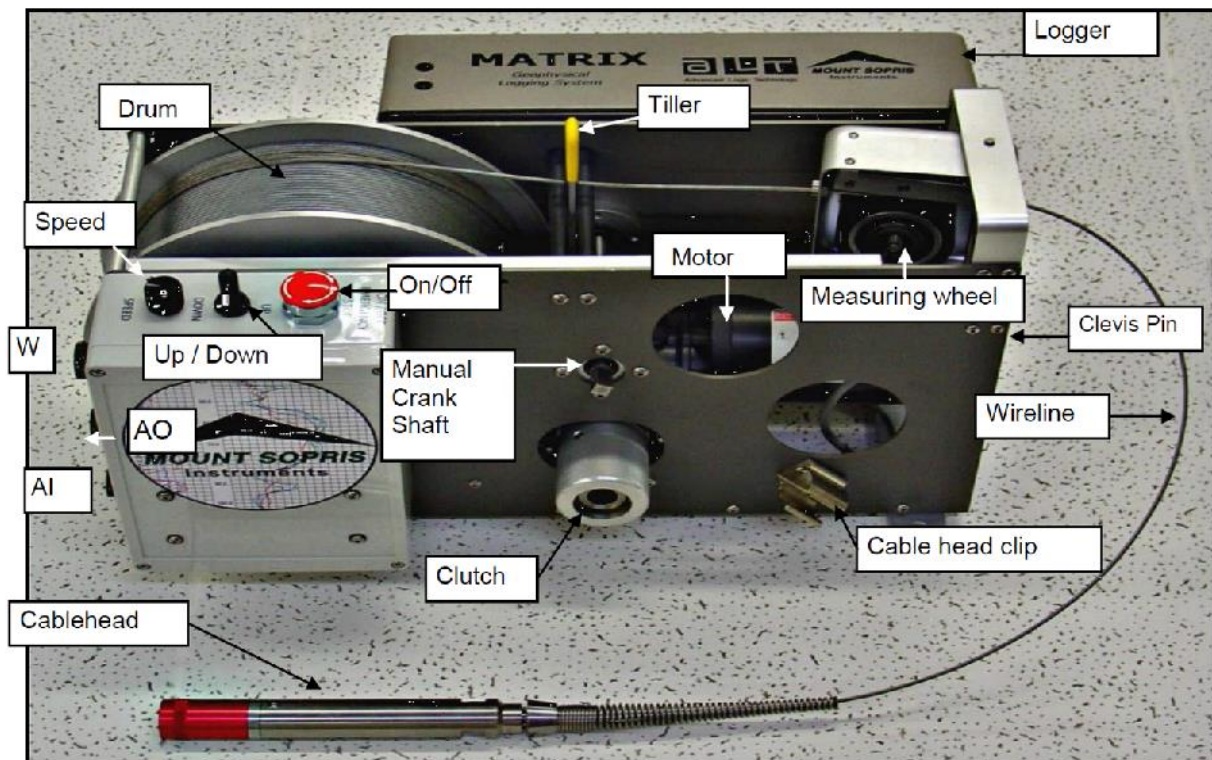


Figure 18: Mini-winch and controller [Gomes, 2017].



Figure 19: Mini-winch and tripod [Gomes, 2017].

Data acquisition system

The recording instrument is connected via the mini winch to the BBox acquisition system which connects the ATL logger suite software of the computer to the logging tool.



Figure 20: BBox acquisition tool [Gomes, 2017].

3.1.2 Procedures for acquisition data

The data acquisition of the walls of the hole usually takes about an hour in total. This time is composed of the assembly of the equipment, about 30 min, and the ascent and descent time of the instrument. With a resolution of 900 PTT the ascent speed is equal to 1 m/s, while the descent speed is equal to 2.4 m/s because carried out with a lower resolution.

The acquisition data on site follow this step:

- Place all the instrumentation near the hole to be detected. Avoid any undue stress on the wireline and place a few blocks of rock in front of the winch to keep it in place.
- Assemble the recording instrument with the mini-winch and connect it to the data acquisition system, then connect the power supply system. Each cable can be connected to a specific input, this has been done to avoid confusing the cables and increase the working time.
- Mount the tripod near the hole to be measured and secure it with stone blocks to prevent any movement. The tripod must be positioned in such a way that it does not cause unnecessary stress on the wireline.
- Prepare the instrument to be inserted into the hole. Centralizers must be mounted correctly. Then connect the instrument to the line protecting the connection with insulating tape.
- Turn on the power generator and then start the data acquisition unit. A certain length of cable must be released from the winch before starting the recording, to position the instrument close to the hole.
- Place the logging tool inside the borehole. It's important that the instrument will not touch the borehole walls, to prevent damage.
- Start the ATL Logger Suite 11.2 program in the computer.
- Connect the program with the logging tool, selecting the tool UPM – GO4-40-OBI40.
- Place the tool in the desired position, about 1.5 meters from the surface, which is the length of the probe. If the depth is not shown, use the 'zero tool' button to reset the height in the software.

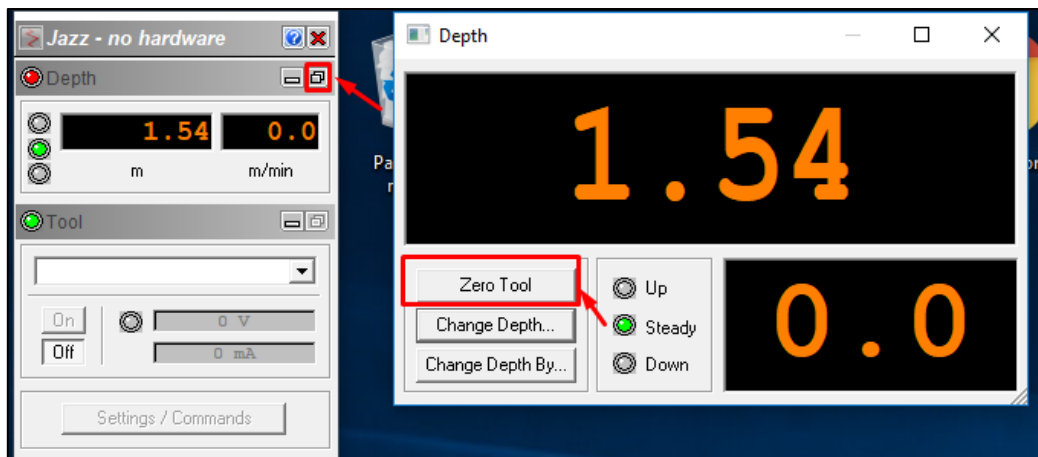


Figure 21: Starting depth [Gomes, 2017].

- Scan down by defining the light intensity, depth, resolution and azimuth. This scan will not be the one that will be analysed, since it has a lower resolution and a higher speed, but it is useful to have an idea of the parameters to be entered for recording during the ascent. When the desired height is reached, stop the winch. It is also possible to define the borehole diameter.

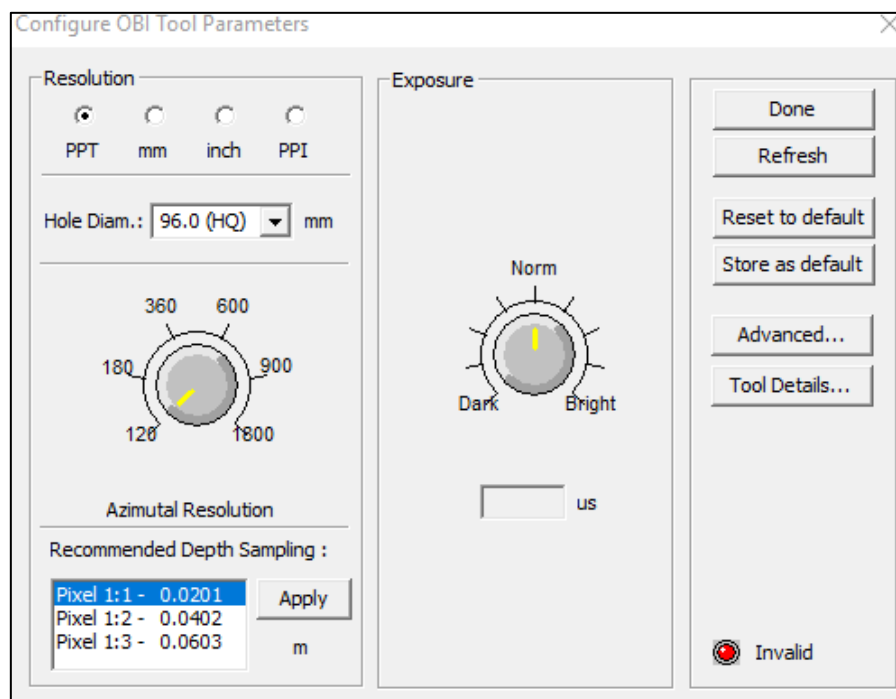


Figure 22: command window [Gomes, 2017].

- Prepare the ATL Logger Suite 11.2 program to start recording. The file was saved as “date, borehole number, starting depth off recording, direction, pixel resolution and field of view” [Gomez, 2017].

- Choose the winch speed of 1m/s, due to the high resolution (900 PPT), because you should not exceed 90 % of the workload.
- Choose the acquisition resolution at 900 PPT and brightness based on the image obtained for the previous survey, the exposure is 170-200 μ s for mylonites [Gomez, 2017].
- Once all the parameters are assigned, start the measuring record, clicking the record button.

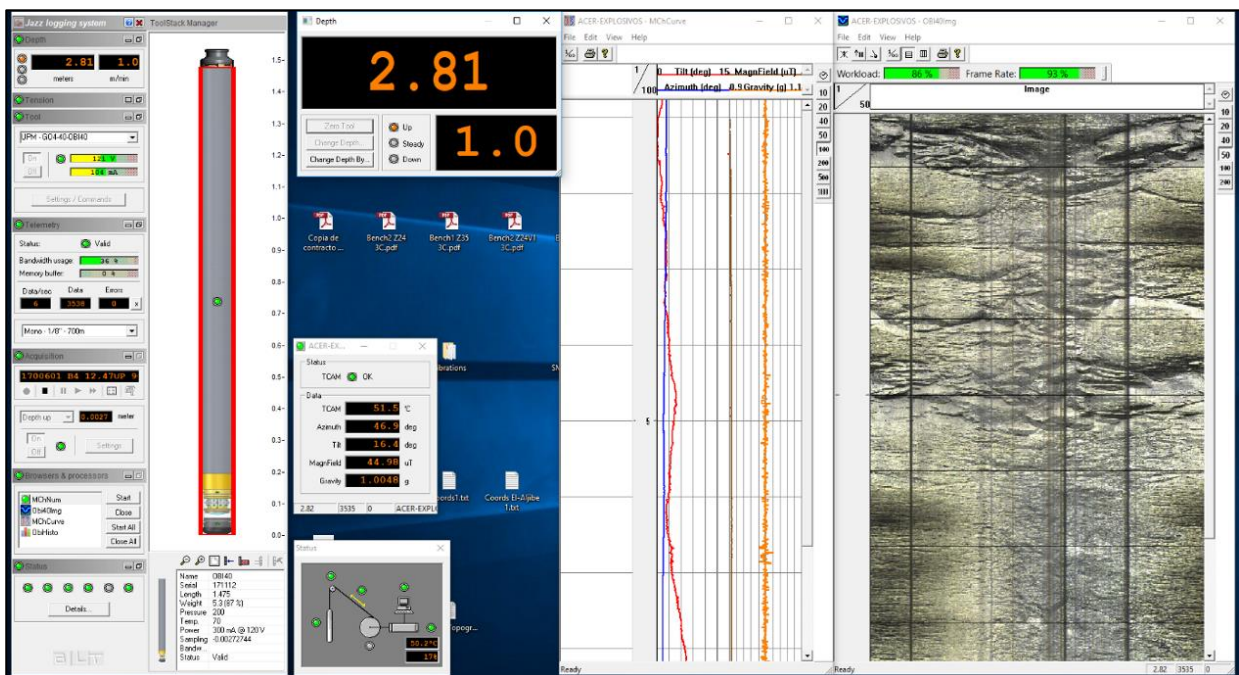


Figure 23: Logger Program [Gomes, 2017].

- Recording stops when the instrument reaches the surface.
- Cut the electric current of the televiewer, remove the televiewer from the hole and repeat the procedure for all the boreholes.

3.1.3 Principles

Image analysis is done by projecting a cylinder onto a plane. The WellCAD software "opens" the cylinder along the north direction line and projects the image of the hole walls onto a plane. The discontinuity traces, being generated by planes intersecting a cylinder, are elliptical, and when projected are defined by a sine wave. The amplitude of the sine wave is defined by the dip angle at which the discontinuity meets the hole.

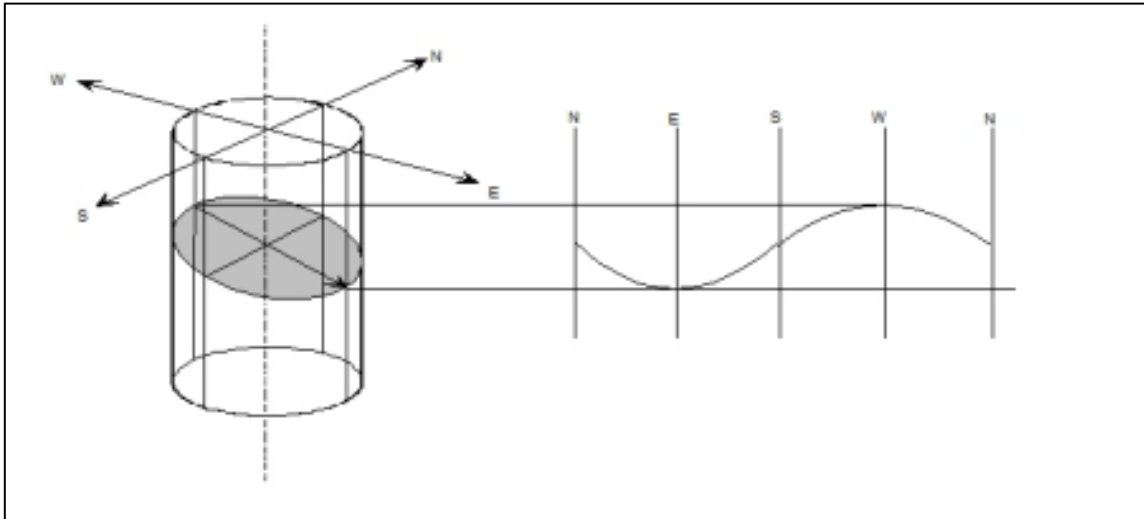


Figure 24: Planar representation of a discontinuity [WellCAD].

The immersion angle also depends on the size of the hole being mapped, and we can find it through the formula:

$$\tan \delta = \frac{\Delta Z}{cal}$$

- δ = dip angle
- ΔZ = distance between the minimum and maximum value
- cal = caliper (dimension of the hole)

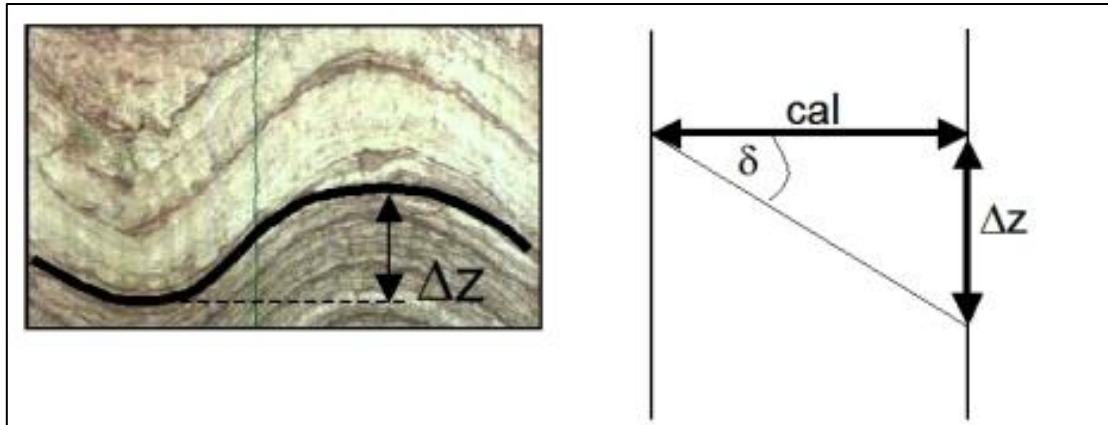


Figure 25: Graphical representation of the influence of the calliper [WellCAD].

The dip direction is calculated according to a beta angle, using the expression:

$$\beta = \begin{cases} \theta + 90^\circ, & \theta < 90^\circ \\ \theta - 90^\circ, & \theta > 90^\circ \end{cases}$$

The value of θ is the dip azimuth of the fracture.

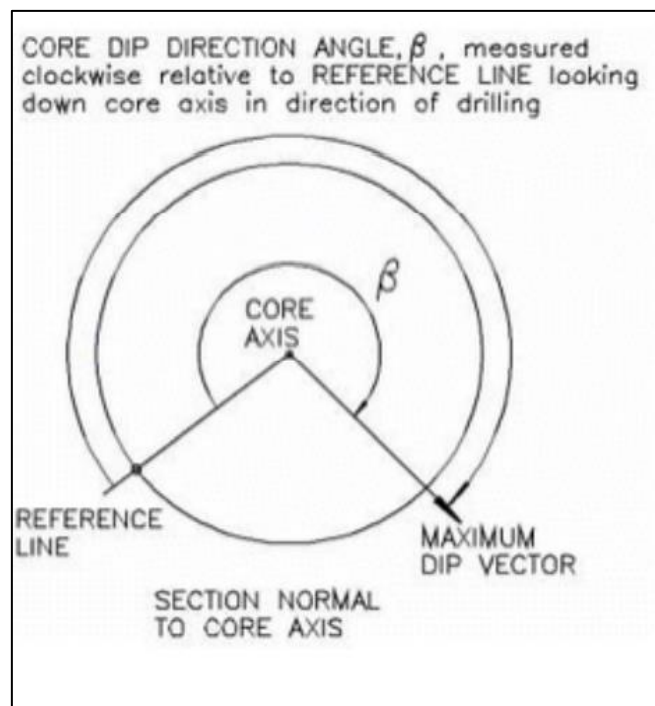


Figure 26: Measuring of the dip direction [WellCAD].

3.1.4 WellCAD analysis

WellCAD procedures

The analysis of the data collected using the televiewer camera takes place through the use of the software WellCAD (64 bit). All data were analysed following the same steps in each procedure. First, the files in *.tfd* format (logger data file) were opened using two different procedure dependent on incoming raw data:

- To open a single file, was used the Menu bar, click on *File, Import, Single file*. At this point three windows were opened, and the following parameters were chosen: Embedded to file, Depth mode and Maximum, To magnetic north, colour image and deviation.
- To open different files, due to a recording interruption due to technical problems and then creating different files containing the data to be analysed, was used the above procedure to open the first file, then was used the menu bar and was clicked on *file, import into current document, single file*. The three windows were opened again and was selected the same parameters of the single file, then a new window was opened, and were selected the parameters illustrated in Figure 27.

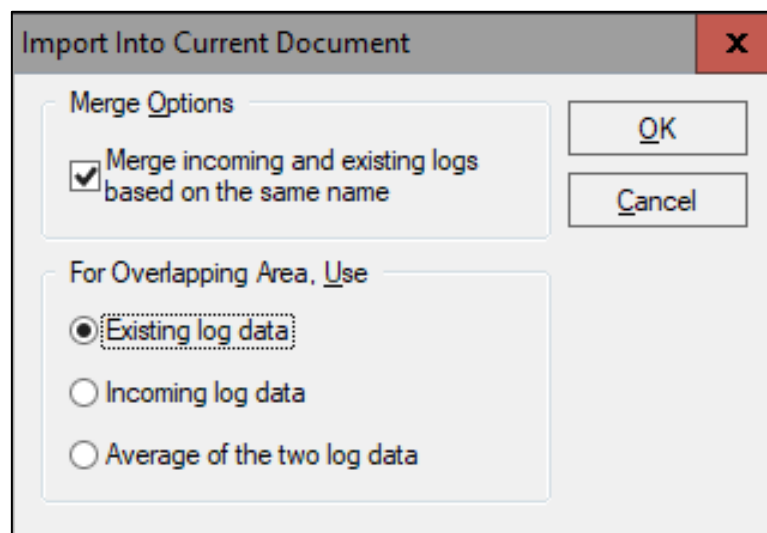


Figure 27: Window to open different image.

When the file was opened all the acquired parameters (image, tilt, magnetic field, azimuth and gravity) were shown for each depth (Figure 28).

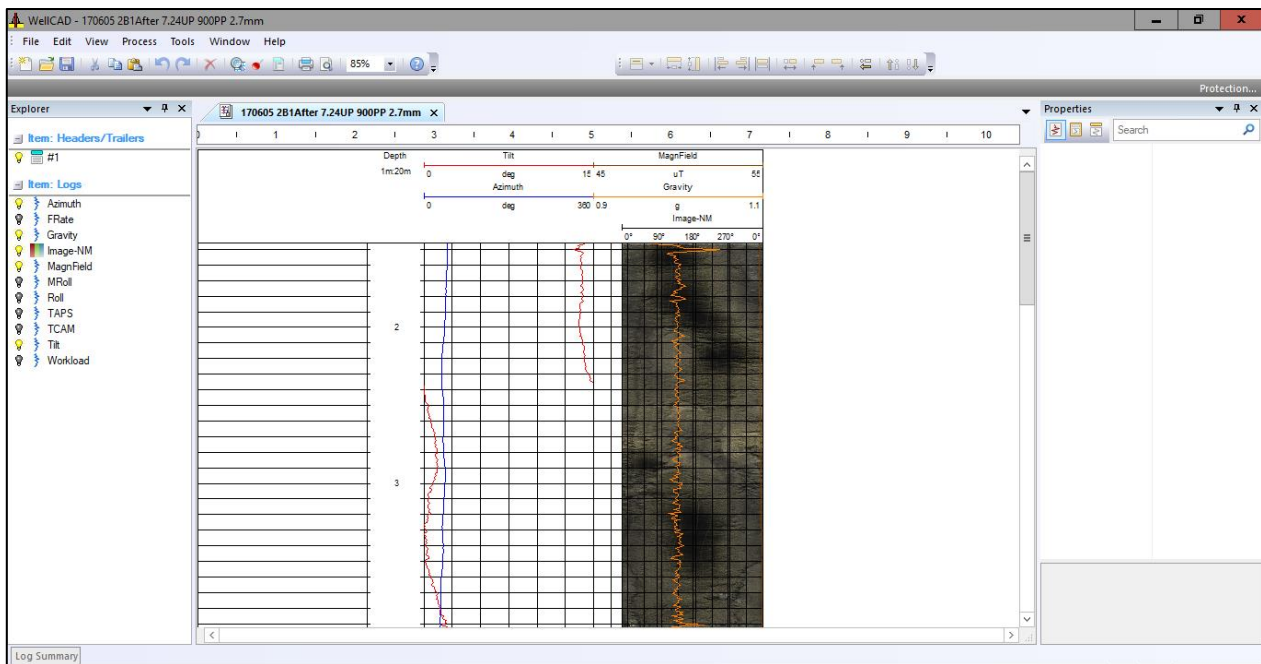


Figure 28: WellCAD image at the beginning of the analysis.

Subsequently, the following steps were followed to improve the presentation of data and thus to clarify the parameters during the analysis:

- Right click on the ruler at the top of the screen and set the values in mm
- Right click on the Depth to define the scale (the ones used were 1m:20m or 1m:10m because using different scales you do not have a clear image of discontinuities)
- Left click on the Depth and going to the Base Setting of the Properties to change the position (Left: 0, Right:15)
- Left click on Tilt and while holding down the Ctrl key, were also selected Magnetic field, Azimuth and Gravity. After with the button “*Align Left and Right*” (Document Layout menu) the logs were stacked (all Document Layout menu commands use the first selected log as a reference point)
- Left click on the Depth and while holding down the Ctrl key, were also selected Magnetic field, Azimuth Gravity and Image-NM. Using the button “*Insert After*” (Document Layout menu) logs were placed to the right of the depth.
- Left click on each parameter and in the Main Setting of the Properties the minimum and maximum values of the scale were changed (Figure 29)

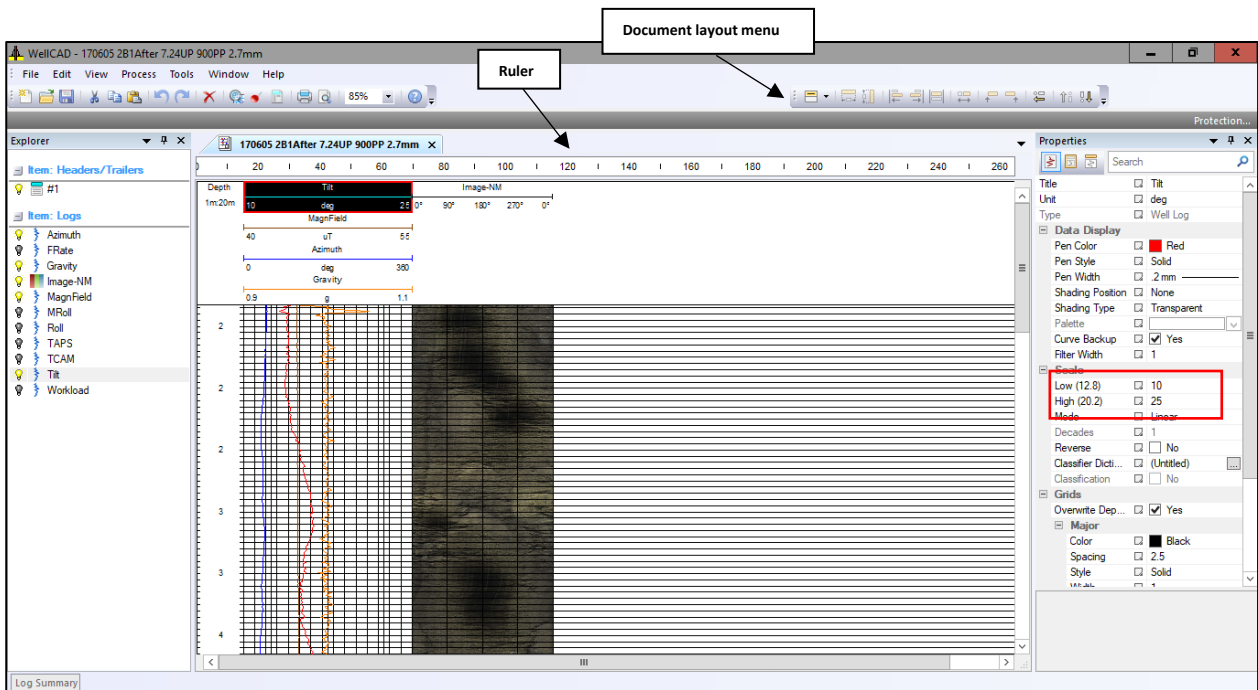


Figure 29: WellCAD image, minimum value of the scale.

Before processing the data, a second corrected image and a Structure log were created:

- To create a second image was used the *copy/paste* function of the right mouse button. Then selecting both images was disabled the Grid Depth option that is situated in the Base Setting of the Properties. The first correction of the second image occurred selecting with the left mouse button the image copied and subsequently using the Menu bar, clicking on *Process, ISI module, RGB logs, Interpolate Bad Traces* (this function is used to remove white lines from the image). The second correction occurred by adjusting the brightness and contrast of the image, using the same process as the previous correction but once inserted in the RGB logs selecting *Adjust Brightness and Contrast* (a window was opened where first was selected Histogram, second Auto and then OK).
- To mark the discontinuities a structure log was created using the commands *Edit menu, Insert New Log, Structure Log* (a window was opened where was selected Create an empty structure log). The structure log was placed under the correct image using the *Align Left and Right button*.

Subsequently some parameters in the Main Settings of the structure log were changed:

- The structure log was renamed
- Projection was chosen as the type of Style
- The value of the caliper was changed with the diameter of the borehole (89 mm). The dip value of a planar feature is directly related to the height (amplitude) of the sinusoid that defines

it in the 360° unwrapped image of the borehole wall. This amplitude is directly related to the caliper value of the borehole and so the image itself.

- The Dictionary_Discontinuities (relative to the type of discontinuities that can be marked Table 2) was inserted in the structure log through the box attribute in the main settings.

Table 2: Structure table.

Continuous closed fracture	Yellow	Fc	Continuous fracture and easily recognizable
Discontinuous fracture	Green	Fd	Discontinuous fracture
Opened fracture	Red	Fo	Continuous fracture with aperture
Filled fracture	Dark blue	Ff	Filled fracture by sediments
Void	Grey	V	natural voids
Weakness area	Orange	W	Low resistant area
Lithology	Brown	L	Change of lithology
Structure	Pink	S	Change of the internal structure like veins, stratification, mineral lineation
Water	Light blue	Wt	Water level
Fill	Dark grey	Fill	Soil or non-compacted materials

Once all the initial procedure is finished, you can begin to trace the discontinuities with the following commands:

- *Select* the Structure log with the left click
- *SHIFT + left click* to a trace of discontinuity
- *CTRL + left click* to cancel a discontinuity
- With the *left click* you can also change the position and the inclination of the discontinuities
- *Right click* on the discontinuities to select the type of discontinuity
- *CTRL + SHIFT + left click* to give thickness to discontinuities

After marking all discontinuities, you have to apply the correction to their orientation. For this operation you have to go to the Process menu, *ISI module, Structure Log and select Apparent to true Dip and Azimuth*. A window will open and then select the data as in Figure 30.

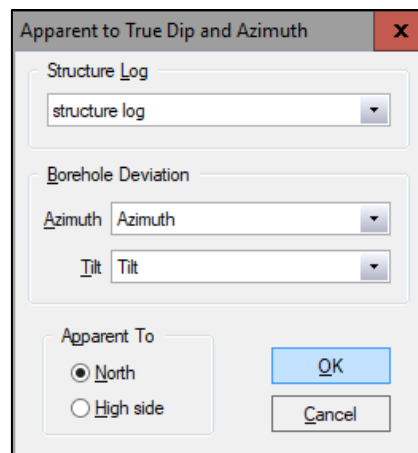


Figure 30: Apparent to true dip and Azimuth.

What the command does is to take the oriented image, so the planar features, to a vertical reference system so that the dip value and dip direction are correct ones. The dip angles derived from the inclined borehole axis are measured from a reference plane which is perpendicular to the borehole axis, and so inclined compared with the horizontal datum. Depending on the borehole path, the traces of the discontinuities can change a lot, because the planar feature is almost vertical while the borehole axis is intersecting it with a certain angle, so the reference plane for the angular measurement in "apparent" will not be the horizontal datum till the "Apparent To True" correction is done (Figure 31).

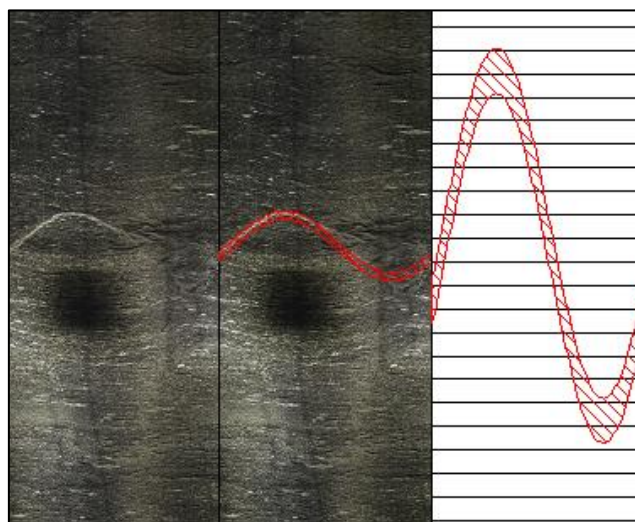


Figure 31: on the left the discontinuity, in the middle the marked trace and on the right the correct trace.

Then with the *copy/paste* function another Corrected structure log was generated, renamed Tadpole log and placed on the right of the first correct projection. The Style was then modified from Projection to Tadpole. The body of the tadpole with respect to the horizontal log scale shows the amount of dip, while the tadpole vector line indicates the azimuth (dip direction).

A 3D Log was created in Edit menu, *Insert New Log* and selecting *3D Log*. It was then renamed, given a thickness of about 20 mm (using the same method as the Depth) and placed to the right of the Tadpole Log. Subsequently in the Main Settings of the 3D Log, on the Amplitude Component was choose the Corrected Image and on the *Structure Component* was choose the Corrected Structure Log. This Log will show the image of the televiewer as a cylinder and the planes containing the discontinuities.

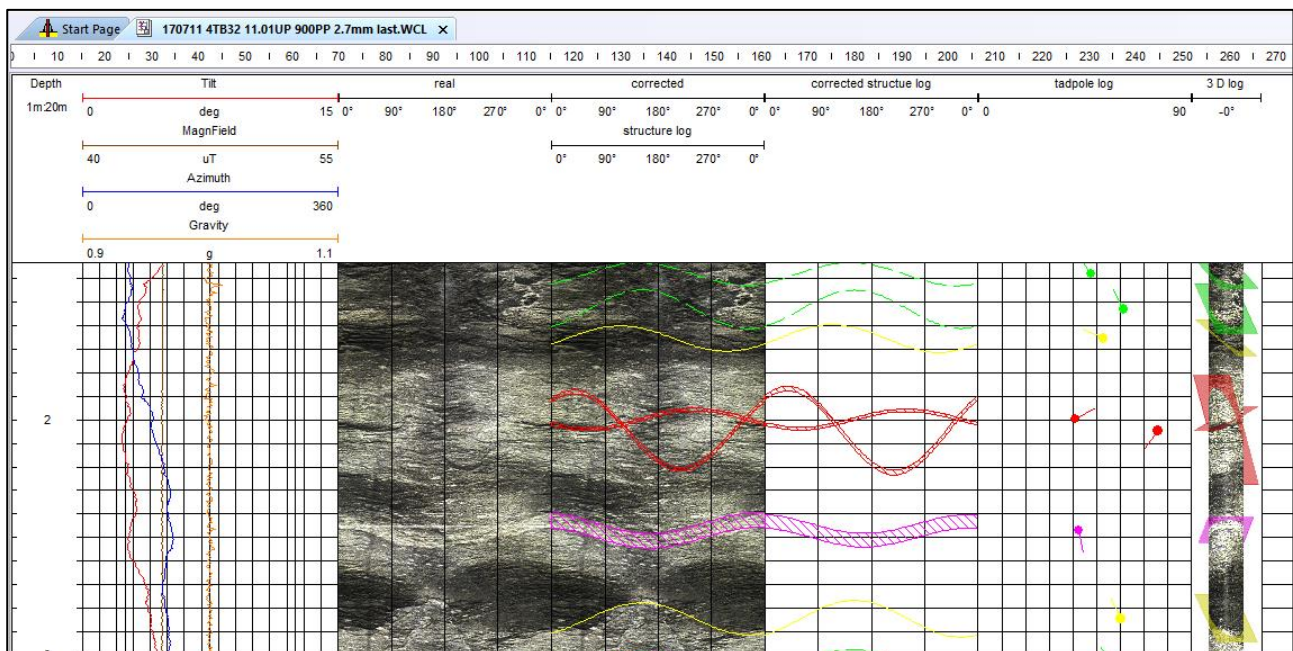


Figure 32: Image of WellCAD at the end of the analysis.

Finally, you have to create a stereographic projection of the traced elements and it can be done with two different methods:

- The first one is done using WellCAD by going to *Tools* and selecting *Chart*. Then two folders are opened consecutively, in the first you have to select *Blank Polar & Rose* and in the second the *Corrected Structure Log*. A new file will be opened in which the stereogram will be shown (Figure 33).

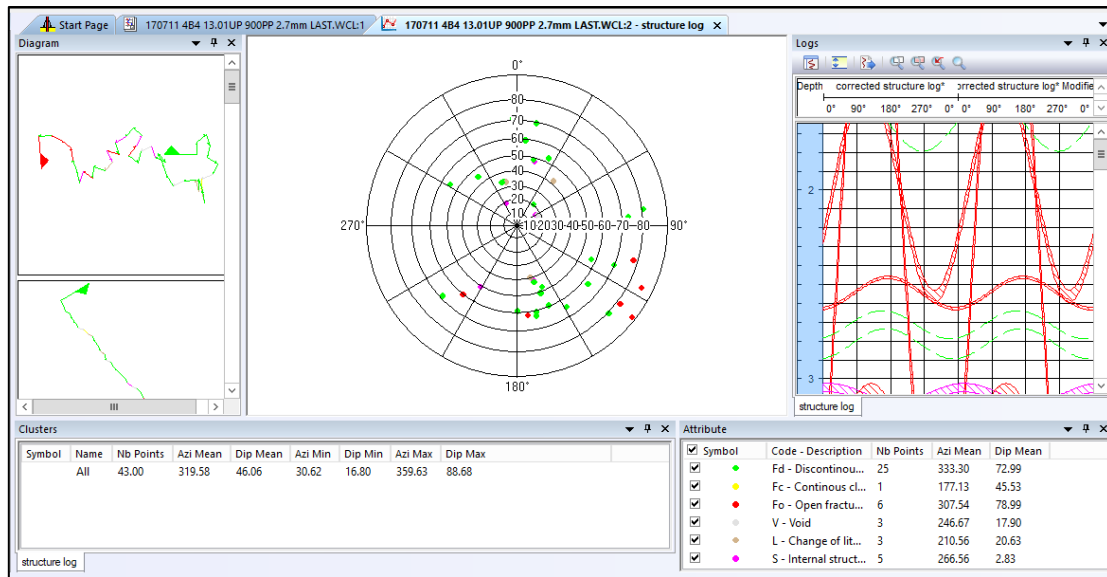


Figure 33: projection of the planes.

Extracted data

Subsequently, data for each hole in each blast were extracted to allow analysis using Dips software [Dips, 2020] (is designed for the interactive analysis of orientation based geological data). The data were extracted as .txt files with the depth designation, dip angle, dip direction, and structure type detected (Table 3).

Table 3: Data extracted from WellCAD analysis (Borehole 1, 6th blast).

Depth	Azimuth	Dip	Aperture	Type
m	deg	deg	mm	
2.01	355.21	44.93	9.66	Fo
2.22	280.03	64.89	0.00	Fd
2.56	191.06	44.62	122.44	S
3.12	274.69	62.60	0.00	Fd
3.38	335.77	42.83	0.00	Fd
3.54	213.15	67.13	0.00	Fd
4.08	356.06	63.97	0.00	Fd
4.61	359.23	48.89	0.00	Fd
4.62	217.30	15.90	46.00	V
5.53	328.13	70.65	11.12	Fo
6.23	221.50	17.20	80.00	V
6.28	165.81	86.78	0.00	Fd

7.08	317.41	65.47	3.17	Fo
7.97	315.68	65.83	0.00	Fc
8.86	335.92	73.39	0.77	Fo
8.87	160.72	53.03	60.60	S
9.32	80.96	89.13	4.32	Fo
10.22	218.17	74.25	0.00	Fd
10.42	215.60	16.30	76.00	V
10.55	17.72	81.45	0.00	Fd
10.73	218.30	16.00	40.00	V
10.76	3.06	85.23	0.00	Fd
11.74	332.04	77.88	3.73	Fo
11.88	328.49	80.50	2.46	Fo
12.76	304.29	69.97	0.00	Fd

The extracted Data were filtered to allow the definition of the discontinuity planes crossing each hole, without counting the voids and the types of structures that do not contribute to the definition of the in-situ block size distribution.

Only 4 types of discontinuities have been used for the following analysis (discontinuous, continuous, open, filled) and are reported in the following table:

Table 4: Total Discontinuities.

	Discontinuous fractures	Continuous fractures	Open fractures	Filled fractures	Total fractures	Total fracture per campaigns
Blast 1	234	105	12	3	354	1012
Blast 2	212	29	20	4	265	
Blast 4	114	21	24	0	159	
Blast 5	91	14	39	3	147	
Blast 6	59	11	14	3	87	

Blast 7	272	52	49	0	373	2238
Blast 8	304	56	45	0	405	
Blast 9	458	22	27	0	507	
Blast 10	176	16	22	0	214	
Blast 11	306	56	65	0	427	
Blast 12	160	53	89	0	302	

3.1.5 Structure features

The fractures are marked according to their continuity, opening and filling:

➤ Discontinuous fracture

Discontinuous fractures are structures in which the sinusoid is not easily visible and traceable. They are traced when the sinusoid covers between 50 % and 75 % of the hole (Figure 34)

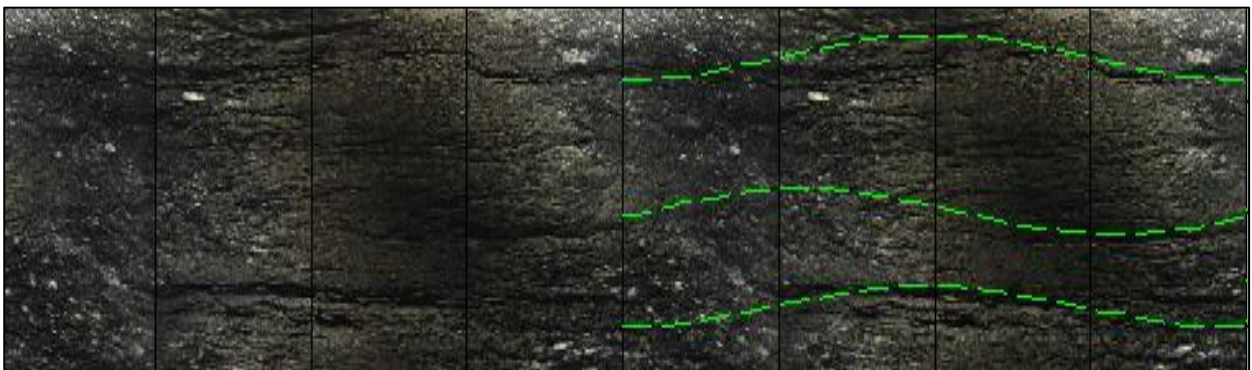


Figure 34: Discontinuous fracture marked.

➤ Continuous closed Fracture

The continuous closed fractures are easily visible, and the sinusoid covers more than 75 % of the hole (Figure 35).

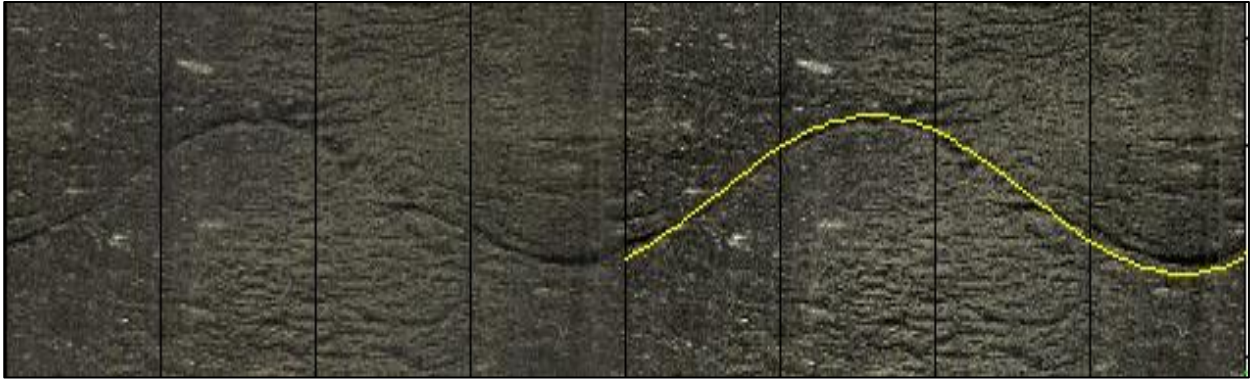


Figure 35: Continuous fracture marked.

➤ Open Fracture

These fractures can be continuous or discontinuous and it is not possible to identify a filler (Figure 36).

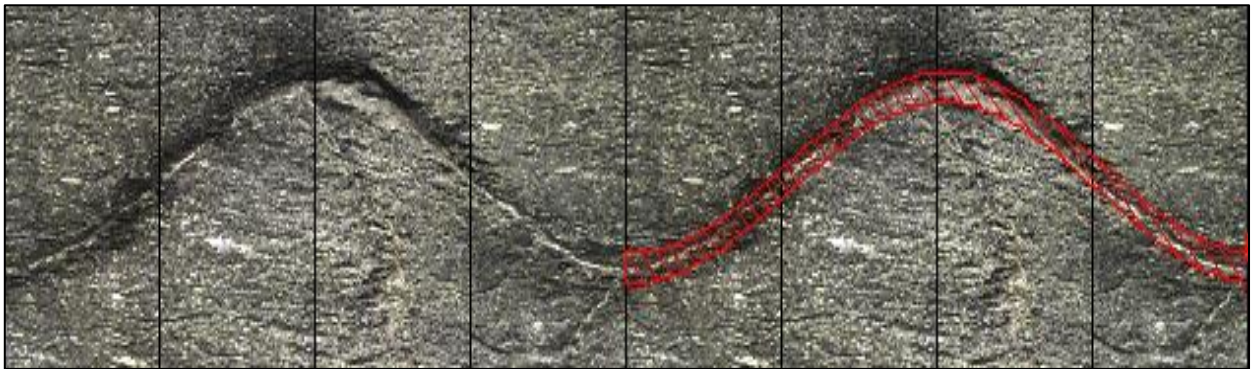


Figure 36: Open fracture marked.

➤ Filled Fracture

These fractures are open and filled with non-consolidating material (Figure 37).

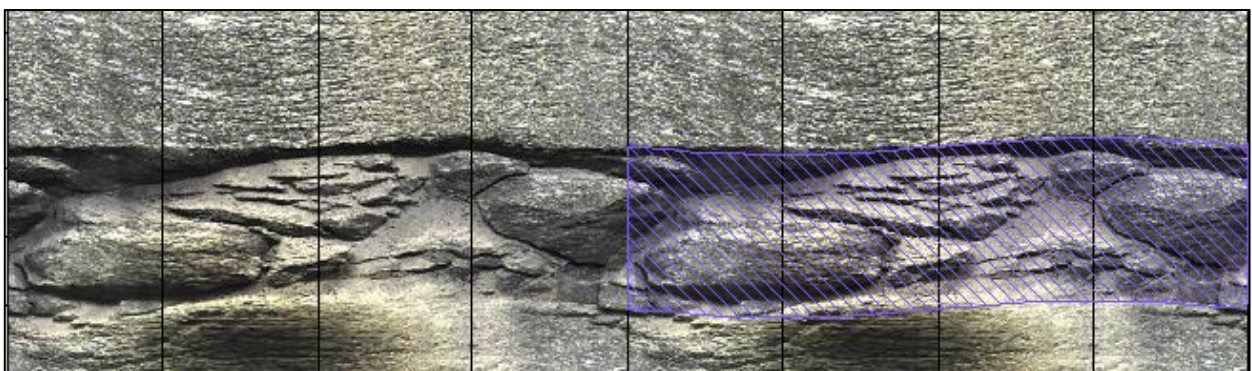


Figure 37: Discontinuous fracture marked.

➤ Internal structure

This structure includes discontinuities due to the internal structure of the rock such as veins, foliation and orientation of minerals (Figure 38).

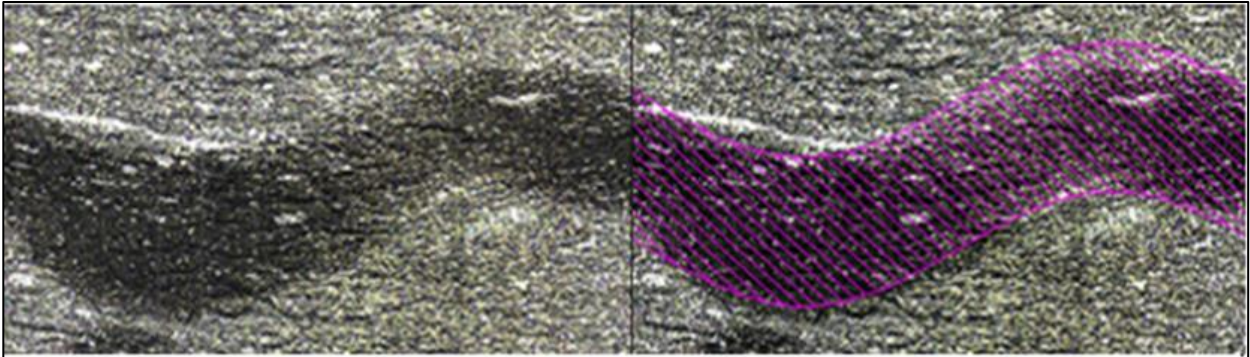


Figure 38: Internal structure marked.

➤ Fill

This feature includes the covering material on the top of the bench. Include soil and filling material and usually is difficult to find it in the televiewer image because have a low thickness and is cutter by the length of the sensor (Figure 39).

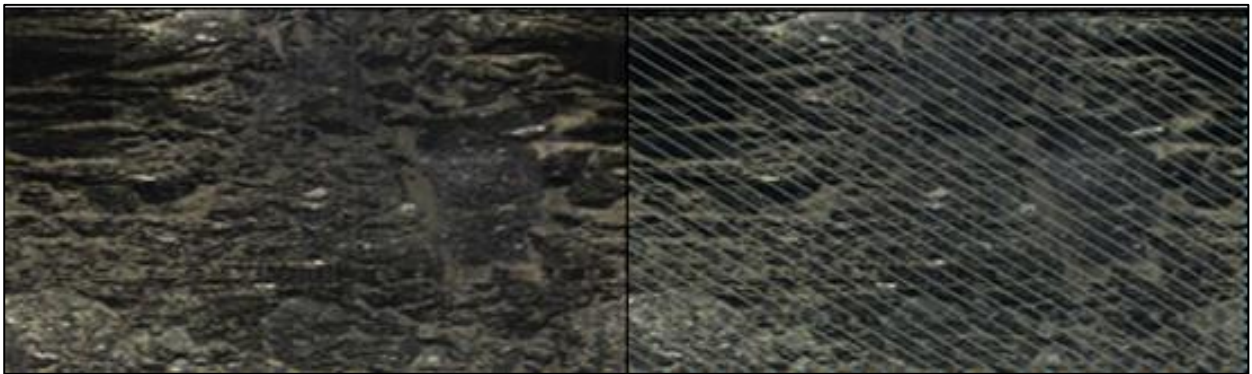


Figure 39: Filing material marked.

➤ Water

This trace indicates the presence of water from that point of the hole onwards, if the water is not turbid and therefore a sedimentation process of the particles inside has occurred, it is possible to trace the discontinuity of the hole (Figure 40).

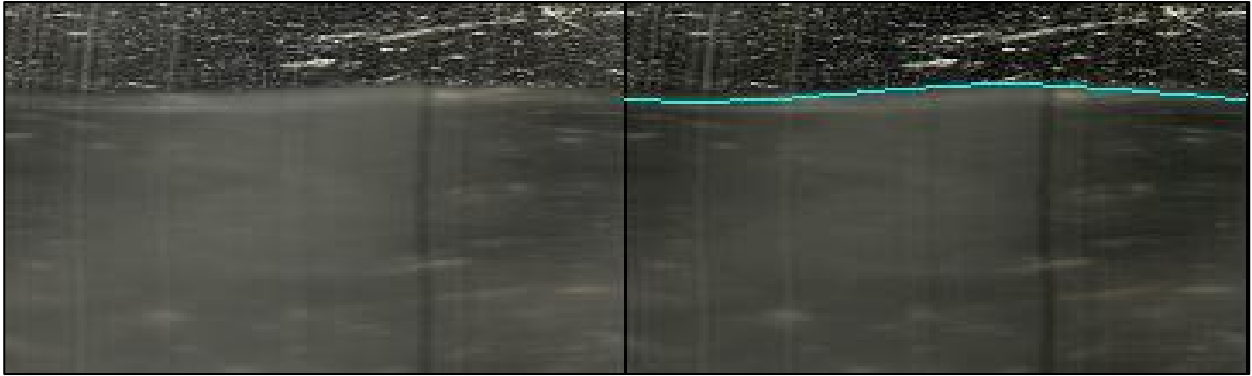


Figure 40: Presence of water in hole.

➤ Void

The voids are very much due to the detachment of material during the drilling phase (Figure 41)

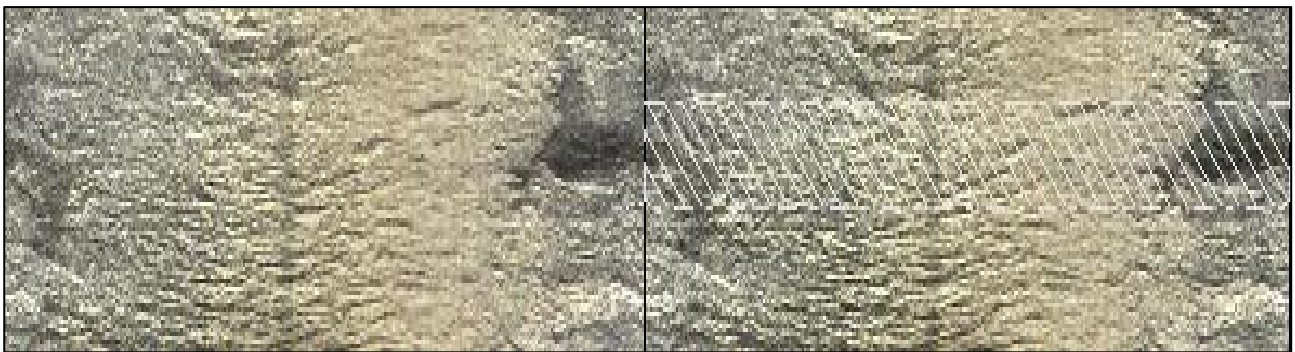


Figure 41: Void.

➤ Weakness area

This area includes internal f rock areas with low strength, highly foliated rock sections or high matrix content (Figure 42).

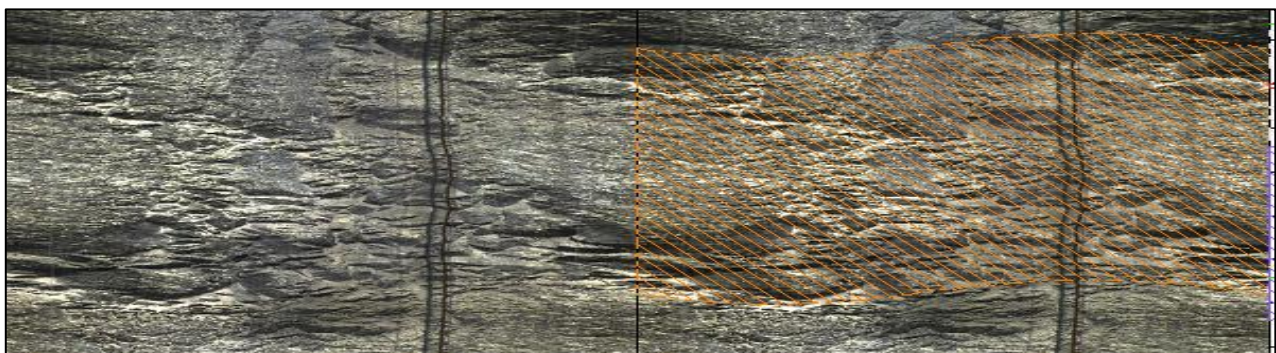


Figure 42: Weakness area marked.

3.1.6 Limitations

The Borehole optical televiewer has some limitations that interfere with image acquisition. The holes must not be obstructed, otherwise they prevent the passage of the instrument, and they must not have water with material in suspension, otherwise the images have too large a distortion and it is impossible to trace the sinusoids during the analysis. In addition, the brightness parameters must be set to the right value, otherwise the acquired images will be too bright, and the correction of the image by the user will not be possible.

Another limitation, which defines a data gap of discontinuities within the rock cluster, is that the discontinuities detected are only those that intersect blast holes. Thus, if a discontinuity is parallel to a blast, or has low persistence, it will not be plotted during the analysis. Furthermore, with this method it is impossible to define the persistence of the fractures, since they are only detected in the hole.

3.1.7 Results

The analysis of the exported discontinuities was carried out using the program Dips, which allows to generate stereo projections with the data of the analysis carried out through the program WellCAD. Dips is program designed for the analysis of orientation based geological data. To represent the density of the poles was used a Schmidt's projection with an equatorial network that gives a representation without areal distortion.

The parameters set in the analysis are shown in the table below.

Table 5: Value inserted during the analysis.

Projection	Equal area
Hemisphere	lower
Distribution	Schmidt
Count circle size	1.9 %
Net	Equatorial

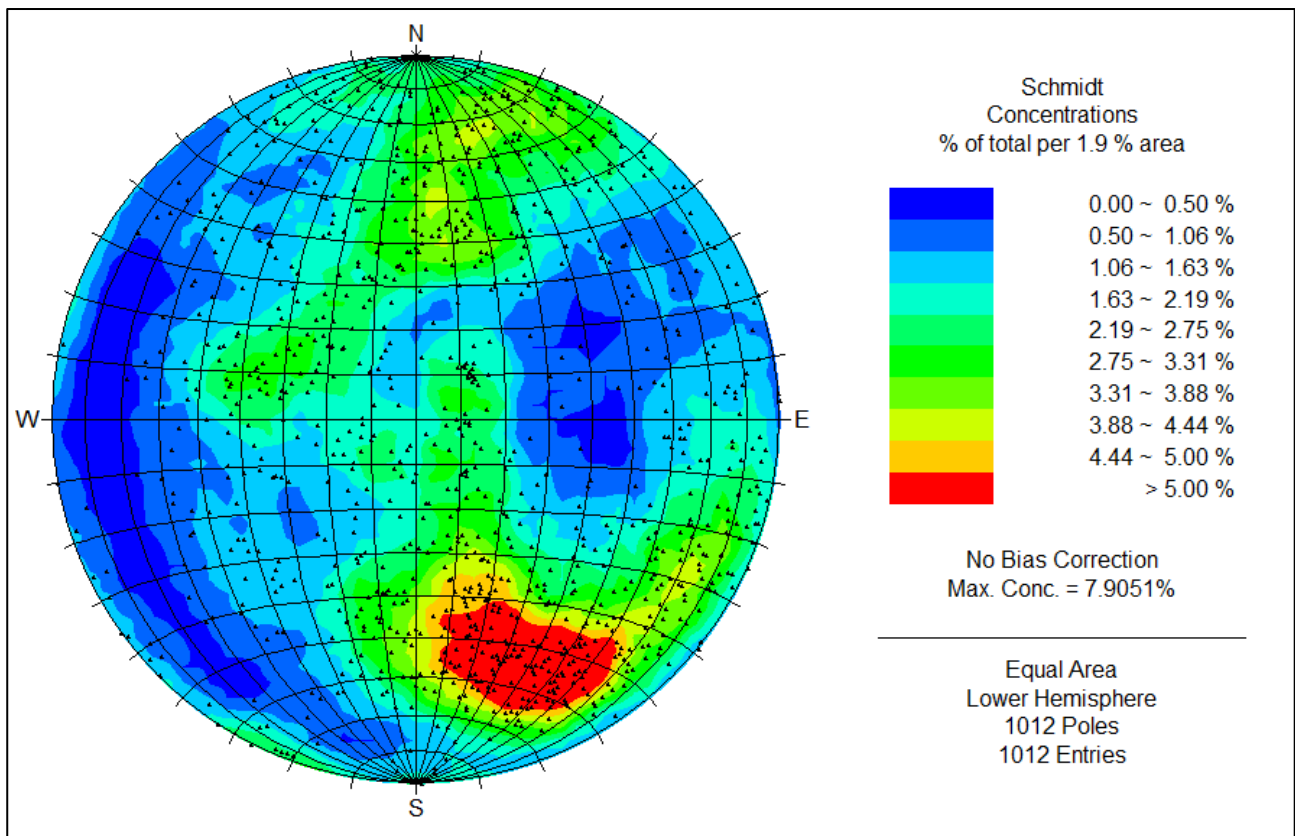


Figure 43: Stereo projection first campaign televiewer.

Stereographic projections were made one for each mining campaign and a significant increase in fractures between the first and second can be seen. This increase in data allows us to visualize the two sets in the NE direction, which are barely visible in the first campaign. Figure 43 shows the stereo projection of the first blast campaign and it is possible to distinguish three main direction of the fracture:

- Sub-vertical South-East that presents the biggest concentration of point
- Sub-vertical North-East
- Sub-horizontal North-East

The last two families begin to stand out slightly in the first campaign while they are clearly visible in the second. This may signify a different application of stress on the rock cluster.

Figure 44 shows the formation of two distinct family sets in the NE direction. The family in the SE direction is persistent in both campaigns. The direction of the three clearly visible sets are:

- Sub-vertical south-east
- Sub-vertical North-East that present the biggest concentration of point
- Sub-horizontal North-East

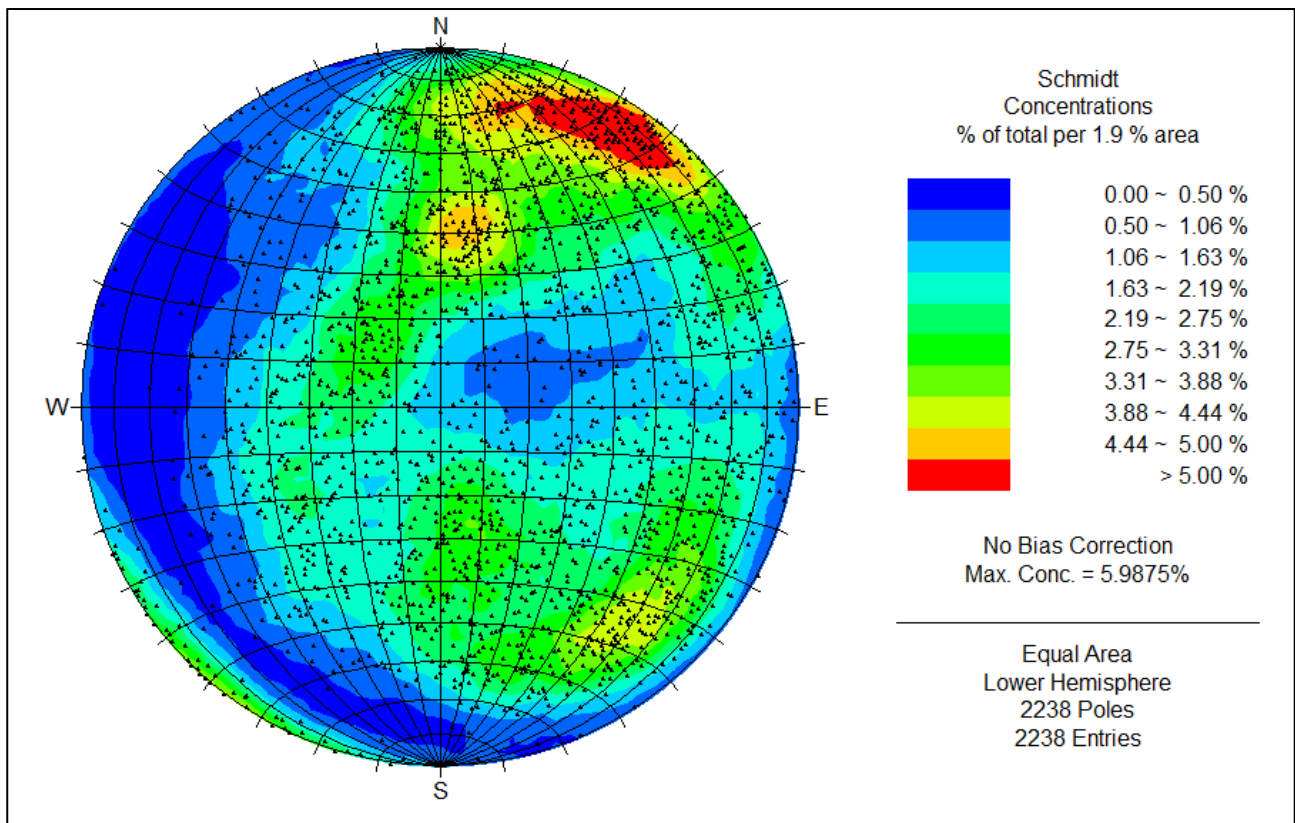


Figure 44: Stereo projection second campaign televiewer.

From the televiewer analysis it is therefore possible to see a continuity of fracture sets in the two campaigns. Since this is an analysis of the interior of the borehole walls, it is not possible to define the persistence, hence the size of the fractures.

3.2 Photogrammetry

Photogrammetry uses a technique based on the calculation of distances using photographs acquired in-situ. The aim is to create a 3D model of the reference surface using 2D images acquired during the excavation campaign. Data acquisition occurred simultaneously with the borehole optical televiewer data acquisition. The images were acquired from different positions to avoid blind spots.

The photogrammetry data used during this analysis came from a previous analysis. The mapping of the rock mass images was done manually, using the software ShapeMetriX 3D [ShapeMetriX 3D].

3.2.1 Equipment

Data acquisition was performed using the following instruments:

- Canon EOS70D digital camera, with two 20 Mp optical lenses (Tamron 17-50 mm and a Sigma 10-20 mm)
- References (calculated thanks to the scan station and targets)
- Tripod

The technique is very simple and fast, so it is easily implemented in different extraction sites. Prior to camera placement, the baseline was measured using a meter. During this study, a distance between the axis of the photos of 4.5 m and a distance from the free face of 35 m was used.



Figure 45: Instruments: Canon EOS70D camera (left) and six targets (right) [Bernardini, 2019].

3.2.2 Procedures for acquisition data

Measurements were taken at 35 m from the free surface and with a distance between them of 4.5 m. Between 4 and 6 photos were acquired in each series to properly capture the free face having a length between 20 and 25 m.

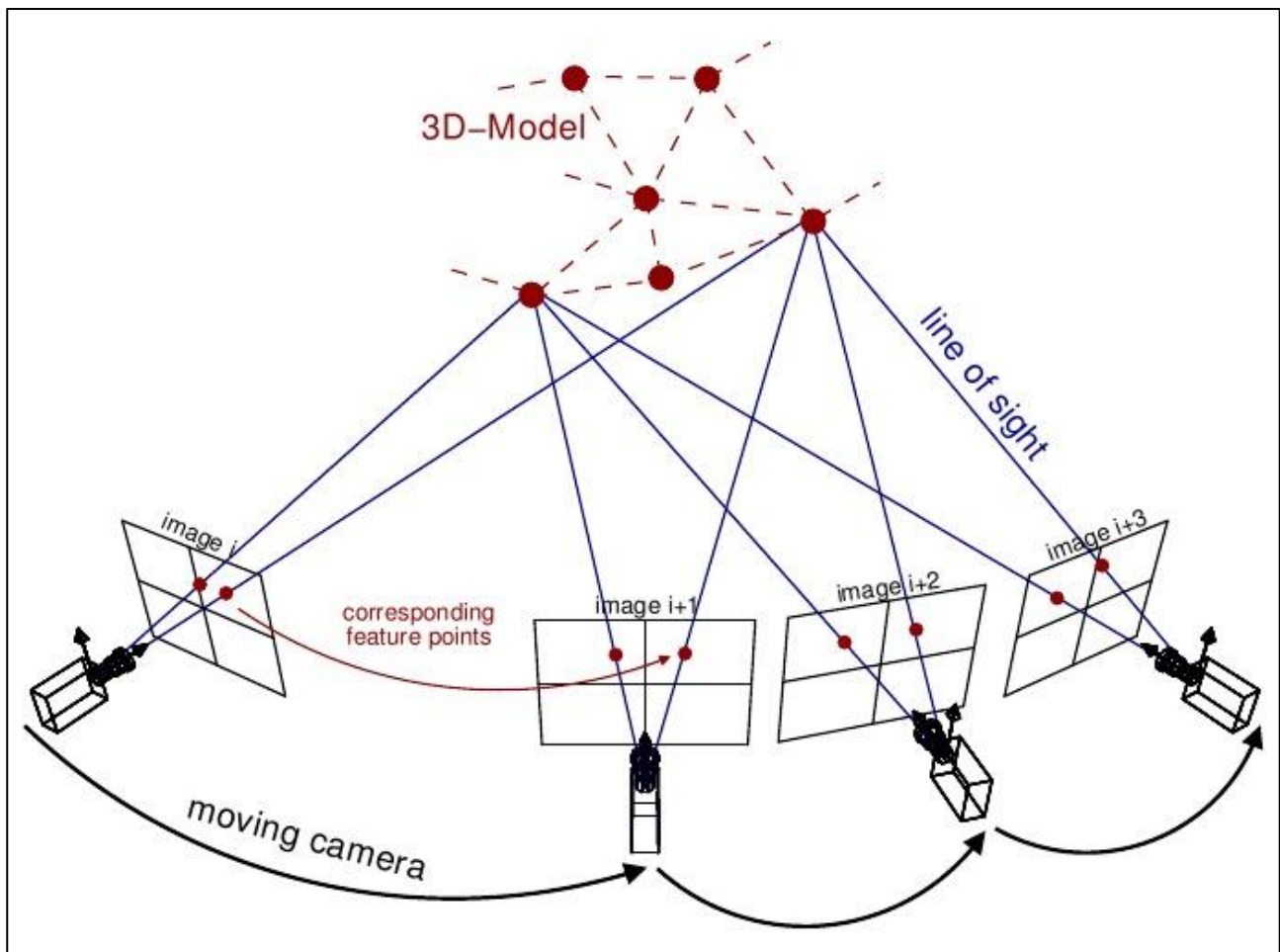


Figure 46: Data acquisition [SfM, 2021].

3.2.3 Principles

Photogrammetry is based on the determination of the position and shape of objects, using the procedure of photometric restitution, starting from photograms acquired either from the ground or from drones.

In order to reconstruct the shape and position of the rock blocks from captured photograms, it is necessary to know the geometric relationships by which the photographs were formed. The photograms can be considered as a central, geometrically rigorous perspective of the photographed object.

Photogrammetry in this study was used to create a 3D model using stereographic image pairs (different positions to acquire photos of the same object). Thus, the generation of the 3D model was performed from a 2D image.

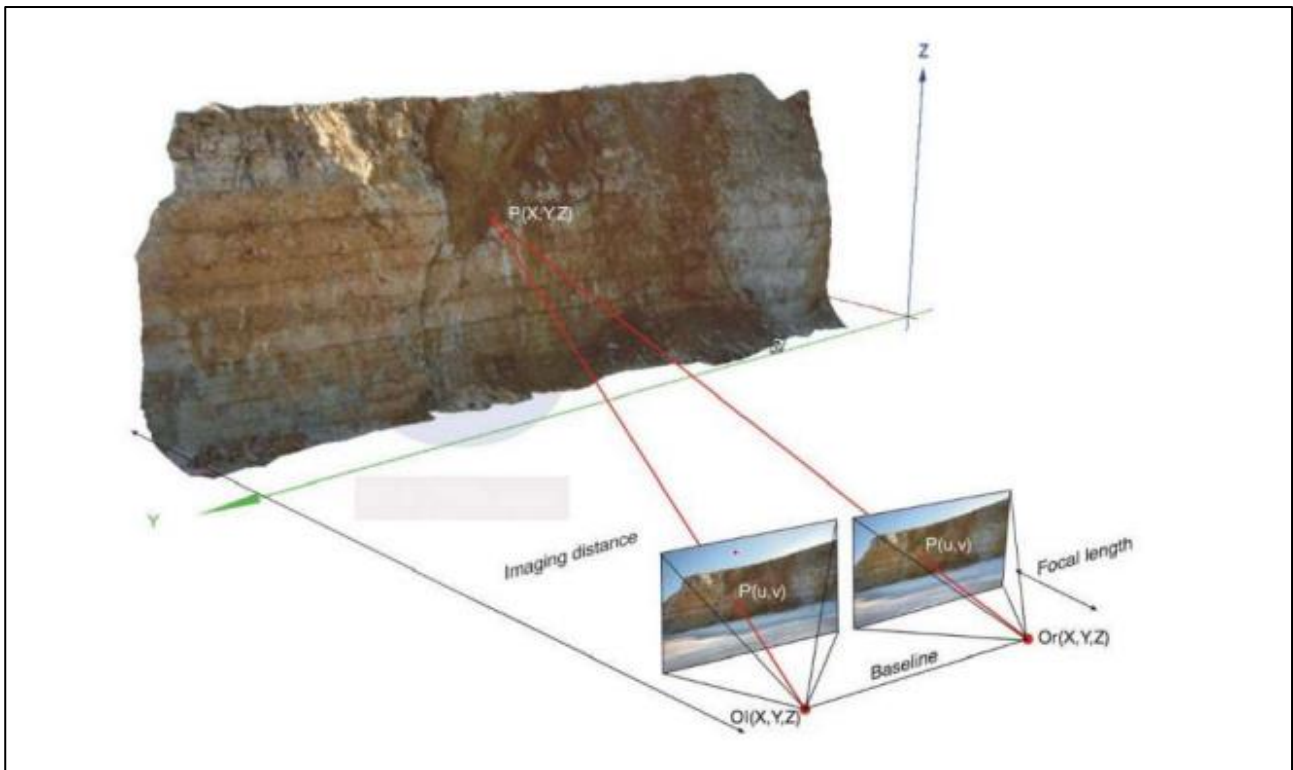


Figure 47: scheme of photogrammetry acquisition [Bernardini, 2019].

To make a three-dimensional image of an object it is necessary that a point is visible from at least two frames, these two points are called homologous points or tie points.

3.2.4 Limitation input data

There are different limitations that affect the results of the photogrammetry and then can divide in on-site and offsite.

It is dangerous position in place targets on the bottom and top of the face because it involves going under the free face, so a collapse would be a problem. The target cannot be placed perfectly parallel to the face and this could cause a distortion in the created 3D model. There are conditions that can affect the result, such as the lighting condition or the presence of shadows or the presence of objects on different planes. Also, if the weather is not favourable is impossible to have picture with a good resolution. Even if the face has significant irregularities, the final model will be distorted or incomplete in those areas that were not visible from the acquisition point. The acquisition of the data takes in place from different position to minimize this problem.

Also, there may be difficulties in positioning the tripod at the precise location identified in the capture pattern, due to the presence of muckpile in front of the face or to the presence of working machine.

3.2.5 Data analysis

Discontinuity marking

The initial analysis of the images from the extraction site were analysed using the program ShapeMetriX 3D, which allows to create a photometric model and then to perform all the analysis at geological and geotechnical level.

The first program module used during the analysis is the *Reconstruction Assistant*. This allows you to load two stereographic photos and create a 3D model. if for each series 6 photos were acquired, 3 different models were created (1-2,3-4,5-6).

The program allows you to manually overlap the images, however there is a residual error, even if you manually try to overlap the lenses as much as possible.

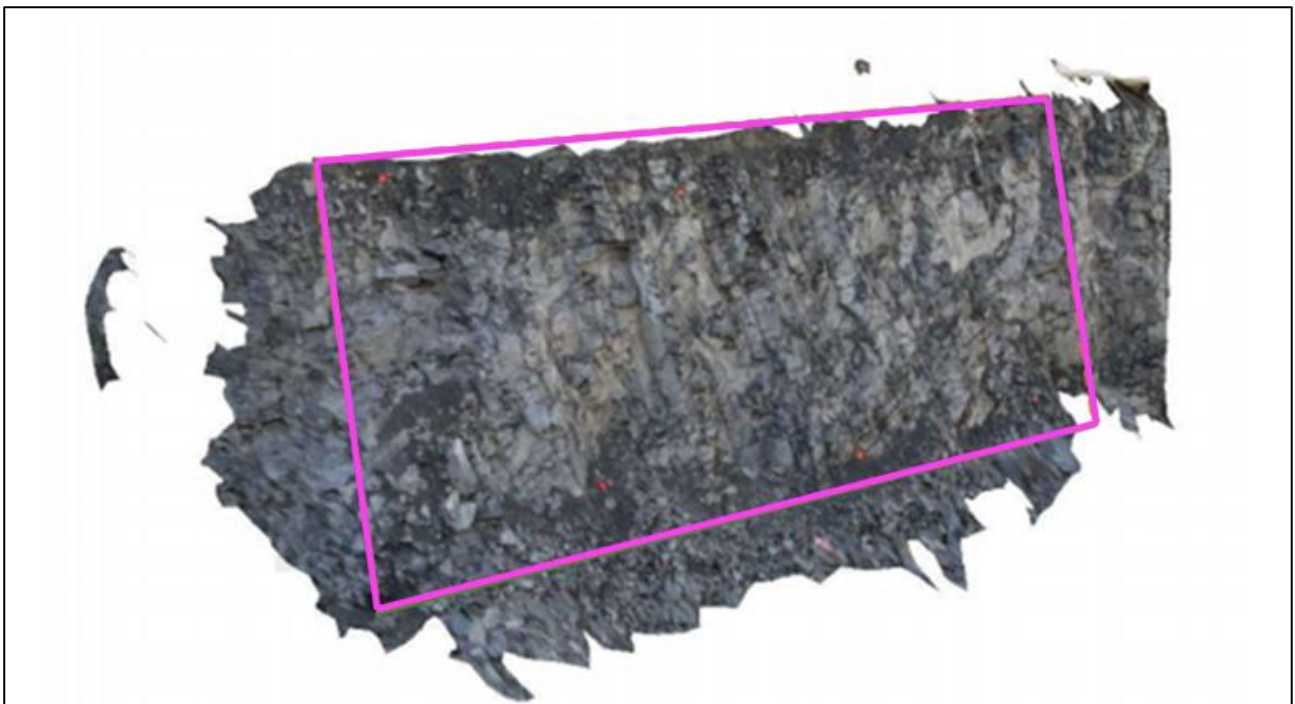


Figure 58: Model of the considered surface [Bernardini, 2019].

In order to better understand the situation of the free face, it is necessary to designate the crest and the toe of it by means of two lines (two ends of the surface). The *Model Merger* module that provides the possibility to join several different models, has not been used, because of a distortion of the results.

Finally, the 3D model of the free surface to be analysed was trimmed using the *Surface Trimmer* module. This command is very useful because it makes it possible to reduce the model points in order to have an archive that collects only the useful zones of the free face (therefore smaller).



Figure 49: Trimmed and referenced 3D model [Bernardini, 2019].

To georeference the model, the *Referencer* command was used, which provides a value of X,Y,Z coordinates to the six control points. Next, after referencing the face, the software allows you to rotate and translate the model. So now it is possible to check the standard deviation between the original and the final coordinates of the targets, and it can be considered acceptable if this value does not exceed 0.01 m.

After completing all these operations, we proceeded with the geological and geotechnical analysis using the *Analyst* module. The procedure was done manually, the operator marked all discontinuities visible in the 3D model using planes or polylines. Each discontinuity was assigned to a family according to its orientation.

The different families were defined using the following colours:

- Subvertical in South-East direction in red (SvSE)
- Subvertical in South-West direction blue (SvSW)
- Subhorizontal in green (Sh)

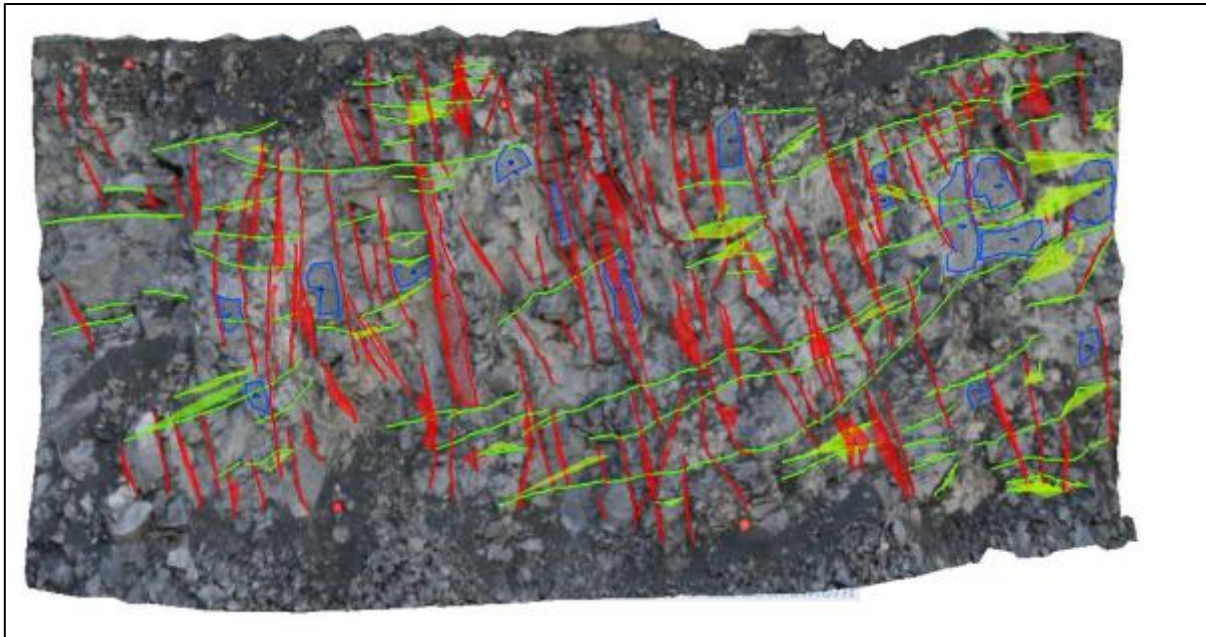


Figure 50: Manual mapping of the joint sets [Bernardini, 2019].

Drawing the marking lines, it is important to pay attention to the curvature you assign, because the software generates a plane that best fits it.

Then an automatic clustering was performed by entering the following parameters:

- minimum number and maximum number of clusters (min 2, max 3)
- Algorithm with 10 iterations
- Maximum membership angle: the maximum angle was set at 35° the lower the value, the more clusters are generated
- Confidence: was assumed a 95 % of confidence

The software algorithm automatically assigns each marked discontinuity to a cluster, not considering the family to which it was manually assigned (different colour in Figure 51 represent different structure sets). Discontinuities that do not belong to any of the assigned families are marked in black.

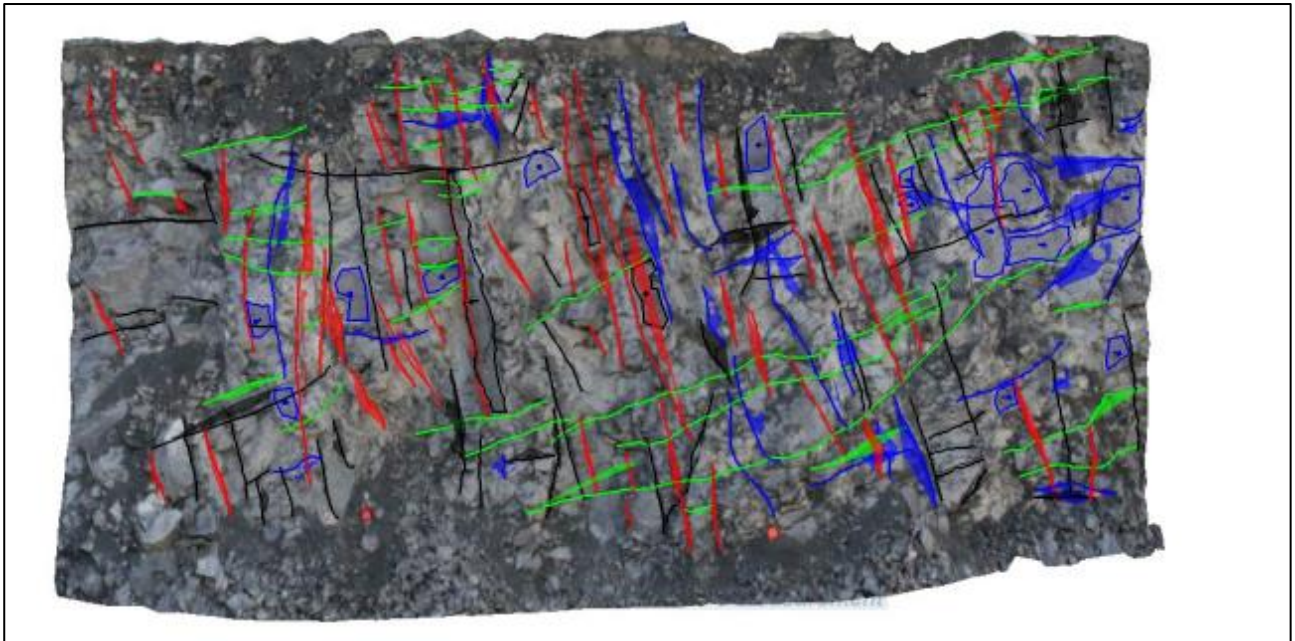


Figure 51: Automatic cluster assignment [Bernardini, 2019].

Subsequently, data of discontinuities present on all generated free surface models were exported. These data were analysed using the Dips [Dips, 2020] program, as in the case of data from the televiewer, and using the same parameters.

3.2.6 Results

The resulting photogrammetry data present in both campaigns 3 different discontinuity sets. The first campaign has a higher number of fractures with prevalent concentration in the set of sub-horizontal and sub-vertical South-East direction.

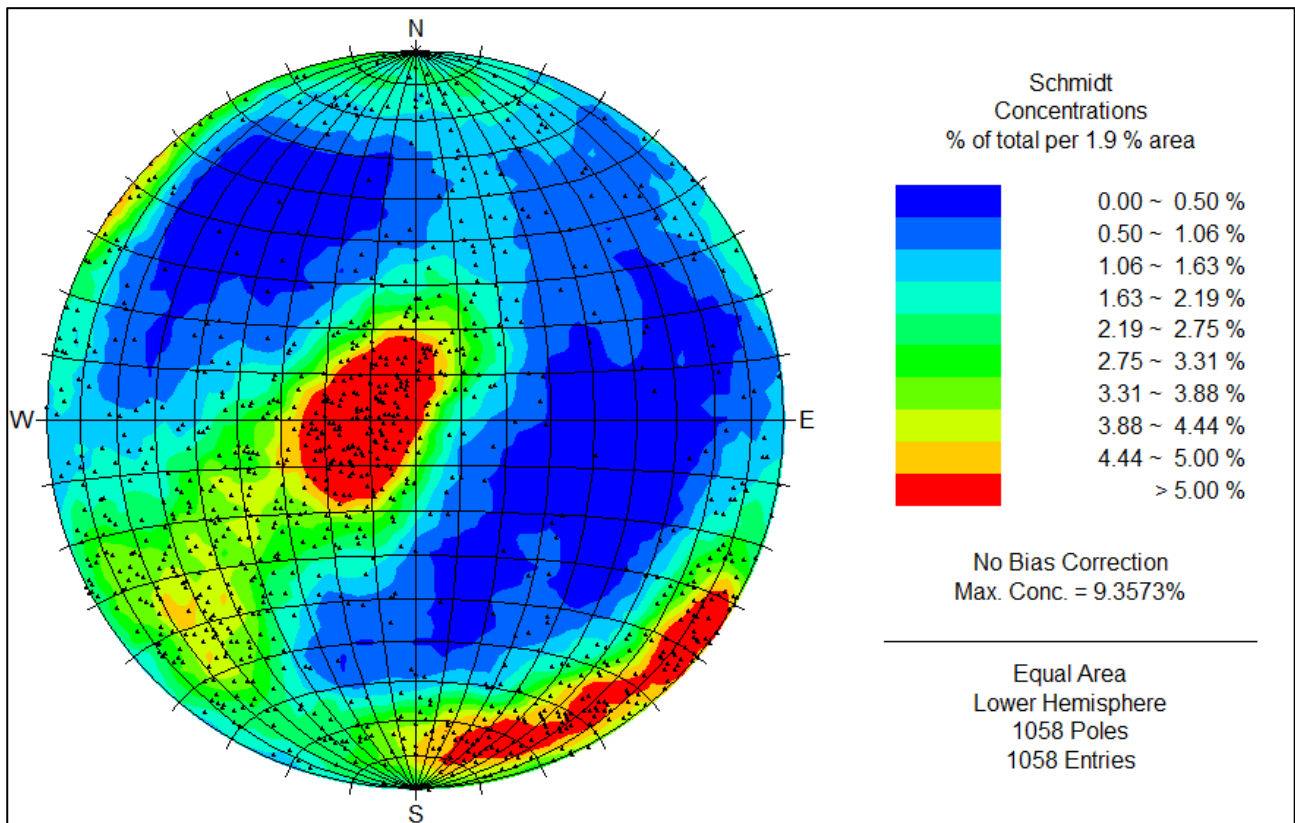


Figure 52: Stereographic projection first campaign (photogrammetry).

In both campaigns, the three sets of discontinuities can be grouped into:

- Sub-horizontal
- Sub-vertical in south east direction
- Sub-vertical south west direction

this last family in the second campaign exceeds the 90° of dip angle and some points are placed in the opposite part of the stereo projection.

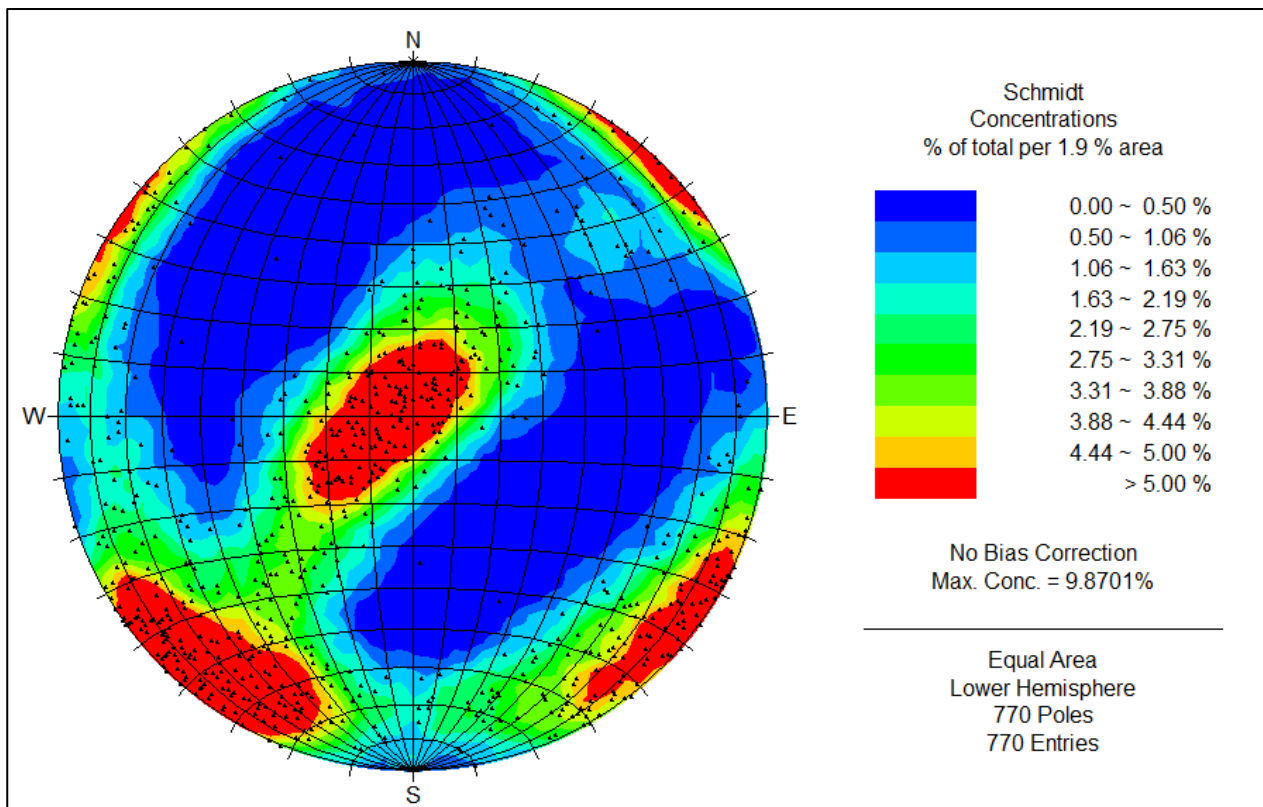


Figure 53: Stereographic projection second campaign (photogrammetry).

3.3 Outcrop measurement

The outcrop measurements were taken outside the quarry using the geological compass. Three natural outcrops were sampled by a geologist and a total of 167 orientation was collected.

The survey points are defined in Section 3.4.2 because they are used to generate holes within the FracMan software. The compass is used to determine the dip and dip direction of surfaces (foliations), and the dip and dip direction of lines (lineations).

To use the geological compass it is necessary side edge of the compass against the wall of the joint, taking care to keep it perfectly horizontal (check the bubble). At this point the angle between the direction parallel to the plane and the needle defines the direction of the plane. The immersion is defined with an angle of 90° to the direction, specifying to which side (it is the direction in which the layer plunges into the ground). Finally, we measure the inclination which the layer dips. The measurement is made at the "maximum slope" using the clinometer.

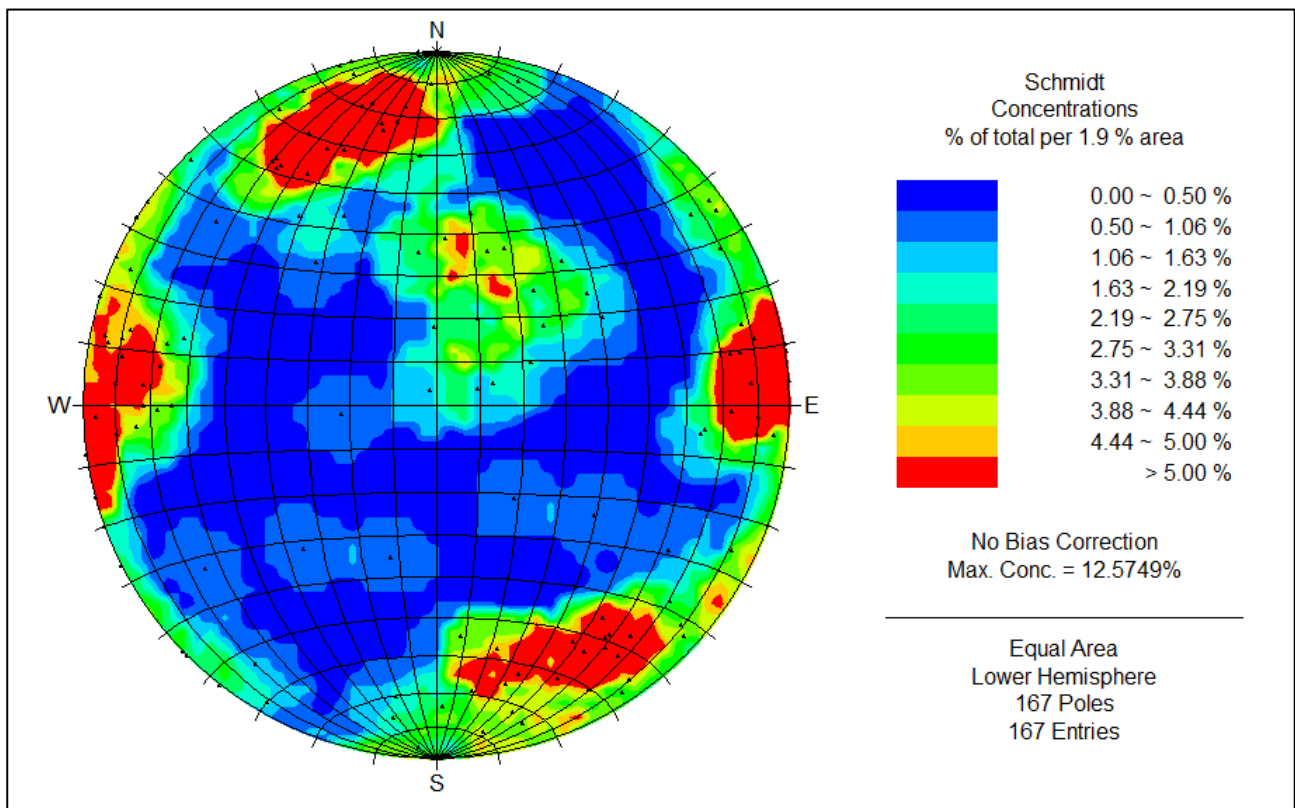


Figure 54: Stereographic projection outcrop.

3.4 FracMan software

A discrete fracture network is a hydrogeological and mechanical system formed by the interaction of a population of individual fractures working as a single system. FracMan was developed by Golder Associates Inc. to model the geometry of discrete features, including faults, fractures, paleochannels, karsts and stratigraphic contacts. The software is designed to provide geologists and engineers with an easy-to-use tool for modelling fractured rock masses, rock mechanics and hydrologic applications in hazardous and nuclear waste management, underground construction, mining and petroleum reservoir engineering. FracMan provides an integrated environment for the entire process of discrete feature data analysis and modelling [FracMan, 2020].

3.4.1 Definitions

- Tracemaps: are a set of line segments in 3-dimensional space and are generally used to represent the intersection between a surface and a fracture.

- Fisher distribution: is the analogue of the Normal (Gaussian) distribution on a sphere, and is theoretically justified when a sum of multiple, uncorrelated variations in rock properties and stress conditions cause the variation in fracture orientation [FracMan, 2020].
- Elliptical fisher distribution: flexible way to analyse and model fracture sets having different amounts of variability in fracture strike and dip that plot as an ellipse on an equal area stereonet [FracMan, 2020]
- Major Axis: direction in which orientation dispersion is greatest
- k1: Geometrical concentration parameter
- k2: ratio of concentration in the directions of greatest to least orientation dispersion
- Spacing: distance between fractures
- P₁₀: linear fracture intensity, is a one-dimensional measurement, measuring the position of fracture-generated intersections along a line through the core axis of the boreholes [FracMan, 2020].
- P₂₁: areal fracture intensity, the length of fractures per unit area [FracMan, 2020].
- P₃₂: Volumetric fracture density, the area of fracture per unit volume [FracMan, 2020].

3.4.2 Input data

Data import from televiewer

The first step was to import the position of the holes analysed during the televiewer analysis. During the measurement of the internal surface of the holes, the televiewer instrumentation acquires the coordinates of the borehole using the starting point of the measurement as the initial point. The measured length will therefore be smaller than the real length, due to the length of the instrument (about 1.45 m long). These data used in combination with data from a probe placed in the holes to obtain the absolute coordinates, have allowed to define the position of the borehole with precision of centimetre.

As is shown in Figure 55 the initial position of the holes the first campaign was effected with 6 parallel blast in one direction (the third is absent due to the breakage of the glass of the instrumentation camera), while in the second campaign, blasts n° 8 and 10 are adjacent and parallel to the others.

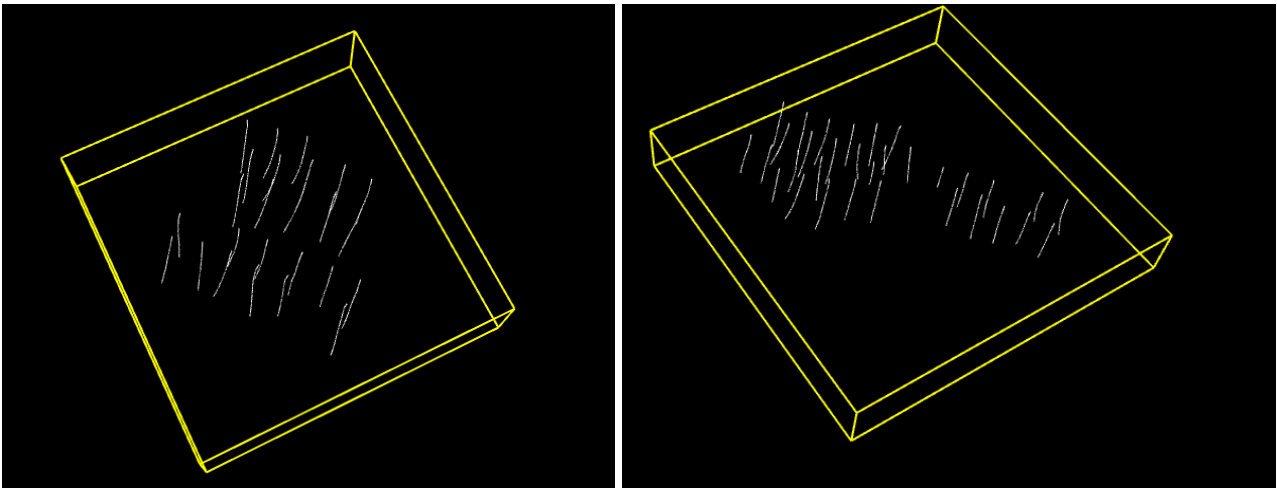


Figure 55: Position and inclination of the borehole (first campaign on the left and second campaign on the right).

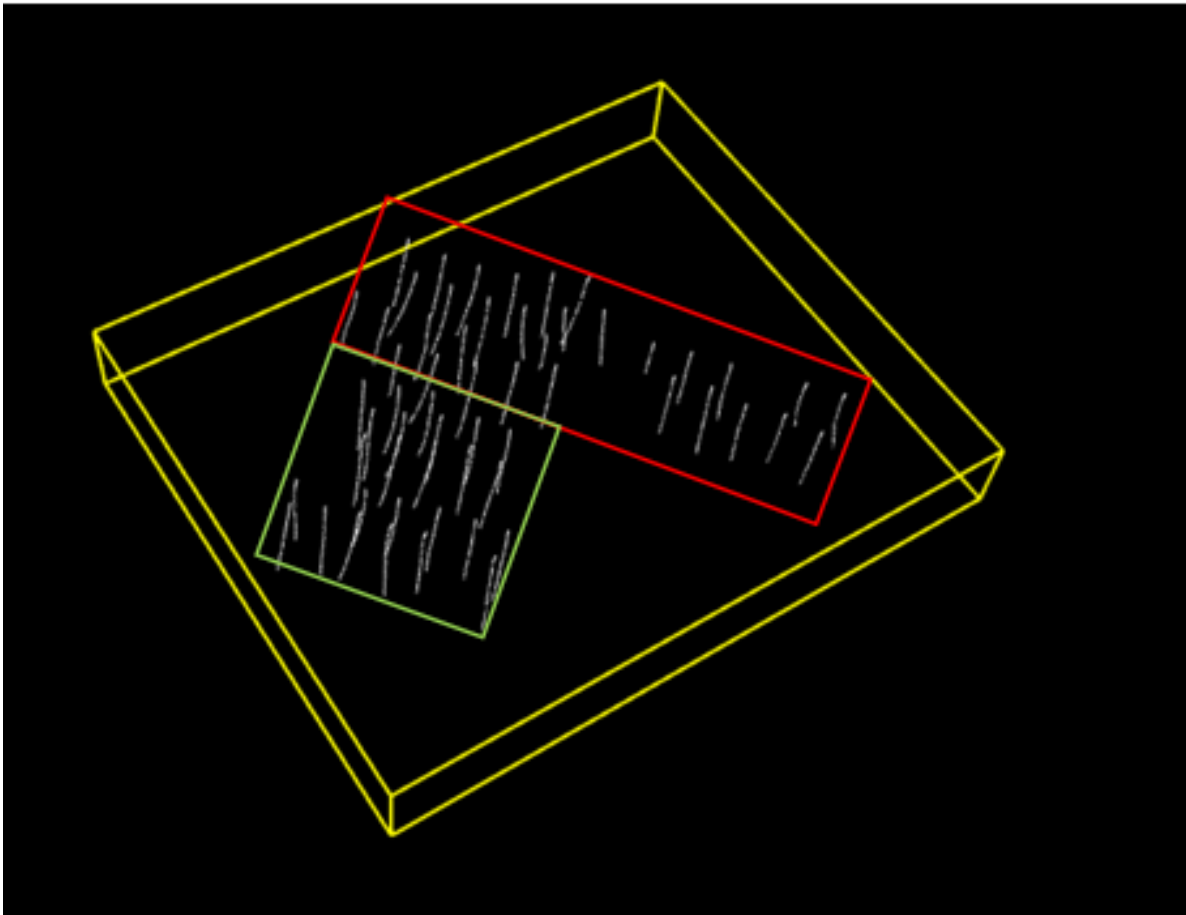


Figure 56: Overall view of the boreholes' location (first campaign in green and second campaign in red).

The position of the holes influences the choice of regions where the fractures are generated.

Subsequently all the discontinuities traced on the in-hole images resulting from the televiewer were imported in FracMan. The imported discontinuities are then manually connected to the well, so the depth, dip direction and dip angle are mapped on the borehole.

As it is possible to see in Figure 57 the upper part of the holes is free from fractures and this is due to the start of the televiewer image acquisition only when the instrument is completely in place, therefore at a depth of about 1.45 m.

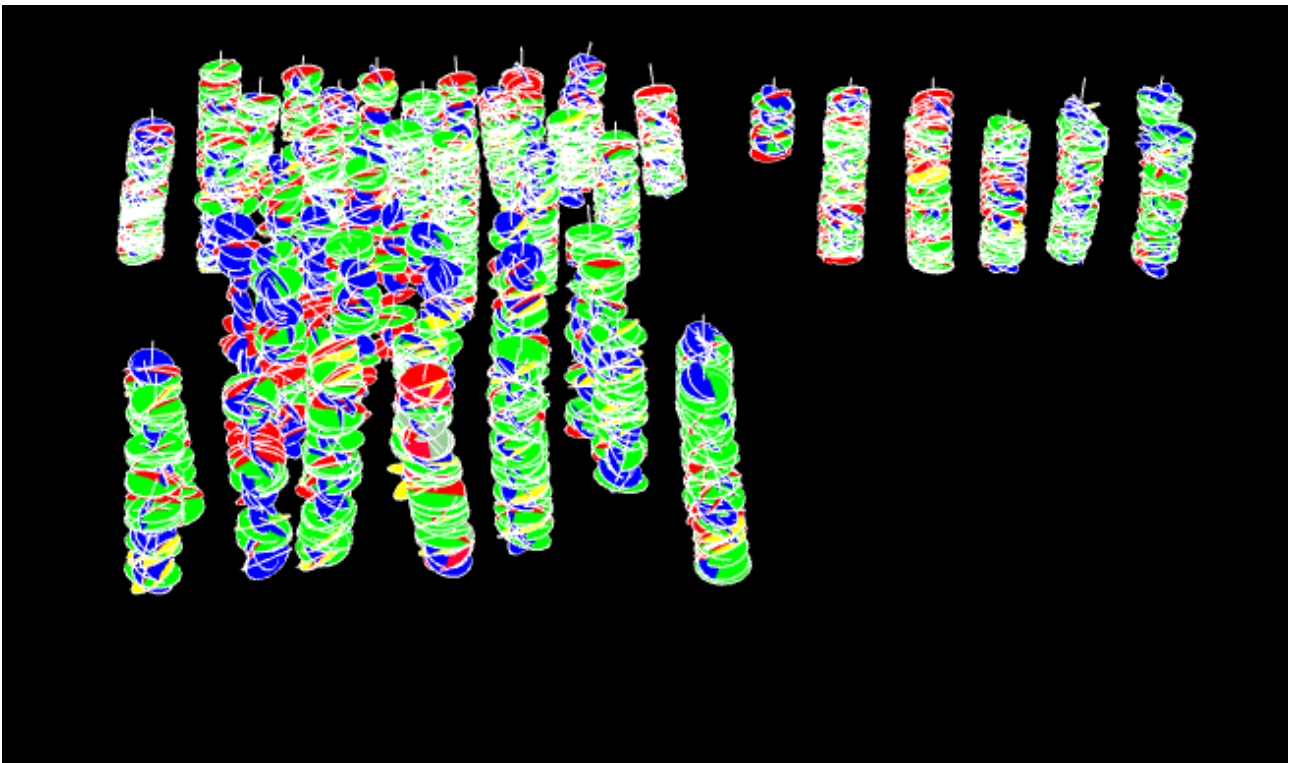


Figure 57: Discontinuities imported in the boreholes.

Data import from outcrops

Data measured by manual acquisition (geological compasses) were used during the analysis to define families, but not used for intersection in the fracture intersection calculation. To fit the data within the program, vertical boreholes were generated at the location where the fractures were detected (Table 6).

Table 6: Position of outcrops measurement (European terrestrial reference system).

Station	X(m)	Y(m)	Z(m)
S1	427085.52	4400486.91	540.63

S2	426775.59	4400374.50	538.84
S3	426803.27	4399806.54	817.03

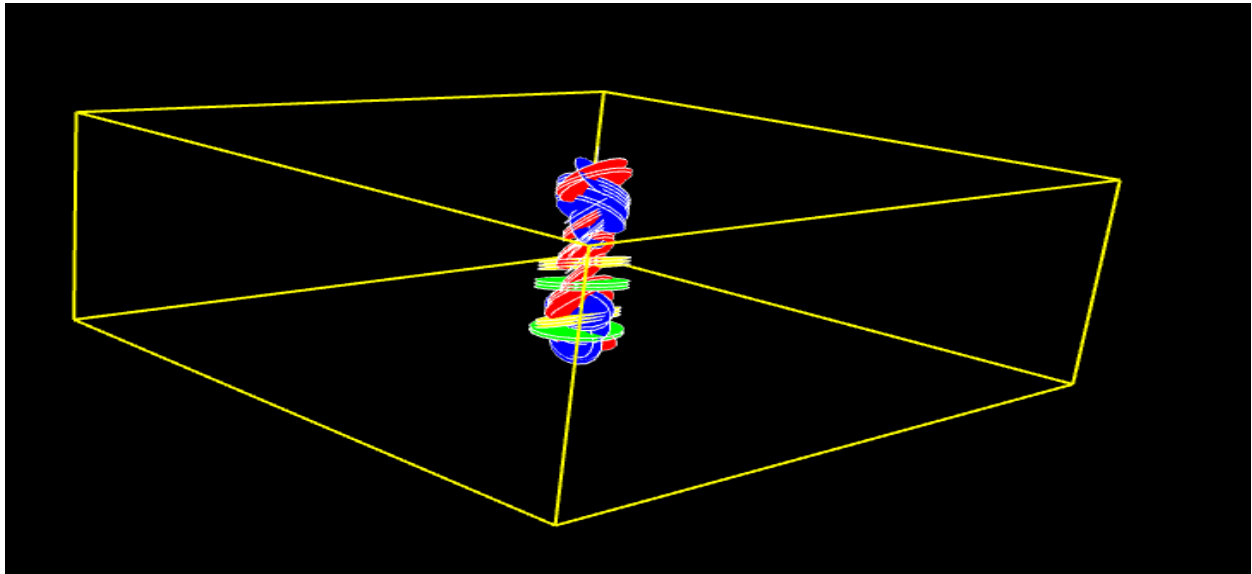


Figure 58: Borehole with outcrop discontinuities (P1).

Data import from photogrammetry

The surfaces were imported into the program as *.obj* files. The width of the surface depends on the analysis performed previously using the ShapeMetriX 3D software. In fact, not the whole free surface was used, but only the surface on which the discontinuities were mapped.

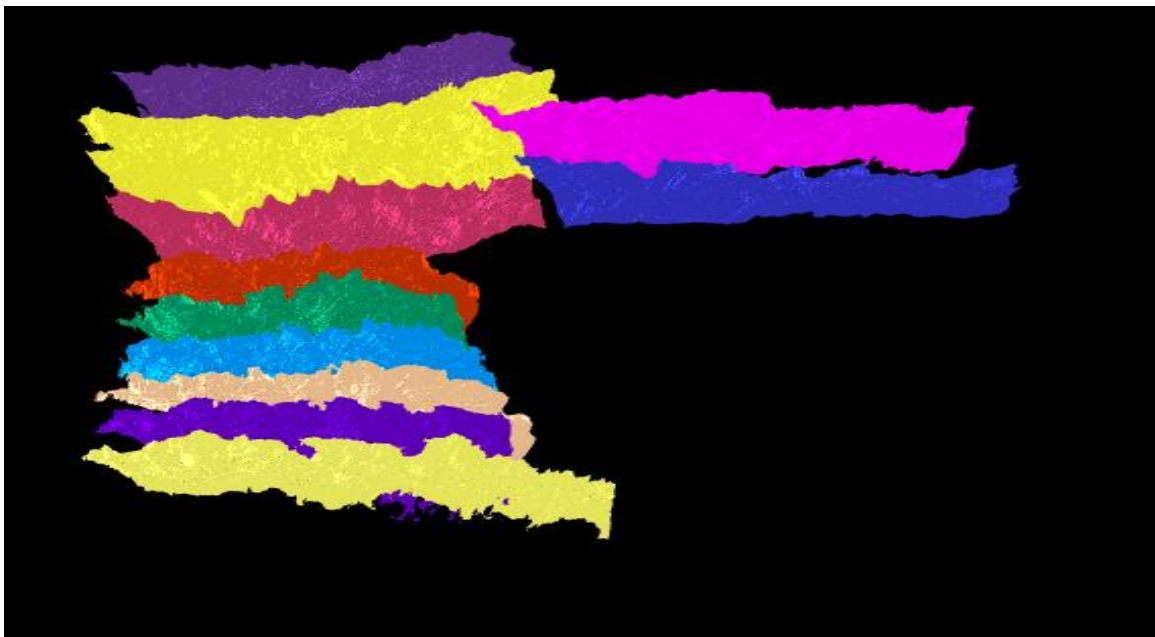


Figure 59: Imported surfaces.

Subsequently, discontinuities mapped onto surfaces were inserted into holes generated to perform the calculation of discontinuity families. For this reason, 12 holes were generated with a fixed distance of 0.1 m between each discontinuity.



Figure 60: Borehole generated with the discontinuity's surfaces.

Finally, joint traces were imported onto the surfaces. The data was extracted from the ShapeMetriX *Analyst* module and processed through a MATLAB filter to be assigned to each set. This was done prior to importing the data into the software due to the inability of the program to filter the traces. Using AutoCad Map3D [AutoCAD, 2021] the files were converted to *.shp* and finally imported into the appropriate format.

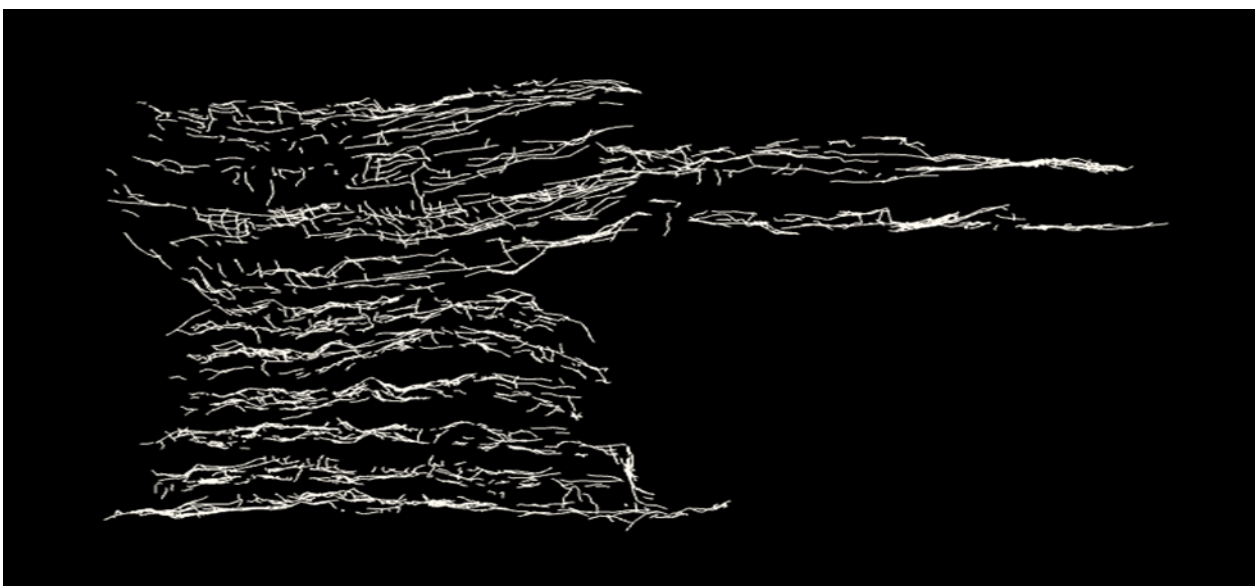


Figure 61: Imported tracemaps.

3.4.3 Data analysis

3.4.3.1 ISIS analysis

The interactive set identification system (ISIS) was used to find the fracture sets from the fracture data. Set Identification defines fracture sets from field data using an adaptive probabilistic pattern recognition algorithm. It calculates the distribution of orientations for the fractures assigned to each set, and then reassigns fractures to sets according to probabilistic weights proportional to their similarity to other fractures in the set. The orientations of the sets are then recalculated, and the process is repeated until the set assignment is optimized [FracMan, 2020].

The method used in this analysis followed several steps:

1) definition of the limits of the sets of discontinuity families

Initially, a stereographic projection of the discontinuity data relative to each campaign was performed. Subsequently, through a visual analysis, sectors were created to contain the family sets, the same for each campaign.

Table 7: Limit of each family defined by the user.

	Dip direction (°)		Dip angle(°)	
	Start	End	Start	End
SH	0	359.9	65.01	90
	75.01	324.99	50.01	65
	195	324.99	35.01	50
	195	265	15.01	35
SHNE	325	75	35.01	65
SVSE	75.01	194.99	0	50
	265.01	334.99	0	35
SVNE	335	75	0	35
	195	265	0	15

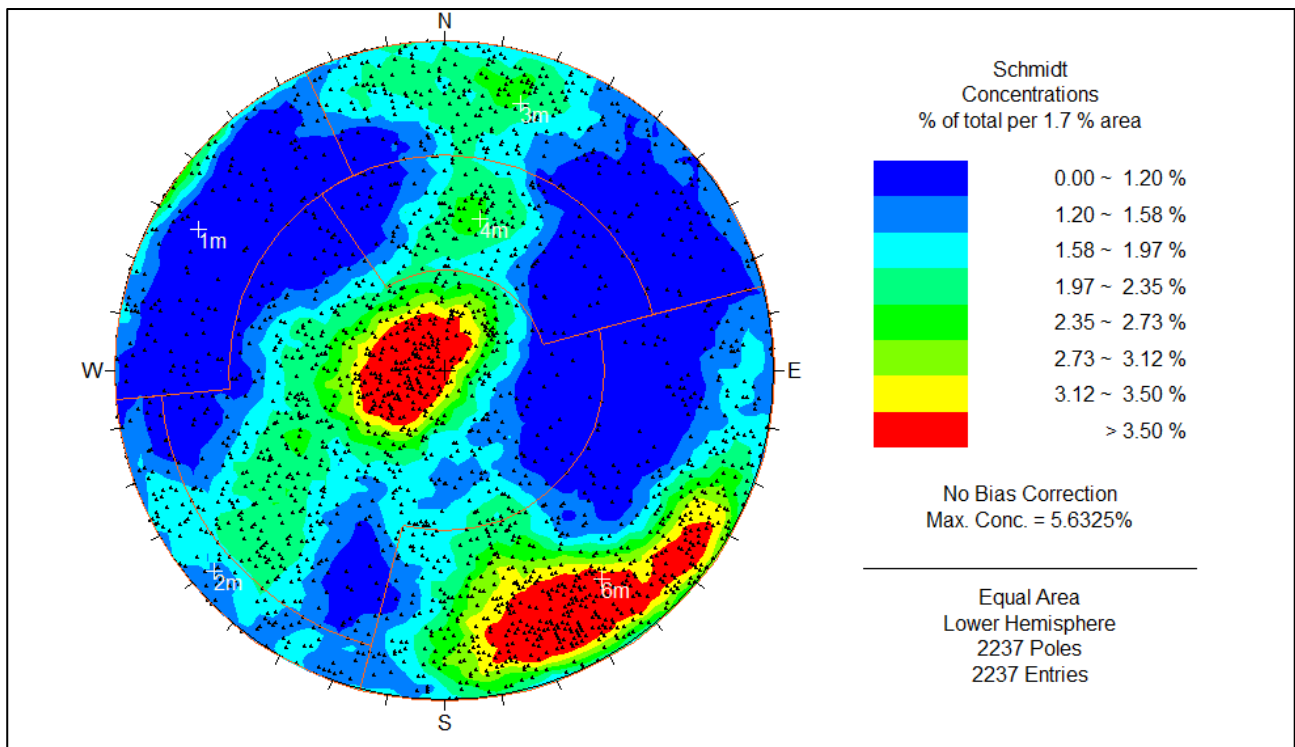


Figure 62: Stereographic projection first campaign with boundaries defined by the user.

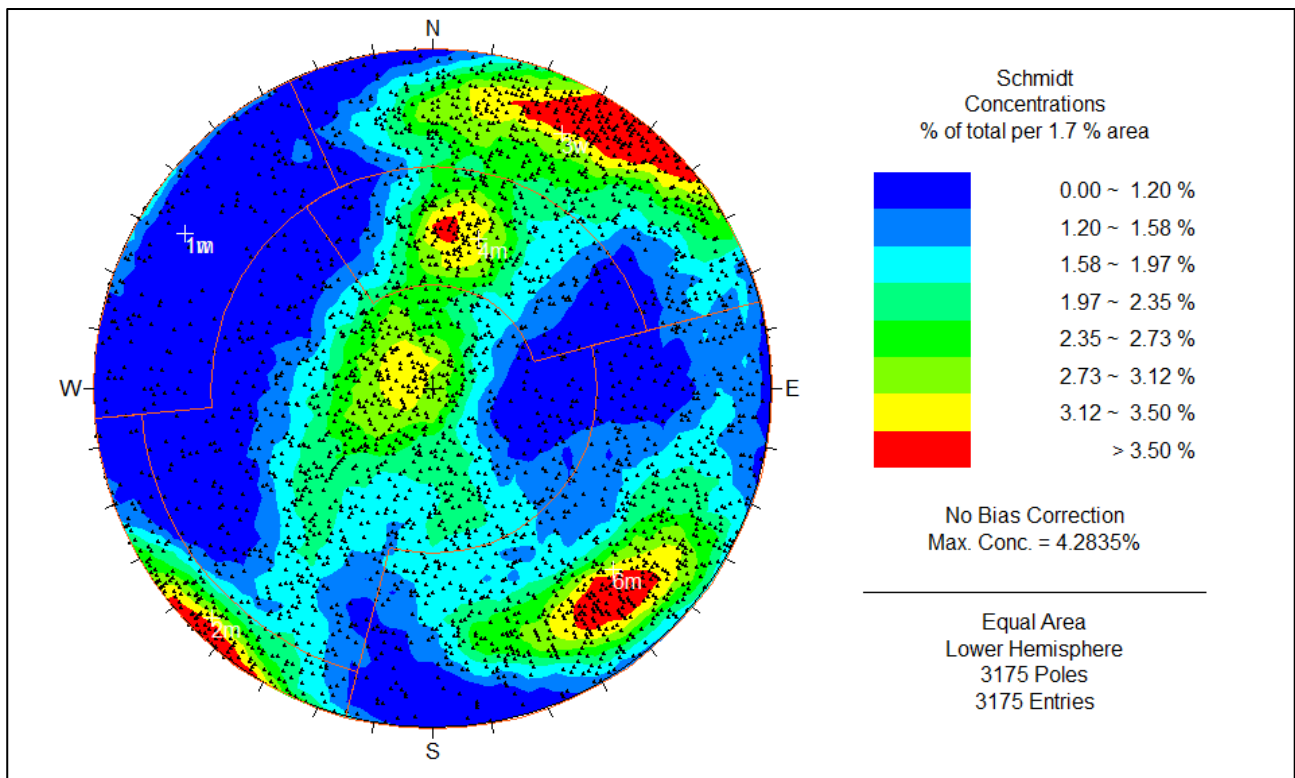


Figure 63: Stereographic projection second campaign with boundaries defined by the user.

Then, after having defined the boundaries through the command "*add set window*" of Dips and having exported the data on excel, through a filter has been calculated the number of fractures of each set and have been assigned to each family. Subsequently the fractures have been imported again on Dips, to obtain in mean pole of each set. The operation was repeated separately for each campaign. The mean poles of each family were subsequently used as seeds the distribution algorithm used by the software.

Then the limits defined through the visual inspection of the stereographic projection were applied directly in FracMan, to perform the distribution simulation and find the most suitable to describe the sets found previously. Table 8 and 9 show the data relative to the analysis carried out for the two campaign.

Table 8: Data relative to the ISIS analysis (first campaign).

Set	Sh		ShNE		SvSE		SvNE	
	Fisher	elliptical Fisher	Fisher	elliptical Fisher	Fisher	elliptical Fisher	Fisher	elliptical Fisher
Fracture counted	792	792	168	168	846	846	431	431
Kolmogorov Smirnov	0.07	0.06	0.06	0.05	0.06	0.03	0.09	0.08
k-s probability	0.41	0.74	0.92	0.97	0.65	1.00	0.31	0.44
Mean pole (tr/pl)	242.31, , 68.03	243.87, , 68.93	12.95, 51.75	12.73, 51.68	139.58, 16.75	141.30, 17.14	25.74, 10.56	24.63, 10.78
Major axis(tr/pl)	62.31, 21.97	49.29, 20.44	192.95, 38.24	105.38, 2.09	319.58, 73.25	236.55, 16.50	205.74, 79.44	291.99, , 13.78
Minor axis(tr/pl)	332.31, , 0.00	141.11, , 4.86	282.95, 0.00	197.02, 38.24	229.58, 0.00	7.86, 65.83	115.74, 0.00	151.47, , 72.37
k1	7.29	7.54	22.28	25.95	6.59	7.26	7.23	8.92
k2		1.33		1.82		1.69		2.17

Table 9: Data relative to the ISIS analysis (second campaign).

Set	Sh		ShNE		SvSE		SvNE	
	Fisher	elliptical Fisher	Fisher	elliptical Fisher	Fisher	elliptical Fisher	Fisher	elliptical Fisher
Fracture counted	956	956	360	360	980	980	879	879
Kolmogorv smirnov	0.06	0.06	0.07	0.06	0.06	0.03	0.06	0.05
k-s probability	0.59	0.66	0.62	0.84	0.72	0.99	0.57	0.78
Mean pole (tr/pl)	229.63, 70.32	230.54, 71.23	16.38, 51.81	16.10, 51.75	132.96, 20.00	133.41, 20.27	31.31, 11.59	31.77, 11.33
Major axis	49.63, 19.68	46.64, 18.73	196.38, 38.19	286.10, 0.00	312.96, 70.00	229.35, 15.65	211.31, 78.41	298.94, 13.83
Minor axis	319.63, 0.00	137.05, 1.19	286.38, 0.00	196.10, 38.25	222.96, 0.00	354.32, 63.95	121.31, 0.00	159.78, 71.97
k1	7.01	7.14	20.53	23.61	6.59	6.98	9.68	11.38
k2		1.26		1.77		1.48		1.93

In all sets the most suitable distribution to represent them is the elliptical Fisher.

3.4.3.2 Spacing

The first index analysed with data derived from the televiewer was the spacing between fractures. This data was calculated solely to define how the discontinuities are distributed within the borehole, so to understand the mean spacing between fractures. The calculation can be done with the following formulae:

$$Spacing = \frac{\text{distance between first and last joint marked}}{N - 1}$$

The N value defines the number of fractures marked during the analysis. The value at the numerator is the distance between the first joint marked and the last one (Figure 64).

The following tables show the value of spacing calculated during the analysis:

Table 10: Spacing result first campaign.

FIRST CAMPAIGN					
	Mean	Standard Dev.	CV	CLUSTERING	
Sh	2.10	2.38	1.13	HIGH DEGREE OF CLUSTERING	>1
ShNE	3.76	3.12	0.83	ANTI CLUSTERING	<1
SvSE	0.79	0.40	0.51	ANTI CLUSTERING	<1
SvNE	2.10	1.76	0.84	ANTI CLUSTERING	<1

Table 11: Spacing results second campaign.

SECOND CAMPAIGN					
	Mean	Standard Dev.	CV	CLUSTERING	
Sh	0.98	1.08	1.10	HIGH DEGREE OF CLUSTERING	>1
ShNE	2.92	3.72	1.28	HIGH DEGREE OF CLUSTERING	>1
SvSE	0.60	0.26	0.43	ANTI CLUSTERIN	<1
SvNE	0.65	0.33	0.51	ANTI CLUSTERING	<1

In Table 29 of Appendix A it is possible to see all spacing values calculated for each hole.

3.4.3.3 Linear fracture intensity

The second index that must be calculated using data from the televiewer is the fracture index per unit length. The index P_{10} is given by the ratio of the number of fractures observed in each hole for each discontinuity set and the length of the measurement. As mentioned in the section on data import from televiewer the measurement length is equal to the actual length minus the length of the instrument (Figure 64)

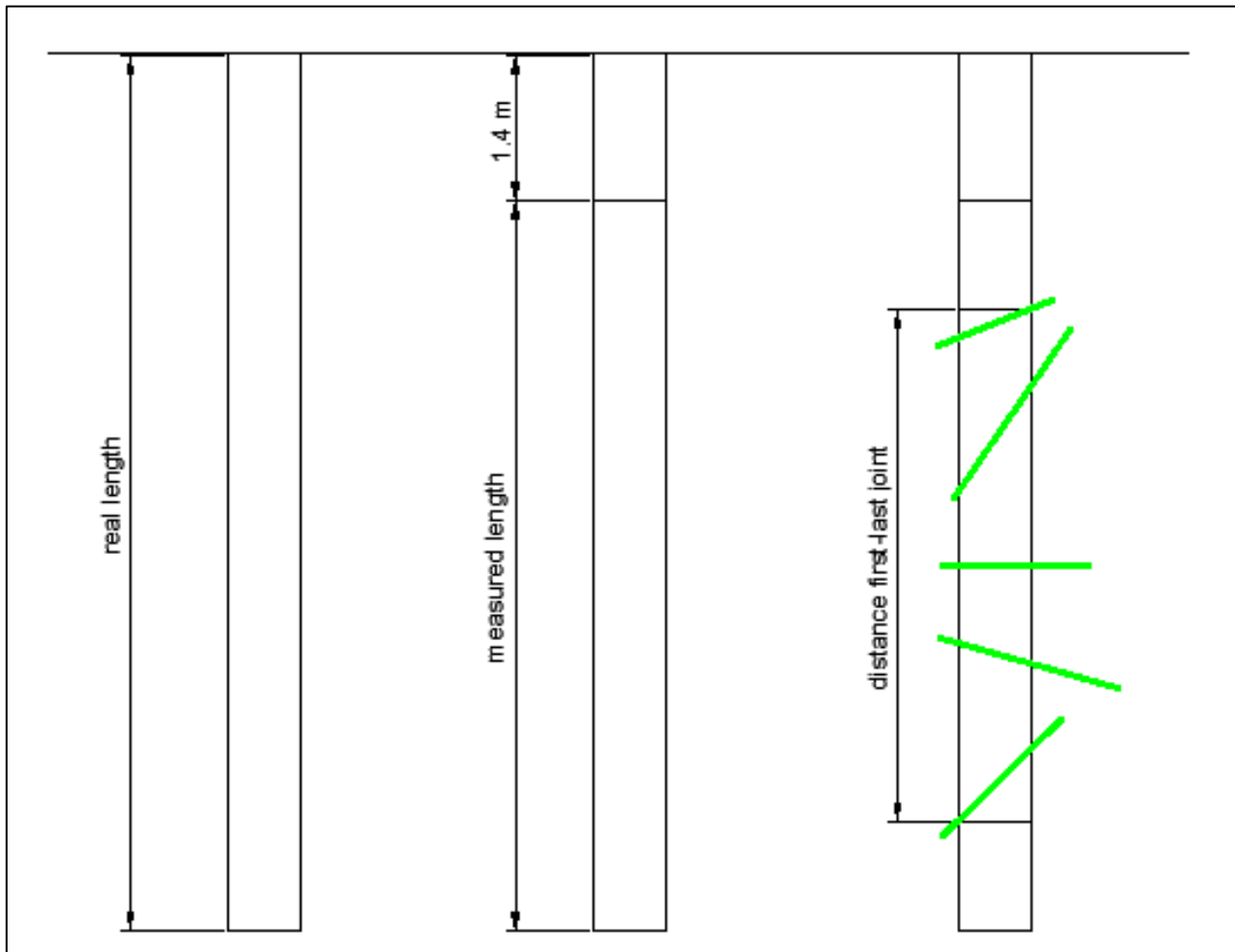


Figure 64: Real length, measured length , distance first last joint.

To obtain the final P_{10} value of the joint sets for the two campaigns, a calculation was performed on each hole and finally the average between the values obtained. Since it was impossible to calculate the trace length with the televiewer, in the final analysis as input data of fracture dimensions was used the value calculated by the trace length analysis that will be explained in the following paragraphs.

Table 12 and Table 13 show the mean value of P_{10} for each campaign

Table 12: P₁₀ measured first campaign.

First campaign						
P₁₀ (1/m)	Mean	Max	Min	Standard Dev.	CV	CV (%)
Sh	1.06	2.39	0.16	0.72	0.68	68.15
ShNE	0.39	0.82	0.08	0.21	0.54	54.30
SvSE	1.37	2.27	0.40	0.45	0.33	32.95
SvNE	0.70	1.74	0.17	0.36	0.51	51.18

Table 13: P₁₀ measured second campaign.

Second campaign						
P₁₀ (1/m)	Mean	Max	Min	Standard Dev.	CV	CV(%)
Sh	1.63	5.00	0.22	1.00	0.62	61.61
ShNE	0.89	3.09	0.07	0.76	0.86	85.65
SvSE	1.74	3.08	0.67	0.59	0.34	33.78
SvNE	1.71	3.17	0.51	0.70	0.41	40.66

It is possible to notice that the highest concentration of fractures in the first campaign is in the Sh and SvSE set while in the second one it is possible to notice the growth of the number of fractures in the NE direction.

The value of P₁₀, since the measured hole length is fixed, depends on the analysis method performed previously on the previous data used during the televiwer analysis.

In Table 28 of Appendix A it is possible to see all the P_{10} values calculated for each hole.

3.4.3.4 Areal fracture intensity

The first index of fracturing intensity on the analysed surfaces is the areal fracturing index P_{21} . It is calculated by the total fracture length of the tracemaps belonging to each set divided by the area of each surface. In Table 14 it's shown the total area for each surface.

Table 14: Total area surfaces.

Blast N.	1	2	3	4	5	6
Area (m²)	528.15	455.85	413.67	402.14	423.68	332.36
Blast N.	7	8	9	10	11	12
Area (m²)	461.37	462.61	405.08	481.339	513.58	391.94

The areal value reported is only the one where it was possible to trace the discontinuities, and not the total value of the surfaces acquired during the first steps of photogrammetry.

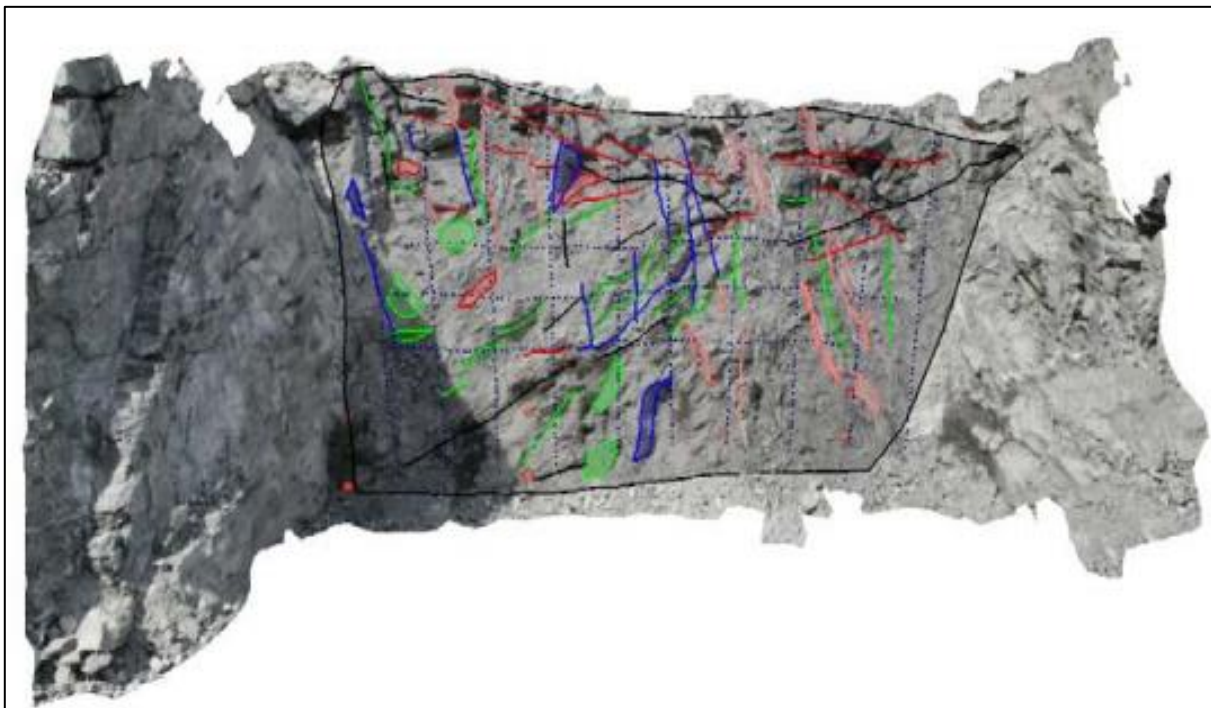


Figure 65: Surfaces taken into consideration in calculation [Bernardini,2020].

The value of the calculated P_{21} are shown in Table 15 and Table 16:

Table 15: P₂₁ measured first campaign.

First campaign				
P₂₁ (1/m)	Sh	ShNE	ShSE	ShNE
Mean (1/m)	0.54	0.03	0.06	0.09
Standard Dev.	0.03	0.01	0.01	0.04
CV	0.06	0.29	0.23	0.47
CV %	6.21	28.62	23.49	46.75

Table 16: P₂₁ measured second campaign.

Second campaign				
P₂₁ (1/m)	Sh	ShNE	SvSE	SvNE
Mean (1/m)	0.45	0.03	0.07	0.13
Standard Dev.	0.16	0.02	0.04	0.03
CV	0.36	0.59	0.51	0.25
CV %	36.33	58.72	51.03	25.32

As can be seen, the greatest concentration of discontinuities is present in the Sh Set and the SvNE Sets. In the second campaign the percentage dispersion values present in some families exceeds 50%.

In Table 27 of Appendix A it is possible to see all the P₂₁ values calculated highwall.

3.4.3.5 Trace length analysis

A very important data used to define the number of fractures generated during the final analysis is the size of the discontinuities present in the rock mass. The data is provided by the analysis of tracemaps previously filtered and imported into the software. The FracMan program allows in an automatic way to generate an empirical cumulative distribution and this operation was performed for each family of discontinuities and separately for the two campaigns. The most representative distribution was the log-normal because it more accurately represents the fracture population.

In Figure 66 and Figure 67 it is possible to see the different graphs for each set and each campaign.

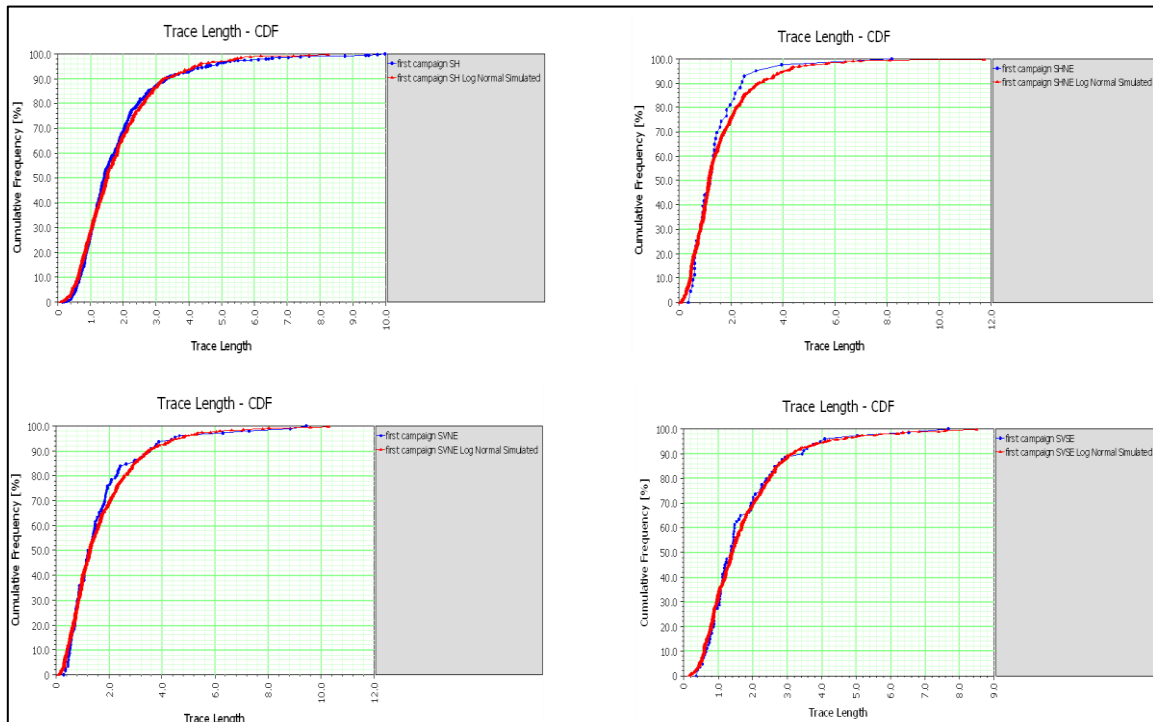


Figure 66: Log- normal distribution from trace length analysis, first campaign.

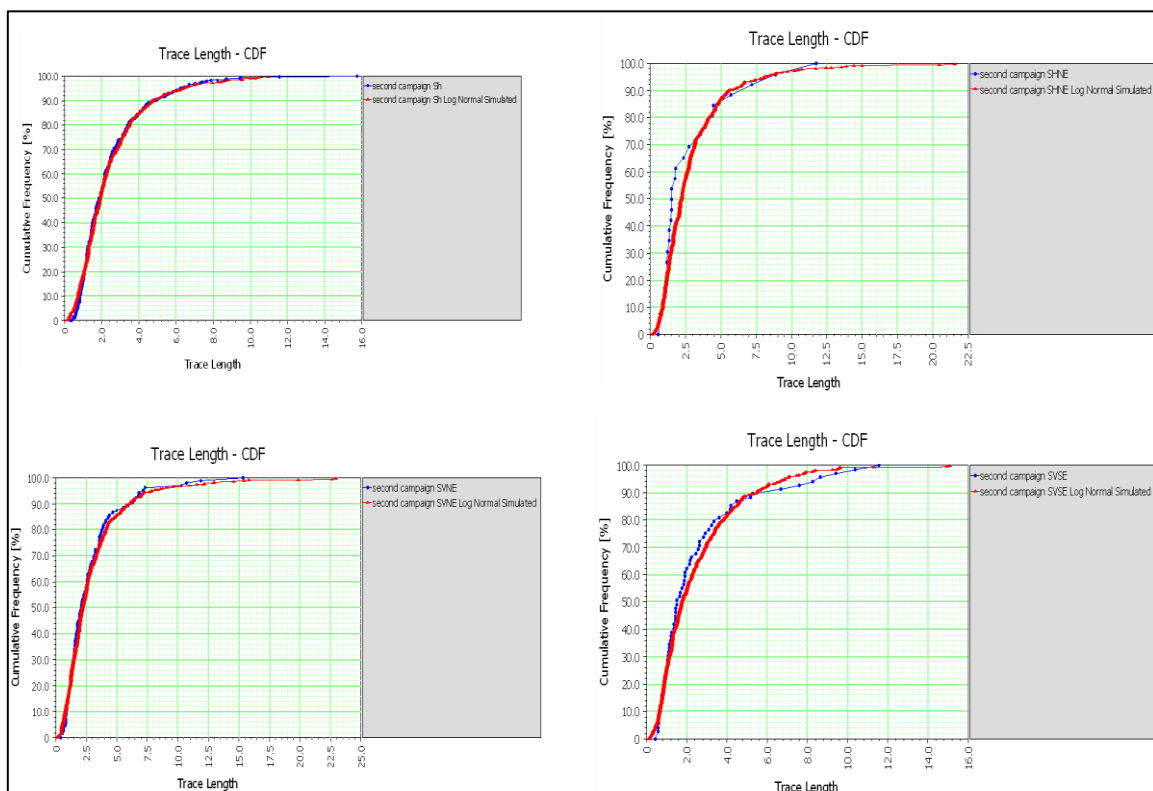


Figure 67: Log- normal distribution from trace length analysis, second campaign.

In Table 17 and Table 18 it is possible to observe the values for the first and second campaign of all the discontinuity sets.

Table 17: Length and radius first campaign.

First Campaign				
Set	Sh	ShNE	SvNE	SvSE
Trace Len Mean	1.82	1.47	1.73	1.75
Trace Len Dev	1.37	1.29	1.57	1.30
Radius Mean	0.80	0.57	0.65	0.78
Radius Deviation	0.54	0.46	0.54	0.51
CV radius	0.67	0.84	0.84	0.72
CV % radius	67.36	83.84	83.62	72.19

Table 18: Length and radius second campaign.

Second campaign				
Set	Sh	ShNE	SvNE	SvSE
Trace Len Mean	2.43	2.89	2.88	2.55
Trace Len Dev	1.87	2.77	2.48	2.49
Radius Mean	1.05	1.04	1.13	0.90
Radius Deviation	0.72	0.91	0.89	0.81
CV radius	0.76	0.89	0.94	0.85
CV % radius	76.29	88.94	93.91	85.49

From this analysis the software generates the average value of trace and radii and their standard deviations (fractures are defined as circular). As it possible to see from the simulation data the trace lengths vary greatly between the first and second campaign; in some cases the difference higher than 1 m. This difference is due to the presence in the first campaign of many discontinuities mapped with length less than 1.1 m. These values have a great influence on the size of the radii that will simulate

the size of the fracture discs. Having reduced dimensions a greater number of discontinuities will have to be generated due to the minor probability of having an intersection fracture/holes or fracture/surfaces.

3.4.4 Model simulation

3.4.4.1 Region box definition

The first step for the model generation was to define two region boxes suitable to contain all the data imported from the two previous analyses (televiewer and photogrammetry). The dimensions of the two regions were chosen to have the same volume and therefore to have a volumetric fracture value P_{32} proportional to the number of fractures generated.

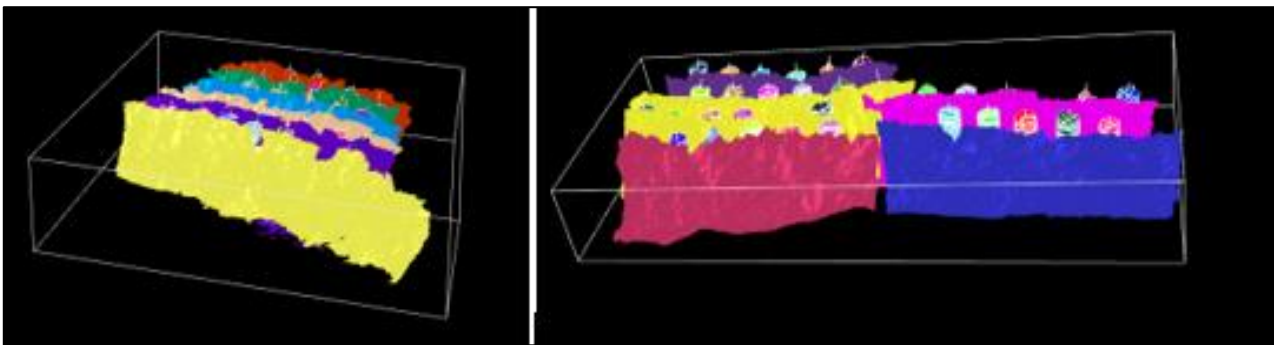


Figure 68: Region box containing all the objects.

The dimensions taken into consideration are 34x33x16 m for the region box created for the first campaign and 54x22x15.1 m for the second one. The dimensions of the regions were chosen in order to have the same volume and to be able to compare the fractures generated in the two different campaigns. The dimensions of the first one could have been smaller to contain all the data, but they have been increased due to the impossibility of having a smaller volume than the second one.

3.4.4.2 Iterations

The FracMan software produces a random seed that will be used as a base in the algorithm; this seed changes at each iteration. During iterations our seed is kept constant to generate at the same locations the fracture centres. The final result depends on the accuracy of this process, because the generation of fractures with different seeds in the iterative process can lead to an inconsistency in the final data. Three values of seeds are used to have a database on the number of fractures to generate. The increase of iterations with different seeds produces an increase in the accuracy of the final data, but consequently an increase of time in data processing. This is due to the impossibility to perform the

process automatically and therefore at each iteration the seed have to be inserted manually. The command used was "*set random seeds*" in the toolbars.

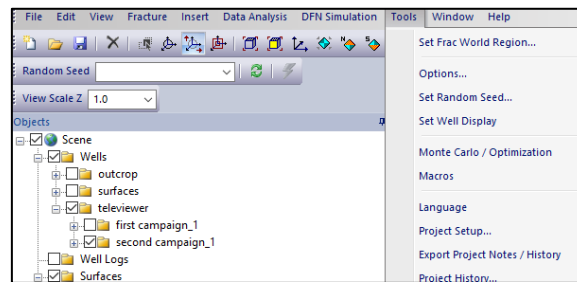


Figure 69: Set Random Seed Tool.

The three initial values chosen were 11111, 22222, 12345 and were applied before fracture generation for P₁₀ and P₂₁.

The fracture generation of each set is repeated with different values until the average of the simulated linear and areal fracture intensities reaches values less than 5 % error from those measured. Since photogrammetry and analysis with the borehole optical televiewer are two different analyses, they produce different fracture values to be simulated.

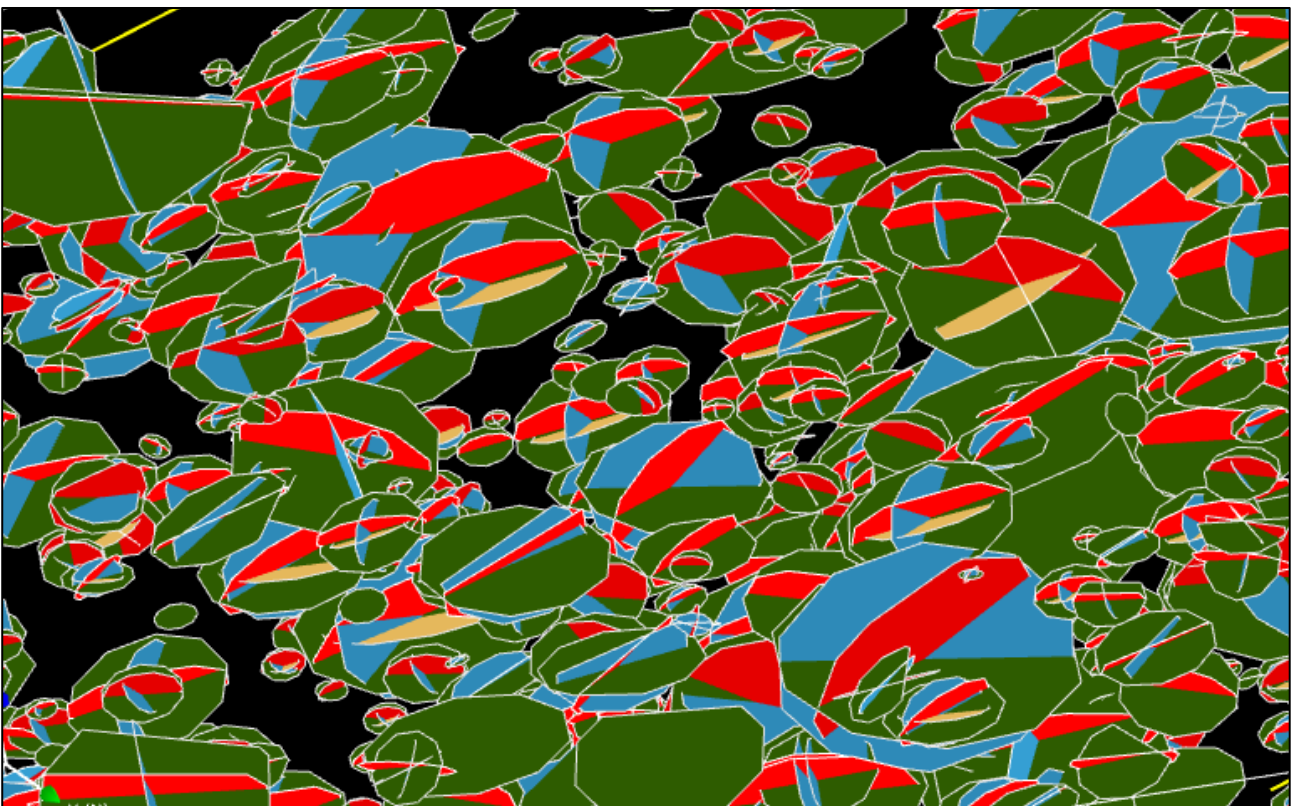


Figure 70: Fracture from different sets with same seed.

In Figure 70 you can see the influence of the initial seed in the algorithm. The fractures defined with different colours belong to different sets (Dark green Sh, Yellow ShNE, Red SvNE, Blue SvSE). Being the initial seed the same (11111) the fractures are generated in identical points.

3.4.4.3 Fracture generations

The generation of the fractures is preceded at each iteration by the insertion of the desired seed. The FracMan software allows, through the command "define a new set", to generate fractures by entering the values of the mean pole, type of distribution, geometric parameters, the major axis (Table 8 and Table 9) and the size of the fracture radius (Table 17 and Table 18). The "geometric" generation set was chosen during the analysis because allows to generate discontinuities within the desired region.

After the selection from the bar of the tools a window with 4 tabs comes opened and it is possible to insert the wished values inside the simulation.

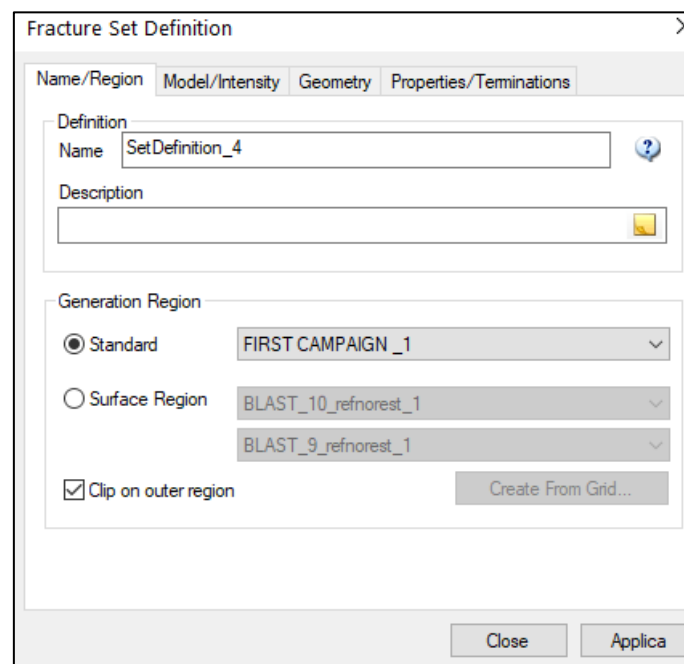


Figure 71: Fracture set definition window.

In the first visualized page it is possible to rename the set of simulation and it is possible to choose the region box in which to generate the fractures (Figure 71). In this study, fractures were generated in two different regions (section 3.4.4.7).

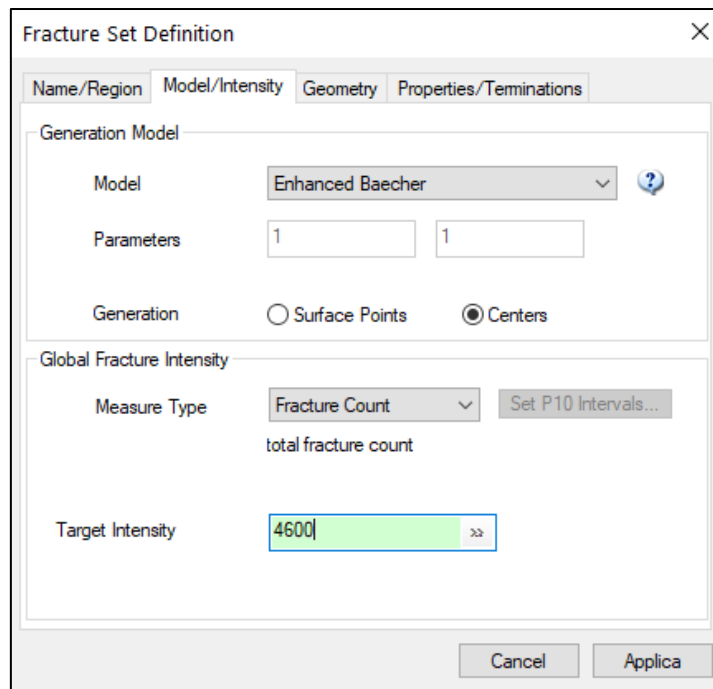


Figure 72: generation model of the set fracture.

In the second page it is possible to insert the number of fractures to generate and the localization algorithm. The algorithm used in this study is the Enhanced Baecher which positions the centres uniformly in space using a Poisson distribution. This decision was taken based on the observation of the tracemaps that present a random and not clustered distribution.

The Poisson distribution is a discrete probability distribution that present the probability of a given number of events, in this case the position of the centre of the fracture, in a fix interval of space where the constant mean rate is known.

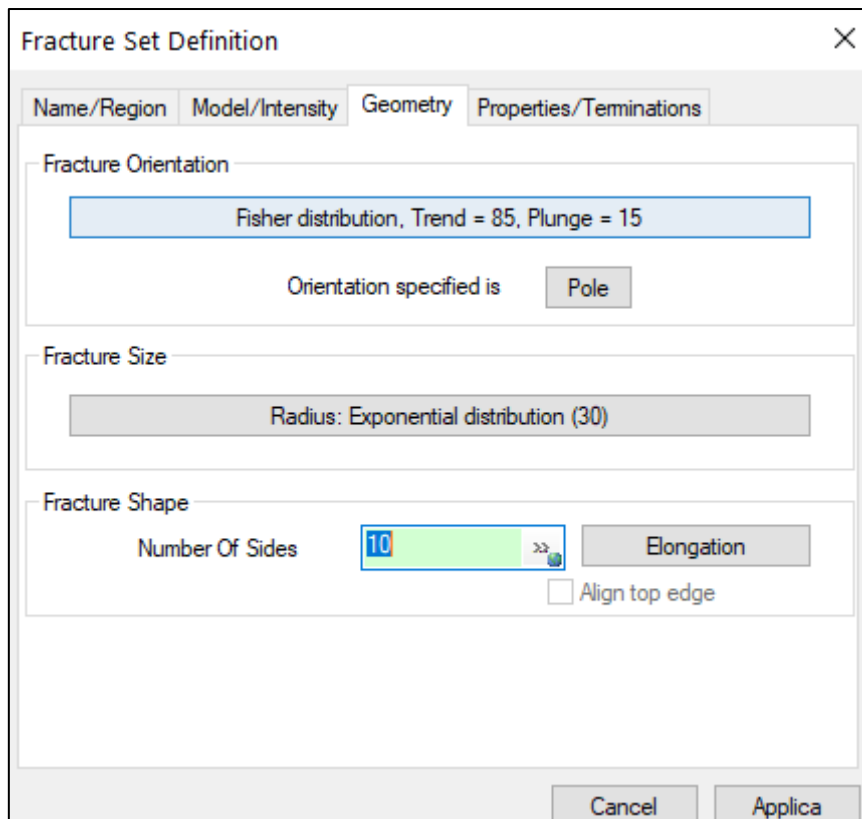


Figure 73 :Fracture properties.

In the third page, using the fracture orientation (Figure 73) it is possible to define to which set the discontinuities belong, entering the type of distribution, the geometric values and the trend and plunge values of the mean pole (Figure 74).

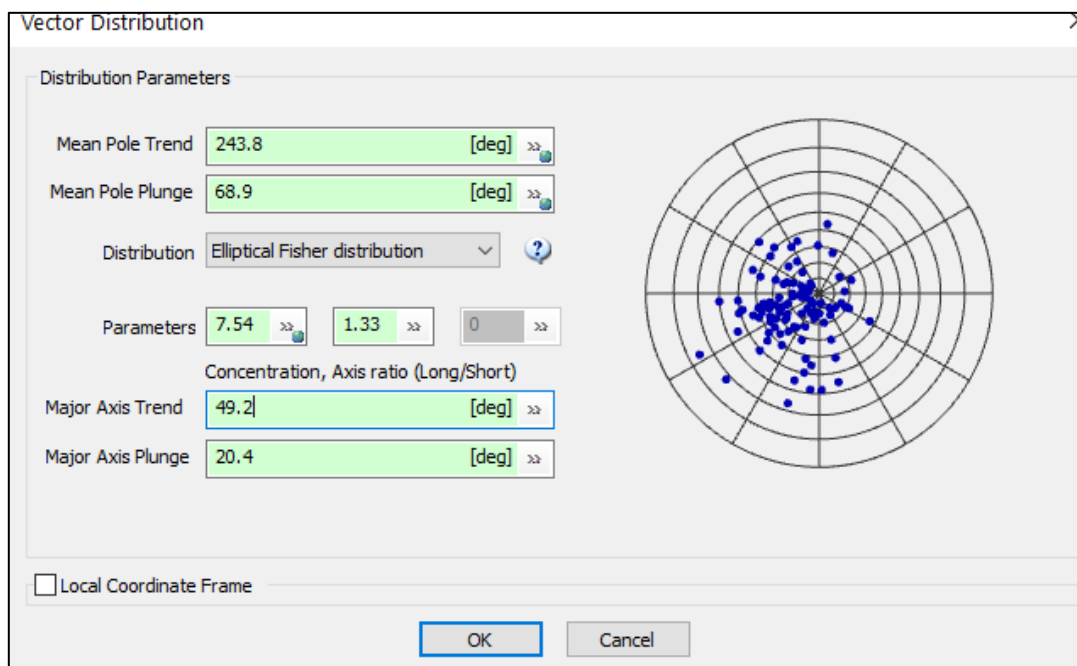


Figure 74: Set properties.

Using the command *Fracture size*, it is possible to insert the type of distribution and the data of the mean radius and the standard deviation (data derived from the trace length analysis paragraph).

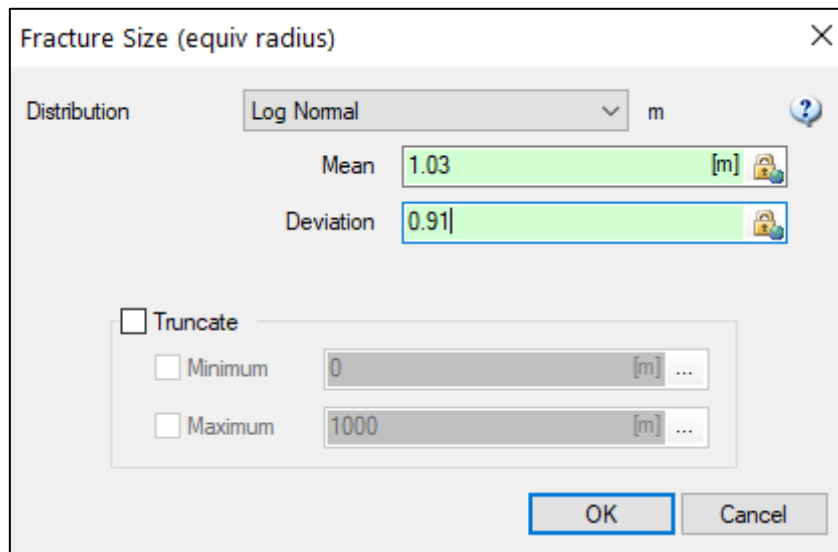


Figure 75: Fractures dimensions.

3.4.4.4 P₂₁ Calibration

The calibration of P₂₁ was done iteratively starting from the intersection of the first set of generated fractures and the surfaces of the present within the region box take into consideration. The iteration continued until the error between the simulated value and the measured value was less than 5 % (Figure 76). The output values include both P₂₁ and P₃₂ values.

		1st iteration			2nd iteration			3rd iteration			
	seeds	P21 traced	Fracture number	P21	ERROR	Fracture number	P21	ERROR	Fracture number	P21	ERROR
SH	11111	0.54	792.00	0.09	82.47	4150.00	0.48	10.39	4600.00	0.55	-1.87
	22222	0.54	4600.00	0.58	-8.82	4150.00	0.52	2.08			
	12345	0.54	4150.00	0.48	10.55	4600.00	0.54	-0.06			

Figure 76: Iteration to reach less than 5 % of error.

The procedure has been repeated for all the seeds in order to obtain a mean value that does not depend on the position in which the program places the centres of the fractures.

The P₂₁ final value are shown in the following tables:

Table 19: P₂₁ calibration.

First campaign					
Sets	Seed	P ₂₁ traced (1/m)	Fracture number	P ₂₁ (1/m)	ERROR (%)
Sh	11111	0.54	4600	0.55	-1.87
	22222	0.54	4150	0.52	2.08

	12345	0.54	4600	0.54	-0.06
ShNE	11111	0.03	330	0.03	4.43
	22222	0.03	520	0.03	-3.38
	12345	0.03	290	0.03	0.34
SvSE	11111	0.06	650	0.06	2.78
	22222	0.06	800	0.06	2.55
	12345	0.06	580	0.07	-2.06
SvNE	11111	0.09	750	0.09	1.26
	22222	0.09	1040	0.09	3.51
	12345	0.09	670	0.09	3.54

Table 20: P_{21} calibration.

Second campaign					
Sets	Seed	P_{21} traced (1/m)	Fracture number	P_{21} (1/m)	ERROR (%)
Sh	11111	0.45	2300	0.45	0.92
	22222	0.45	2110	0.45	1.33
	12345	0.45	2550	0.46	-0.98
ShNE	11111	0.04	150	0.04	-0.83
	22222	0.04	150	0.03	1.21
	12345	0.04	70	0.03	2.00
SvSE	11111	0.08	320	0.08	-4.93
	22222	0.08	430	0.07	3.70
	12345	0.08	395	0.07	0.14
SvNE	11111	0.13	430	0.12	4.68
	22222	0.13	515	0.12	4.17
	12345	0.13	600	0.13	-3.56

3.4.4.5 P_{10} Calibration

The calibration of P_{10} values was performed using a procedure similar to that of P_{21} , this time not using the surfaces for the intersection, but the holes used for the televiewer analysis. The average value was calculated to eliminate the error related to the generation of the fracture centers.

The P_{10} final value are shown in the following table:

Table 21: P_{10} calibration.

First campaign					
Sets	Seed	P_{10} traced (1/m)	Fracture number	P_{10}(1/m)	ERROR (%)
Sh	11111	1.06	8250	1.06	-0.43
	22222	1.06	9400	1.04	2.16
	12345	1.06	8500	1.04	2.35
ShNE	11111	0.39	4600	0.40	-2.45
	22222	0.39	5000	0.38	2.73
	12345	0.39	4900	0.40	-1.98
SvSE	11111	1.37	28000	1.39	-1.64
	22222	1.37	28000	1.32	3.89
	12345	1.37	28000	1.32	4.00
SvNE	11111	0.70	12800	0.71	-1.18
	22222	0.70	12800	0.68	2.34
	12345	0.70	14500	0.70	-0.40

Table 22: P_{10} calibration.

Second campaign					
Sets	Seed	P_{10} traced (1/m)	Fracture number	P_{10}(1/m)	ERROR (%)
Sh	11111	1.63	7850	1.61	1.46
	22222	1.63	7850	1.57	3.85
	12345	1.63	8460	1.61	0.99
ShNE	11111	0.89	3300	0.89	0.33
	22222	0.89	3525	0.90	-0.84
	12345	0.89	3525	0.88	1.13
SvSE	11111	1.74	19270	1.75	-0.34
	22222	1.74	19270	1.72	1.36
	12345	1.74	19270	1.71	1.70
SvNE	11111	1.71	13130	1.72	-0.69
	22222	1.71	13130	1.76	-2.66
	12345	1.71	13130	1.65	3.33

3.4.4.6 Results

The results of the average fractures generated during the simulation for P_{10} and P_{21} are shown in Table 23:

Table 23: Mean value of calibration fractures.

	First campaign			Second campaign		
	P_{10}	P_{21}	P_{10}/P_{21}	P_{10}	P_{21}	P_{10}/P_{21}
Sh	8717	4450	1.96	8053	2320	3.47
ShNE	4833	380	12.7	3450	123	28.04
SvSE	28000	677	41.35	19270	382	50.44
SvNE	13367	820	16.3	13130	515	25.49

In Appendix B it is possible to see the fractures generation with the mean values of P_{10} and P_{21} of the two campaigns.

As can be seen, the linear fracturing values are much higher than the areal fracturing values. This can be caused by different factors:

- **Dimension of the region box:** the volume of the region box affects the amount of fractures that must be generated for intersections to occur. The probability of a fracture intercepting a surface is much higher than that of intercepting a borehole. This is due to the fact that the region boxes must contain all the objects being analysed and the surfaces being the "largest" objects, there are areas at the boundaries without boreholes, but in which they are in any case generated fractures.
- **Observation scale:** the analysis with photogrammetry takes place at the level of the free surface, while the analysis carried out with the borehole optical televiewer inside the rock mass. The P_{21} values, measured in situ, are also lower than the measured P_{10} values.
- **Dip angle and dip direction:** for a surface (considering it flat) there is only one value of dip angle and dip direction such that the generated fractures are parallel and therefore an intersection is impossible, while for the holes almost all vertical fractures have a very low probability of being intercepted.

Moreover, it is possible to notice for very similar values of P_{21} and P_{10} to be reached with the simulation that the number of fractures has a different trend. Sub-vertical fracture families must be generated in greater number than sub-horizontal fractures in linear fracturing because of the low probability of intercepting holes. Sub-horizontal fractures are in a range of perpendicularity to the holes, so the probability of intercepting increases.

An interesting datum different from the previous analysis is the number of fractures to be generated between the first and the second campaign. It is possible to notice that in the first campaign there are higher values than in the second one even if the measured values are lower. This is due to two different factors:

- **Dimension of region box:** as in the previous consideration, the region box influences the fracturing values, also between the two campaigns. Having taken the two volumetric dimensions equal and being the dimensions of the objects inside the boxes different, was taken as minimum volume that of the largest region (second campaign). For this reason, subsequently, the dimensions of that of the first campaign were increased. By increasing the dimensions have been created empty volumes, in which neither borehole nor surfaces are present, and fractures are simulated.
- **Dimensions of fracture radii:** The size of the radius of the fractures is one of the values that most influence the simulation. In the first campaign having the fractures with a very small radius they have little probability to intercept the surfaces or the boreholes. The very low radius values are due to the presence of many fractures smaller than 1.2 m in size. Moreover, having very short radii, it is unlikely that the same fracture can intercept two different objects during the calculation of P_{10} and P_{21} .

To understand how much the radii of the fractures influence the final result, a test was carried out by inserting the data deriving from the trace length analysis of the second campaign in the simulation of the first one. In Table 24 we can observe the input data and the results of the test.

Table 24: Test with different radius.

	Sh first campaign	Sh test
Seed	11111	11111
Distribution	Elliptical Fisher	Elliptical Fisher
Mean pole (tr/pl)	243.8, 68.9	243.8, 68.9
Major axis (tr/pl)	49.3, 20.4	49.3, 20.4
k1	7.54	7.54

k2	1.33	1.33
Radius Mean (m)	0.80	1.05
Radius Deviation (m)	0.54	0.72
N. Fractures	8250	8250
P10 (1/m)	1.07	1.85

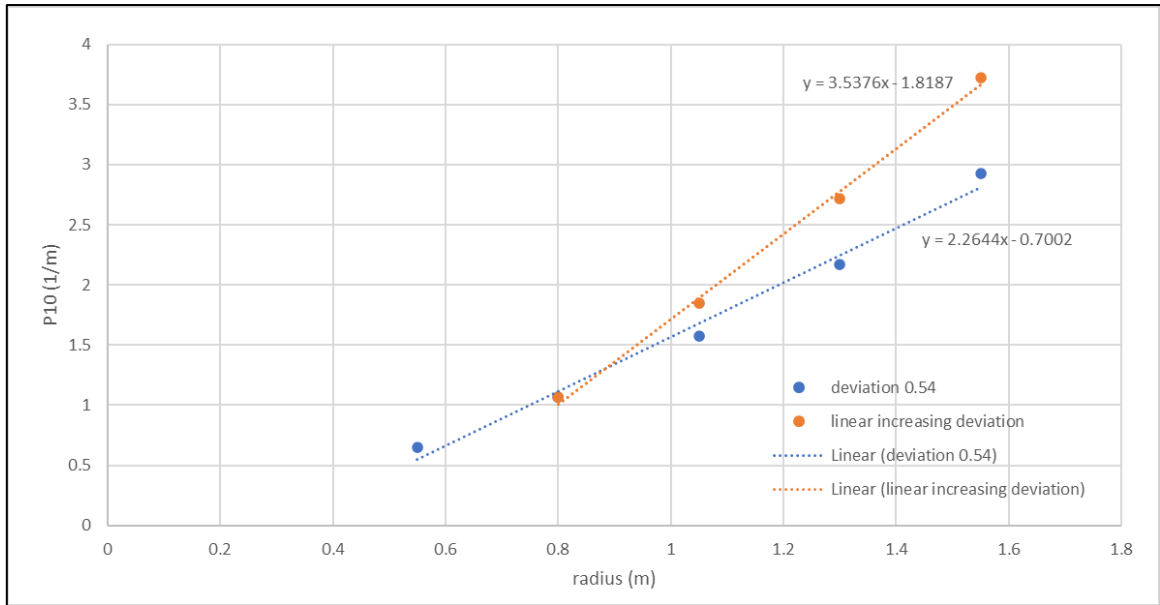


Figure 77: P₁₀ in function of the radius (mean and deviation).

In Figure 77 it is possible to observe how the values of P₁₀ with iteration 11111 vary with the variation of the average value of the radii and with the variation of the standard deviation. It is possible to notice a linear trend between the values of P₁₀ and the dimension of the fractures.

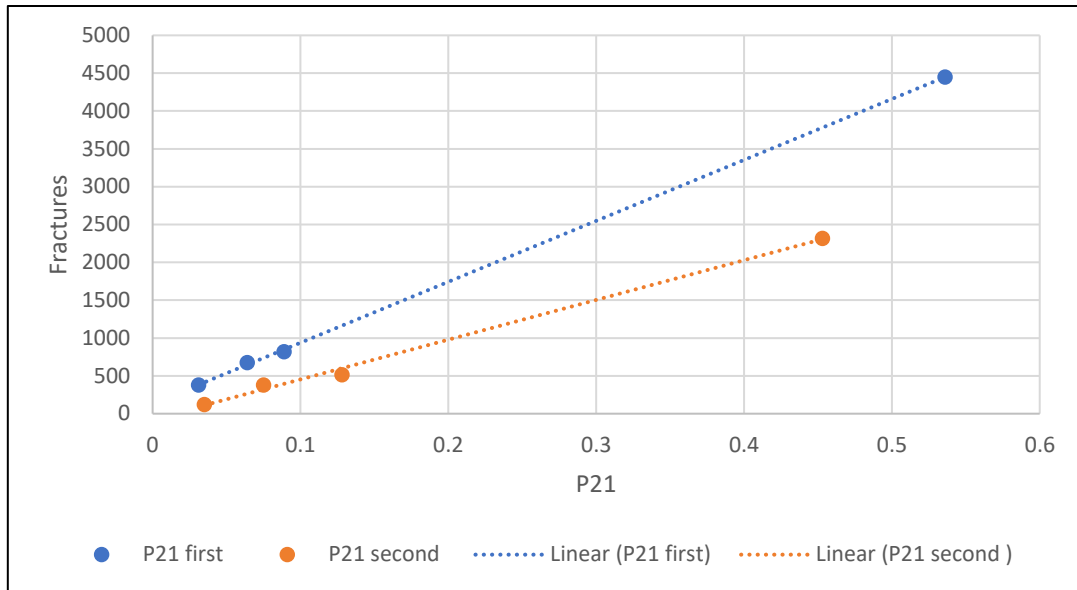


Figure 78: P_{21} in function of the fractures.

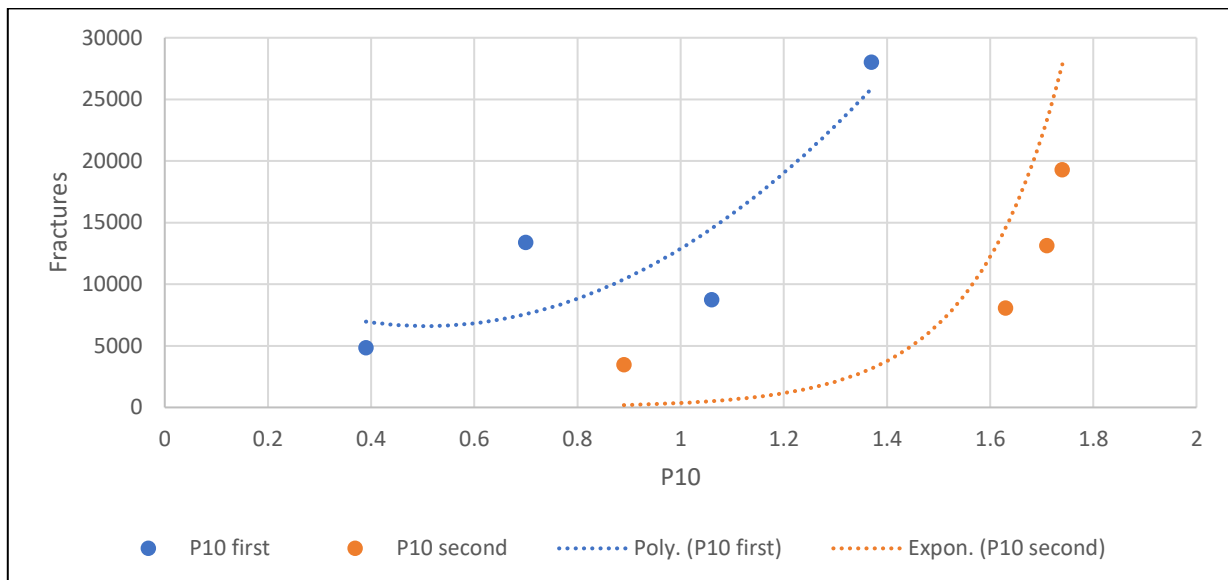


Figure 79: P_{10} in function of the fractures.

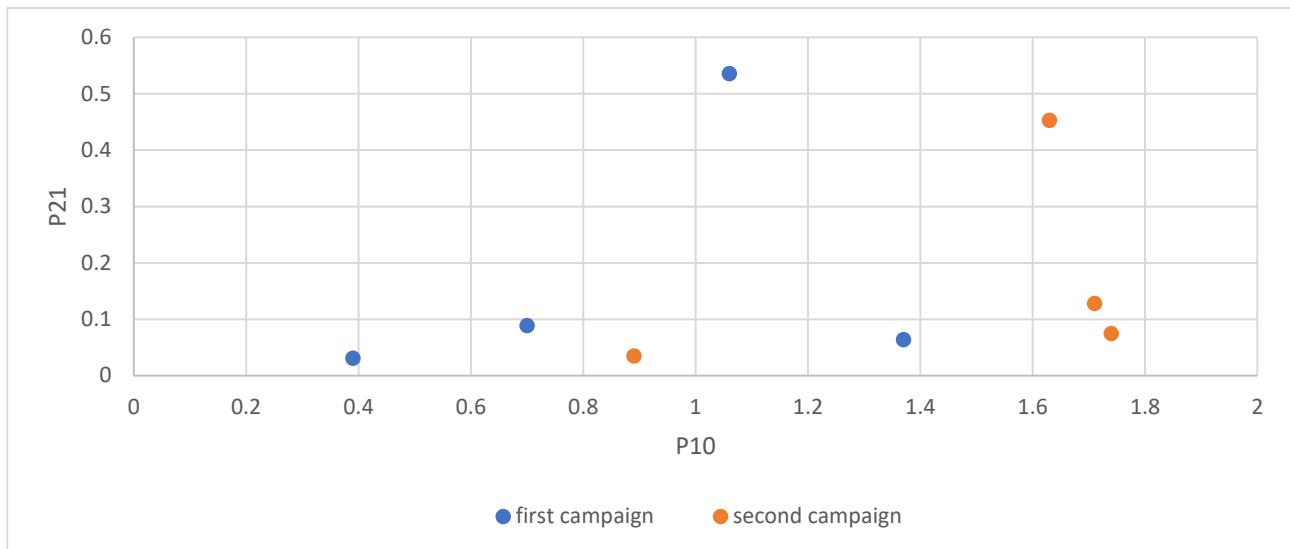


Figure 80: Graph P₁₀-P₂₁.

3.4.4.7 Model generation

Model generation was performed using the average number of fractures computed using data derived from the three seeds. The procedure to generate the fractures was performed in the same way as in the section 3.4.4.3, this time not using any seed to generate fractures at random points. The seed was not included so as not to provide an equal base input to the distribution algorithm, thus, not to have fracture centres at the same point (Figure 70).

The procedure was performed for the two separate campaigns and for P₁₀ and P₂₁ values. As can be seen in both campaigns, the models with P₁₀ values have a higher fracture intensity and therefore a smaller block size.

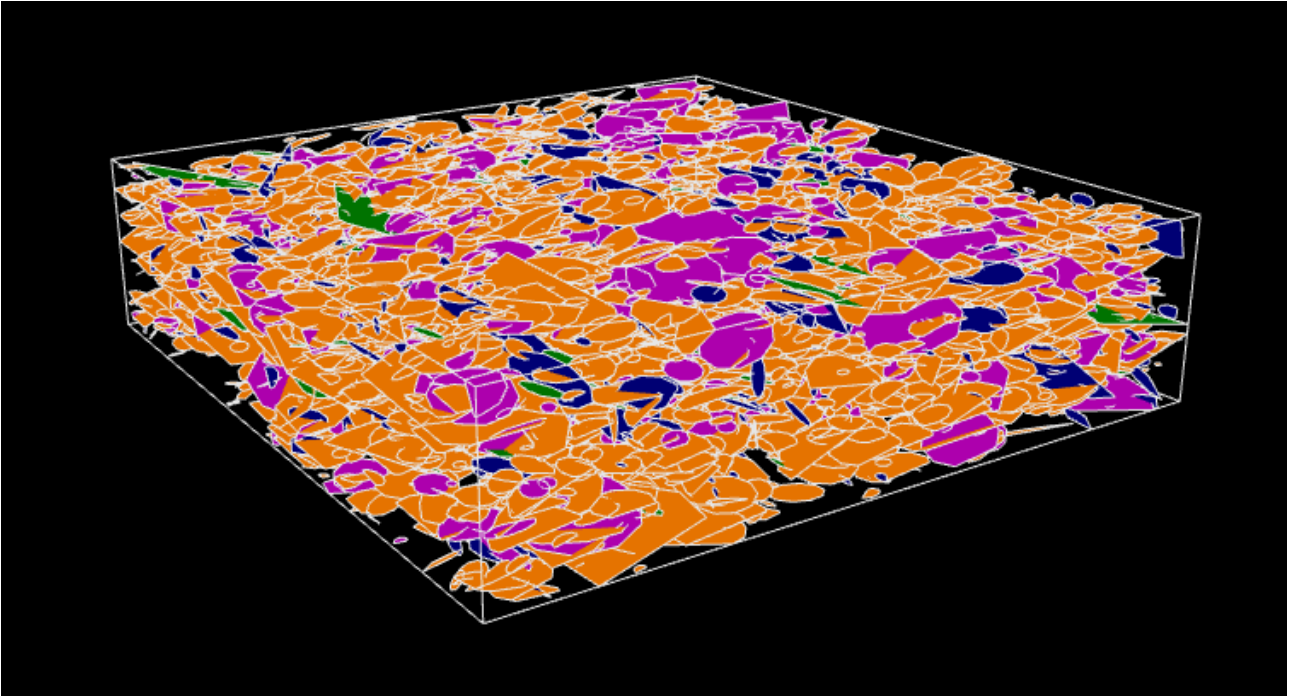


Figure 81: Model simulation with P_{21} value first campaign.

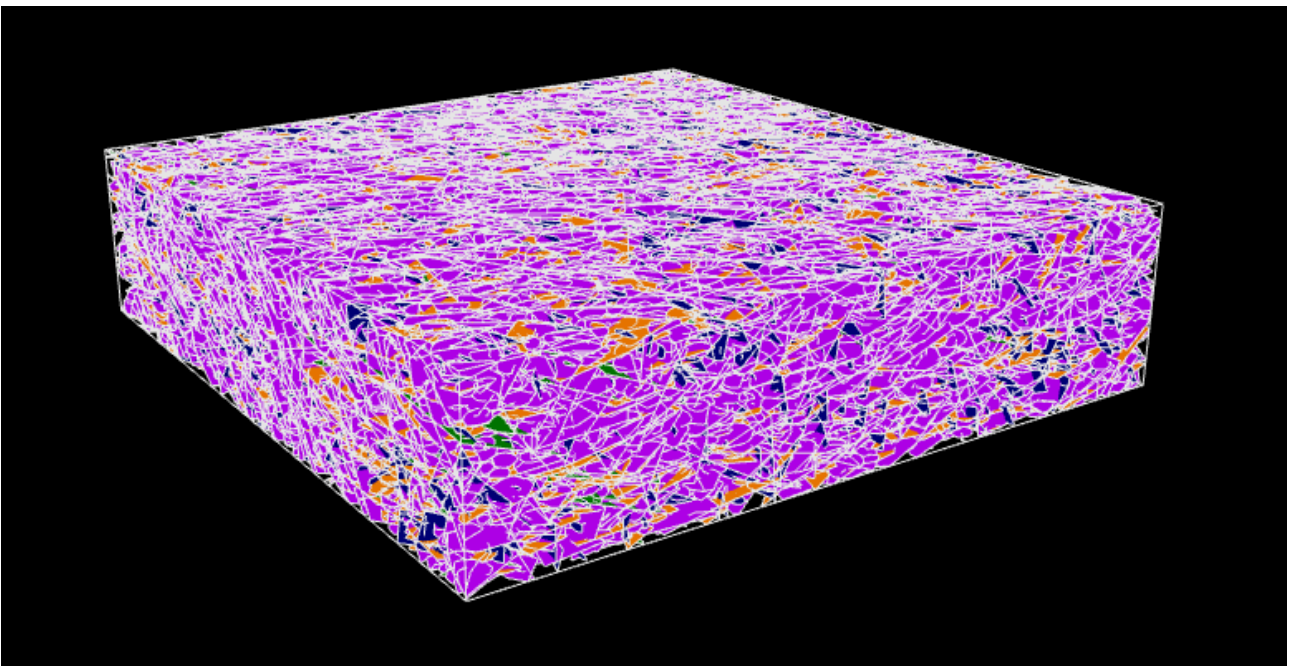


Figure 82: Model simulation with P_{10} value first campaign

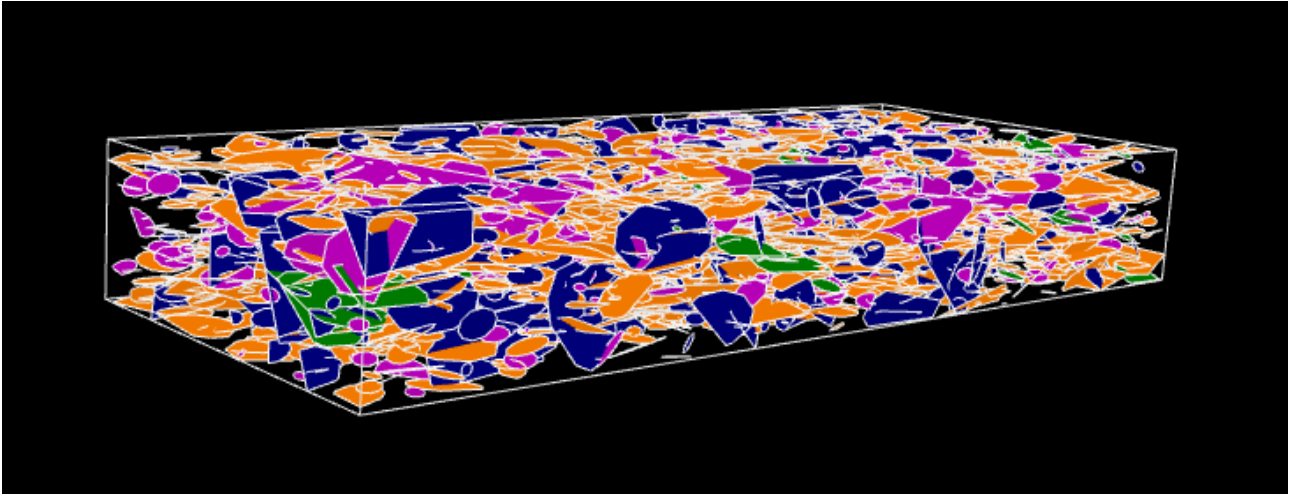


Figure 83: Model simulation with P_{21} value second campaign

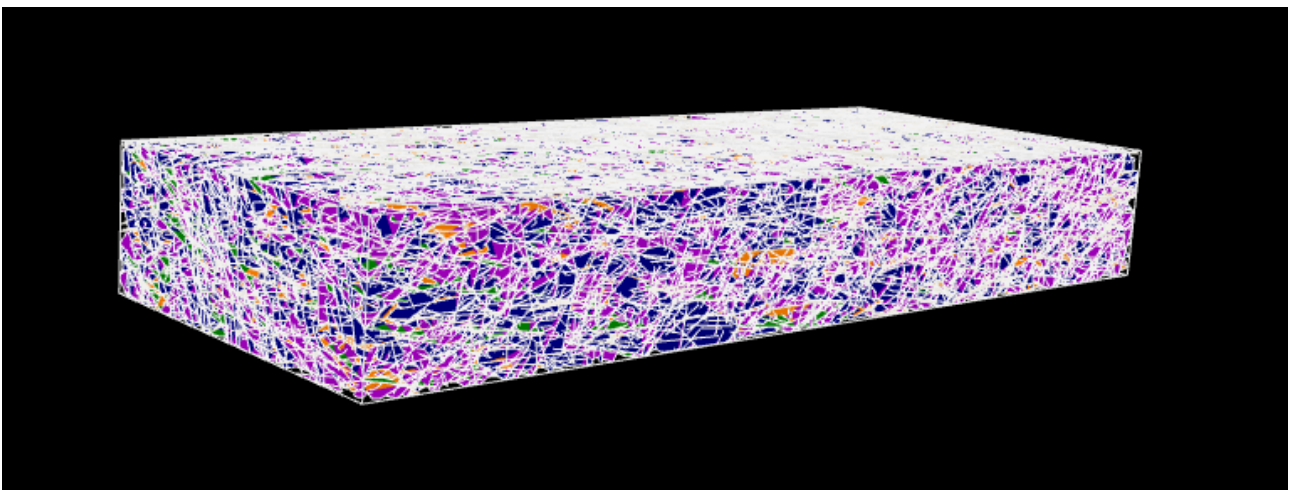


Figure 84: Model simulation with P_{10} value second campaign

3.4.5 In-situ block size distribution (IBSD)

The in-situ block size distribution is an excellent method to optimize the work to be carried out on the rock mass and to define its mechanical properties. Knowing the block size allows to understand the interaction between them and to know the general mechanical behaviour. In this study the FracMan software allows to generate a discrete fracture network (DFN) based on the MDS (Multi-Dimensional Spacing) algorithm.

The calculation of the in-situ block size distribution was done by simulating the previously calculated fractures (Table 20), through P_{21} and P_{10} , in the box region containing the surfaces and holes of the campaign under consideration (Figure 68).

The Multi-dimensional spacing algorithm works by using the number of points as first input value, and the number of blocks to be generated with the calculate spacing. For each generated point, 3 intersection lines are created inside the border of the region box with 90° angles between them. The intersection between the lines and the fractures are recorded with their position in the space. This allows a distribution to be created in multiple dimensions of the spacing. The spacing probability distributions are multiplied together using Monte Carlo sampling techniques to produce a frequency distribution of block volumes and surface areas [FracMan, 2020].

The volume of the block is given by thee formula (for the Monte Carlo computation):

$$Volume = X_i * Y_i * Z_i$$

Where the factor are the spacing values at random with selection probability proportional to their frequency [FracMan, 2020].

In the following table is possible to see the value used as input in the calculation:

Table 25: Input value for MDS analysis.

	First region box	Second region box
Density (kg/m3)	2721	2721
No. points (P₂₁)	1500000	1500000
No. points (P₁₀)	2000000	2000000
No. blocks	100	100
1° direction (tr°/pl°)	0 , 0	0 , 0
2° direction (tr°/pl°)	0 , 90	0 , 90
3° direction (tr°/pl°)	90 , 0	90 , 0

The simulations performed with the fractures generated for P₂₁ values took approximately 2 hours, while those for P₁₀ were performed in 23 hours.

3.4.5.1 Results

The result of the analysis is a cumulative volumetric distribution of rock blocks. Then, in Figure 85, it is shown a graphic representation of the fragment size distribution resulting for the 4 DFNs, assuming that each fragments has a spherical shape.

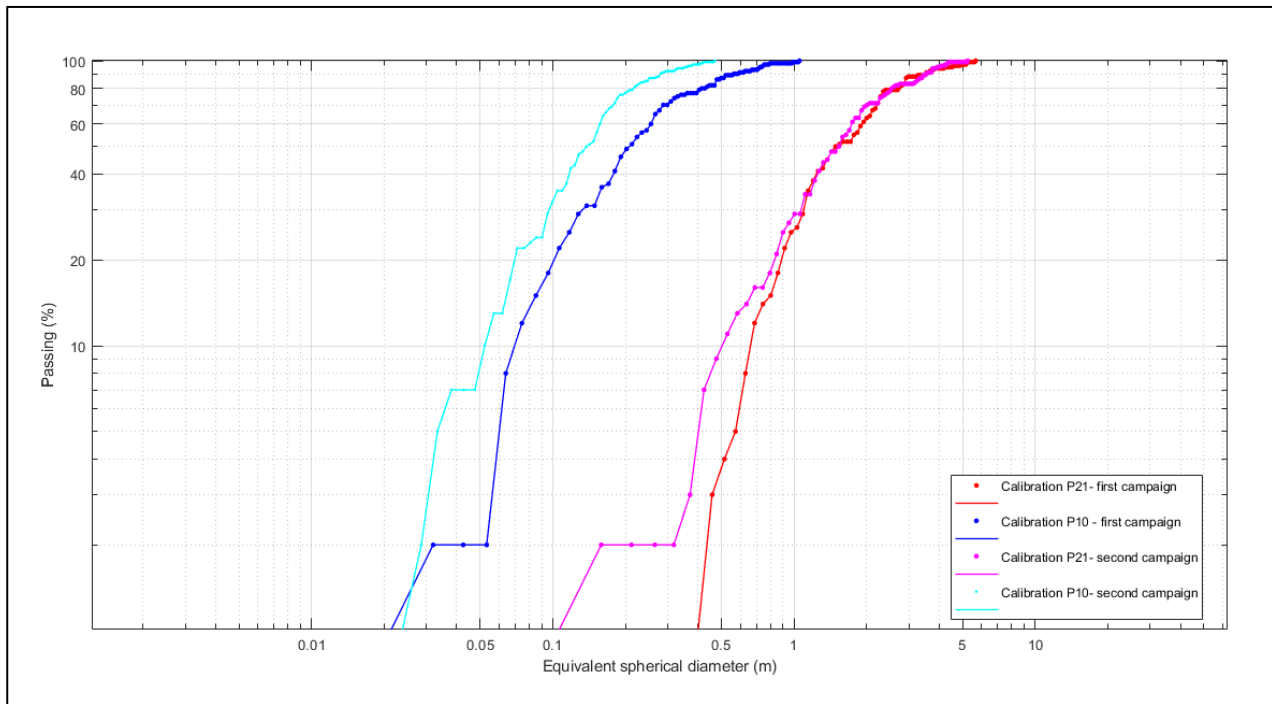


Figure 85: Graph equivalent spherical diameter (log-log).

It is possible to visualize in Figure 85 the 4 different curves related to the equivalent diameters of the rock blocks, using the values of P_{21} and P_{10} of each campaign. The data from the photogrammetry show larger diameters than the one obtained from the televiewer due to the number of fractures simulated.

The value simulated from the areal fracture intensity show a similar trend and very similar equivalent diameter. The two factors that can have a compensating effect on each other can be:

- **The number of fractures generated:** the P_{21} of the first campaign require a bigger number of fractures to be reached.
- **The diameter of the fractures:** the fractures, being of small diameter in the first campaign, may not be intercepted by the lines generated from the random points inserted as input for the multi-dimensional spacing algorithm.

A significant increase in random points provided output data very similar to those in the Figure 87, so it can be inferred that the algorithm works optimally for larger diameters and for greater fracture interactions.

The values for the P_{10} curve are discordant to the fracture number, which may be due to the radius calculated during the trace length analysis. Since the diameters are small, they are less likely to interact with each other and be intercepted by the generated lines of the algorithm. This leads to an increase in the acquired spacing and produces an increase in the size of the rock block.

Table 26: Median and maximum diameter for the two type of detection for each campaign.

	First campaign		Second campaign	
	P_{21}	P_{10}	P_{21}	P_{10}
X_{50} (m)	1.53	0.22	1.58	0.14
Φ_{max} (m)	5.72	1.06	5.30	0.48

The median and maximum equivalent diameter values for each campaign and each method used for data acquisition are shown in the Table 26. The values from the first campaign can be used for blasting aim, although the value derived from the televiewer is relatively small. In the case of the second campaign, only the P_{21} values can be used for blasting aim, because the maximum diameter of P_{10} is smaller than the maximum size usually detected during the blast.

4 Conclusions

The following study presents the elaboration of data from two different acquisition methods to define the in-situ block size distribution in the El Aljibe area (Almonacid de Toledo). Photogrammetry and borehole optical televiewer are the two methods used to acquire a conspicuous database of fractures that are visible on the blast highwall and on the boreholes inner walls. The creation of the DFNs and the calculation of the in-situ block size distribution was performed using the FracMan 7.90 software developed by Golder Associate Inc.

The study was carried out on 12 blasts at El Aljibe quarry, site that produces high volumes of aggregate that are mainly used for railway ballast production. Discontinuities were manually mapped on twelve 3D models of the blasts' highwall using ShapeMetriX 3D, and on 57 boreholes using WellCAD software. The discontinuity sets present are four:

- Sub-horizontal (Sh)
- Sub-horizontal in North-East direction (ShNE)
- Sub-vertical in North-East direction (SvNE)
- Sub-vertical in South-East direction (SvSE)

The use of two different methodologies allows measurements to be made at different scales, by this way, the discontinuity sets can clearly defined. The discontinuity sets were defined in terms of orientation, intensity, spatial and length distribution. The intensity values, P_{10} (linear fracture intensity) and P_{21} (areal fracture intensity), and the fracture radii (derived from trace length analysis) were used as input to the creation of discrete fracture network that base on the Baecher distribution algorithm to define the number of fractures to be simulated in each models.

From the DFN, the in-situ fragments' volumes distributions were generated using a multi-dimensional spacing algorithm and subsequently processed through MATLAB software to define the equivalent block diameters distributions. Four size distribution curves were generated: two for acquisition campaign and two for each data-acquisition method. The graphs show a very similar trend, highlighting how the difference in acquisition scale affects the size values but not the distribution curve trend. This is due to the difference in intensity of fractures obtained by the two acquisition methods. In the analysis of the images coming from the televiewer probe, there is a supernumerary of fractures, generated by the tracing of furrows produced by drilling and intersection of holes with micro-fractures that do not affect the mechanical behaviour of the rock mass. Photogrammetry allows the mapping of clearly visible fractures, but not those that doesn't reach the highwall. Thus, with the

first method there will be an overestimation of the number of fractures, while in the second method there will be an underestimation.

The televiewer analysis does not allow fracture length to be defined, so it cannot be used individually for analysis, so for this factor and the more realistic in-situ block size distribution result, photogrammetry is considered to be the more complete method.

5 References

- [Bernardini, 2019] Bernardini, March 2019. Application of LiDAR and photogrammetry methods at El Aljibe quarry (Toledo, Spain) to characterize the rock mass for fragmentation prediction in rock blasting through Kuz-Ram and xp-frag models
- [FracMan 7.90] FracMan 7.90, 2020. Golder Associate inc.
- [MATLAB, 2019] MATLAB R2019b. MathWorks, Inc.
- [Enrile, 1981] Enrile, J. H. (1981). Evolución microestructural de rocas cuarzo-feldespáticas como resultado del aumento de la deformación en la milonita de Toledo
- [Segarra, 2018] Segarra, P., Pérez Fortes, A.P., Fernández, A., Gomes, T., Gao, X., 2018. Geomechanical models of El Aljibe tests blasts from measurements of the free face with photogrammetry and LiDAR
- [Alt, 2017] ALT-Advanced Logic Technology (2017). WellCAD software 5.1
- [Slob, 2010] Slob, S., (2010). Automated rock mass characterization using 3-D terrestrial laser scanning.
- [WellCAD] WellCAD™ 5.1 user manual
- [Hack, 2003] Hack, H.R.G.K., 2003. Discontinuous rock mechanics.
- [Rock mechanics, 2019] Slides “outline of rock mechanics”, Peila Daniele 2018/2019, Politecnico di Torino
- [Gomes, 2017] Gomes, T., Pérez Fortes, A.P., Segarra, P., Natale, M., 2017. Procedure for rock mass characterization with optical Televiewer. SLIM Technical Report;
- [User Guide OBI, 2017] User Guide: QL40 OBI-2G Optical Borehole Image. V17.03.03
- [Dips, 2020] Dips 2020. Rocscience Inc
- [ShapeMetrix 3D] ShapeMetriX 3S-SMX 2010. 3GSM (version 4.3);
- [FracMan, 2020] FracMan User manual – Geotechnical
- [AutoCAD, 2021] AutoCAD Map 3D 2021. Autodesk, Inc
- [Bernardini, 2020] Bernardini, 2020. ISBD definition from rock mass direct measurements
- Discontinuity characteristics in the rock mass (Hudson and Harrison 1997)
- Gomes, T., Segarra, P., Pérez Fortes, A.P., Xisheng, G., 2017. Procedure for rock mass characterization with photogrammetry. SLIM Technical Report;
- RockWorks 2016. RockWare – Earth Science & GIS Software. Golden, Colorado USA
- UShapeMetriX3D User Manual – 3D imaging for measuring and assessing rock and terrain surfaces, December 2010

- Barton, N. (1978). Suggested methods for the quantitative description of discontinuities in rock masses.

6 Sitography

- [Map,2021] https://satellite-map.gosur.com/it/italy/?gclid=Cj0K_CQiA7NKB_BhDBARIsAHbXCB4eN_z4Ua78dVe6dZtXs_2i8boCvW2nwzxmNe14ayJRxdFvBEkwVGoaAnGvEALw_wcB&ll=39.7760130_5721666,-3.8566740673043114&z=10.89587556974998&t=satellite
- [Arno,2020] <https://www.arno.es/es/arno-proyectos/cantera-el-aljibe/#>
- [Metamorphic, 2021] <http://www.alexstrekeisen.it/english/meta/amphibolite.php>
- [SfM, 2021] heia-sfm.org 2016. Structure from Motion (SfM) — Theia Vision Library. [online]
- <http://unica2.unica.it/antoniofunedda/9-Proiezioni.pdf>
- <https://www.pconti.net/doc/Stereogrammi.pdf>
- https://books.google.es/books?id=4Gd7Hg2tz-sC&pg=PA27&lpg=PA27&dq=four+type+of+stereographic+projection+slope&source=bl&ots=CV0K0I9gWa&sig=ACfU3U3RXGVWg045bQ3W3zFdrvA89zzlcQ&hl=it&sa=X&ved=2ahUKEwj-14Ge5oPqAhUN_RQKHRD0Co8Q6AEwDHoECAoQAQ#v=onepage&q&f=false
- <https://www.rockware.com/product/rockworks/>
- <https://www.geamap.com/it/geologicoespana>

Appendix A

(P_{21} calculated)

Values of P_{21} for each set of families in each campaign were calculated previously for each set of each highwall.

Table 27: All values of P_{21} Analysis.

first campaing				
	SH	SHNE	SVSE	SVNE
Object	Blast_1_1	Blast_1_1	Blast_1_1	Blast_1_1
Trace length(m)	294.07127	19.940022	32.419329	54.243828
Total area (m2)	528.15907	528.15907	528.15907	528.15907
Total P_{21}(1/m)	0.55678541	0.037753819	0.061381751	0.10270358
Object	Blast_2_1	Blast_2_1	Blast_2_1	Blast_2_1
Total Length (m)	252.80822	17.341532	23.393653	12.046106
Total Area (m2)	455.85086	455.85086	455.85086	455.85086
Total P_{21} (1/m)	0.55458538	0.038042116	0.051318655	0.026425542
Object	Blast_3_1	Blast_3_1	Blast_3_1	Blast_3_1
Total Length (m)	220.42833	11.189899	33.487238	20.612392
Total Area (m2)	413.67531	413.67531	413.67531	413.67531
Total P_{21} (1/m)	0.53285349	0.027049957	0.080950536	0.049827465
Object	Blast_4_1	Blast_4_1	Blast_4_1	Blast_4_1
Total Length (m)	195.68819	16.116501	16.976931	36.941812
Total Area (m2)	402.14474	402.14474	402.14474	402.14474
Total P_{21} (1/m)	0.48661135	0.040076368	0.042215971	0.091861979
Object	Blast_5_1	Blast_5_1	Blast_5_1	Blast_5_1
Total Length (m)	212.19729	11.074628	26.344894	47.027094
Total Area (m2)	423.68388	423.68388	423.68388	423.68388
Total P_{21} (1/m)	0.50083871	0.026138895	0.062180544	0.11099571
Object	Blast_6_1	Blast_6_1	Blast_6_1	Blast_6_1
Total Length (m)	193.65151	5.0730366	28.018529	51.56661

Total Area (m2)	332.36057	332.36057	332.36057	332.36057
Total P₂₁ (1/m)	0.58265488	0.015263653	0.084301603	0.15515261
Second campaign				
	SH	SHNE	SVSE	SVNE
Object	Blast_7	Blast_7	Blast_7	Blast_7
Total Length (m)	180.13016	17.78721	37.457419	64.504321
Total Area (m2)	461.37476	461.37476	461.37476	461.37476
Total P₂₁ (1/m)	0.3904205	0.038552628	0.081186536	0.13980895
Object	BLAST_8	BLAST_8	BLAST_8	BLAST_8
Total Length (m)	163.83006	13.032465	2.4268061	53.746094
Total Area (m2)	462.61568	462.61568	462.61568	462.61568
Total P₂₁ (1/m)	0.35413857	0.028171256	0.005245836	0.11617871
Object	BLAST_9	BLAST_9	BLAST_9	BLAST_9
Total Length (m)	318.58009	29.066201	30.020571	42.964497
Total Area (m2)	405.08209	405.08209	405.08209	405.08209
Total P₂₁ (1/m)	0.7864581	0.071753852	0.074109845	0.10606368
Object	BLAST_10	BLAST_10	BLAST_10	BLAST_10
Total Length (m)	197.68185	16.116222	62.515741	89.178926
Total Area (m2)	481.339	481.339	481.339	481.339
Total P₂₁ (1/m)	0.41069153	0.033482061	0.12987882	0.1852726
Object	BLAST_11	BLAST_11	BLAST_11	BLAST_11
Total Length (m)	139.17794	1.1018006	30.424889	42.071324
Total Area (m2)	513.58867	513.58867	513.58867	513.58867
Total P₂₁ (1/m)	0.27099106	0.002145298	0.059239798	0.081916379
Object	BLAST_12	BLAST_12	BLAST_12	BLAST_12
Total Length (m)	199.11272	13.375253	38.566873	55.527526
Total Area (m2)	391.94778	391.94778	391.94778	391.94778
Total P₂₁ (1/m)	0.50800829	0.034125088	0.098397988	0.14167072

P₁₀ (calculated)

The P₁₀ values calculated for each borehole were previously calculated for each borehole.

Table 28: All values of P_{10} analysis.

P₁₀	SH	SHNE	SVSE	SVNE
1B1	1.538461538	0.512821	1.367521	0.940171
1B2	1.008403361	0.084034	1.848739	1.344538
1B3	1.694915254	0.423729	1.440678	1.186441
1B4	2.393162393	0.769231	1.025641	0.512821
1B5	2.368421053	0.438596	2.192982	1.052632
1B7	2.231404959	0.330579	1.404959	1.735537
2B1A	1.052631579	0.478469	1.148325	0.574163
2B3A	1.061946903	0.619469	1.327434	0.619469
2B4A	2.090909091	0.636364	1.090909	1
2B5A	0.959860384	0.26178	1.832461	0.17452
2B6A	1.545454545	0.818182	2.272727	0.454545
2B7A	1.949152542	0.084746	2.033898	0.847458
4B2	0.241935484		1.370968	0.887097
4B3	0.403225806	0.080645	0.806452	0.806452
4B4	0.403225806	0.403226	1.532258	0.241935
4B5	0.16	0.56	1.12	0.72
4B6	0.885668277	0.322061	1.851852	0.724638
5B2	0.833333333	0.333333	1	0.416667
5B3	0.403225806	0.564516	1.048387	0.403226
5B4	0.327868852	0.163934	1.065574	0.409836
5B5	0.642570281	0.160643	0.963855	0.401606
5B6	0.8	0.16	1.92	0.48
6B1			1.127214	0.402576
6B2	0.241935484	0.403226	1.129032	0.483871
6B3	0.24291498		0.404858	0.647773

7B2	0.505050505	0.10101	1.212121	1.010101
7B3	0.224719101	0.074906	0.674157	0.674157
7B4	3.884892086	1.510791	1.726619	3.165468
7B5	2.413793103	1.206897	2.327586	2.068966
7B6	2.212765957	1.276596	2.042553	1.957447
8B2	1.96969697	1.515152	1.742424	2.045455
8B3	2.264150943	0.754717	0.830189	2.867925
8B4	2.064220183	0.993884	1.376147	2.905199
8B5	1.908396947	0.839695	2.290076	1.984733
8B6	1.596958175	0.456274	1.673004	0.988593
9B1	2.589285714	2.678571	2.946429	2.767857
9B2	0.948275862	1.206897	2.586207	0.948276
9B3	1.974248927	1.287554	2.145923	1.974249
9B4	2.666666667	1.75	2	1.75
9B6	5	3.088235	1.470588	1.323529
10B2	0.606060606	0.151515	1.666667	1.060606
10B3	0.827067669	0.150376	1.804511	1.954887
10B4	1.048689139	0.299625	1.273408	1.198502
10B6	0.707070707	0.10101	1.818182	0.505051
10B7	0.858369099		1.802575	1.030043
11B2	2.307692308	0.940171	0.940171	0.854701
11B3	1.138211382	0.650407	2.601626	1.544715
11B4	1.796875	0.46875	1.484375	1.40625
11B5	2.095238095	1.904762	2.190476	2.380952
11B6	1.473684211	0.947368	2.105263	3.052632
11B7	1.447963801	1.357466	3.076923	1.900452
12B2	1.307692308	0.153846	1.230769	1.461538

12B3	1.317829457	0.155039	1.24031	1.317829
12B4	0.778210117	0.311284	1.167315	1.400778
12B5	0.916666667		1.416667	1.666667
12B6	0.916666667	0.25	0.916667	1.583333
12B7	0.310077519	0.155039	1.860465	2.093023

Spacing (calculated)

Average spacing values were calculated by calculating the spacing for each hole.

Table 29: All values of spacing analysis.

Spacing m/n	SH	SHNE	SVSE	SVNE
1B1	0.61353	2.086	0.695333	1.043
1B2	0.97818		0.512381	0.717333
1B3	0.57	2.7075	0.676875	0.833077
1B4	0.3863	1.30375	0.948182	2.086
1B5	0.39654	2.5775	0.429583	0.937273
1B7	0.41808	3.623333	0.679375	0.5435
2B1A	0.892	2.23	0.810909	1.784
2B3A	0.85636	1.57	0.672857	1.57
2B4A	0.43136	1.581667	0.862727	0.949
2B5A	0.912	4.56	0.456	9.12
2B6A	0.59188	1.18375	0.394583	2.3675
2B7A	0.48136		0.460435	1.176667
4B2	5.41		0.67625	1.082
4B3	2.7125		1.205556	1.205556
4B4	2.77	2.77	0.615556	5.54
4B5	10.81	1.801667	0.831538	1.35125
4B6	1.111	3.703333	0.505	1.38875
5B2	1.15222	3.456667	0.942727	2.5925

5B3	2.6925	1.795	0.8975	2.6925
5B4	3.58333	10.75	0.895833	2.6875
5B5	1.54286	10.8	0.981818	2.7
5B6	1.16667	10.5	0.456522	2.1
6B1			0.826923	2.6875
6B2	4.9	2.45	0.753846	1.96
6B3	4.98		2.49	1.422857
7B2	2.155		0.783636	0.957778
7B3	5.645		1.41125	1.41125
7B4	0.24491	0.649	0.564348	0.30186
7B5	0.3737	0.776154	0.388077	0.438696
7B6	0.4252	0.759286	0.462174	0.483182
8B2	0.4624	0.608421	0.525455	0.444615
8B3	0.40759	1.313333	1.182	0.319459
8B4	0.44885	0.9725	0.686471	0.315405
8B5	0.48917	1.174	0.404828	0.4696
8B6	0.575	2.3	0.547619	0.958333
9B1	0.34786	0.335862	0.304375	0.324667
9B2	0.999	0.768462	0.344483	0.999
9B3	0.47636	0.748571	0.436667	0.476364
9B4	0.33774	0.5235	0.455217	0.5235
9B6	0.16121	0.266	0.591111	0.665
10B2	1.54667		0.464	0.773333
10B3	1.101	11.01	0.478696	0.4404
10B4	0.89923	3.896667	0.730625	0.779333
10B6	1.19		0.42	1.785
10B7	1.10333		0.4965	0.902727
11B2	0.39923	1.038	1.038	1.153333
11B3	0.87692	1.628571	0.367742	0.633333
11B4	0.52636	2.316	0.643333	0.681176

11B5	0.43714	0.483158	0.417273	0.3825
11B6	0.57385	0.9325	0.392632	0.266429
11B7	0.578	0.619286	0.262727	0.4335
12B2	0.70938	11.35	0.756667	0.630556
12B3	0.68938	11.03	0.735333	0.689375
12B4	1.29	3.87	0.829286	0.682941
12B5	0.99		0.61875	0.521053
12B6	1.001	5.005	1.001	0.556111
12B7	3.81333	11.44	0.497391	0.44

Appendix B

➤ First campaign

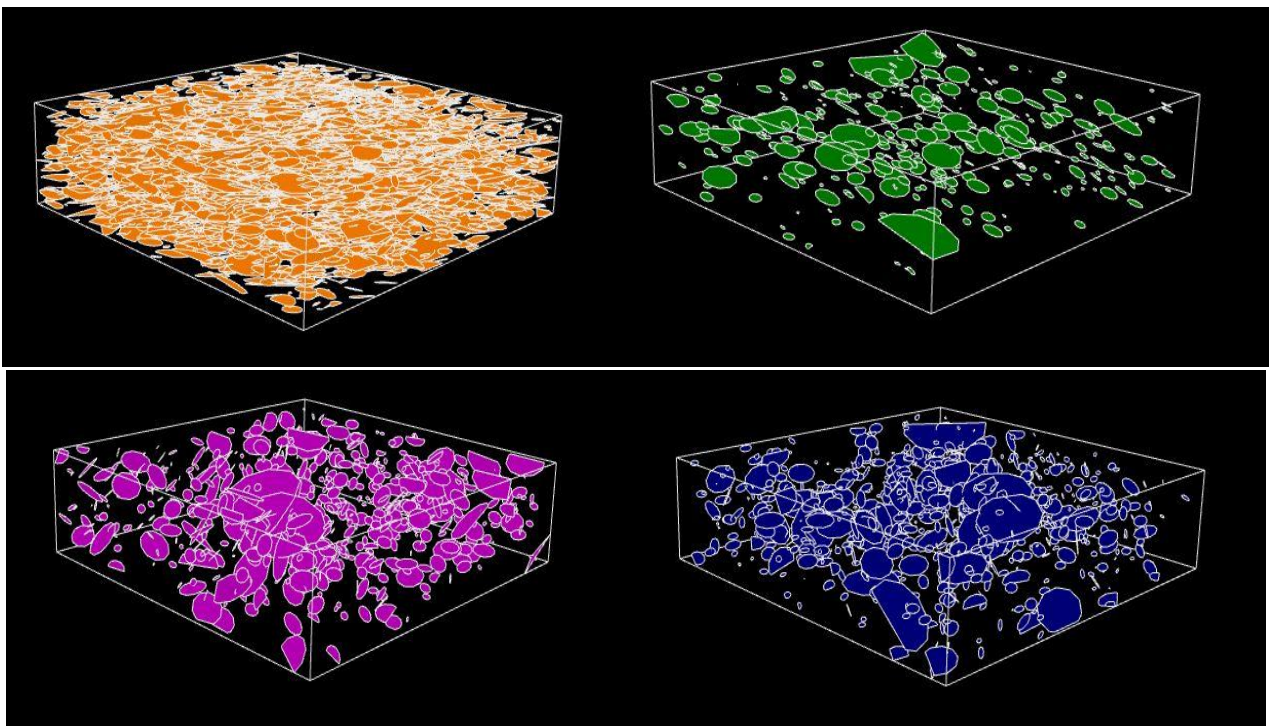


Figure 86: Fracture simulation with P_{21} values (From top left to bottom right: Sh, ShNE, SvSE, SvNE).

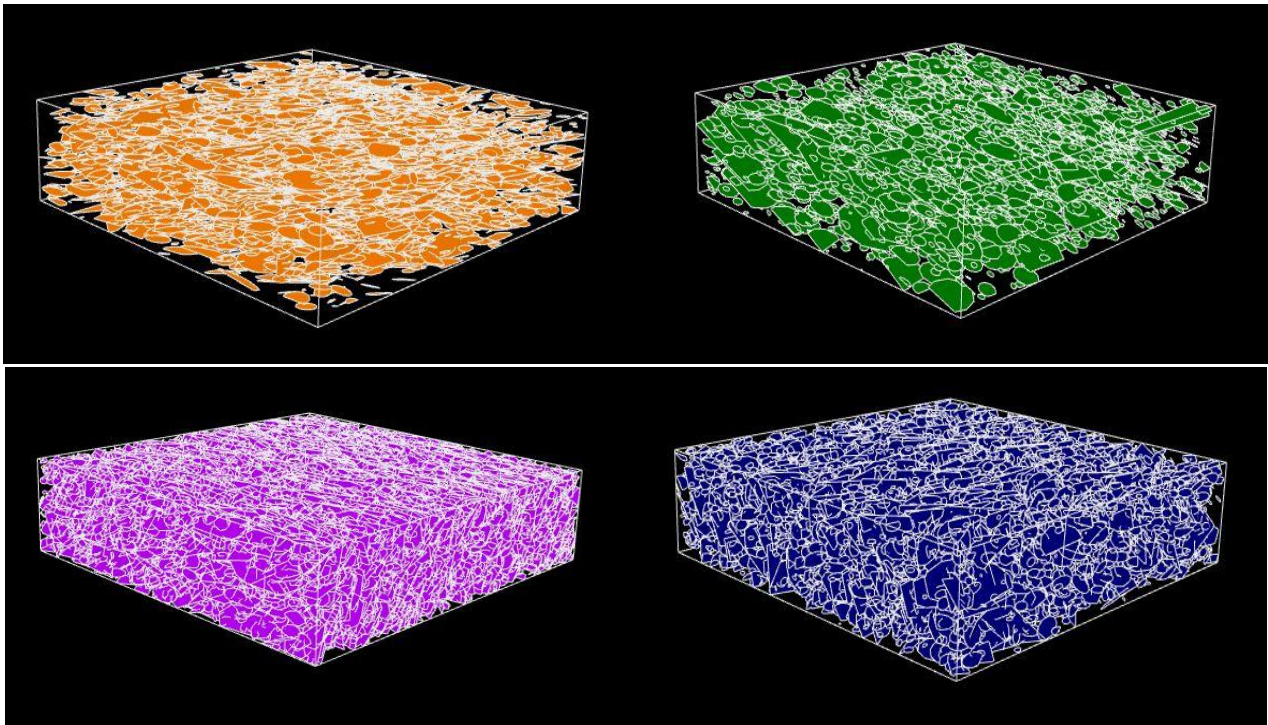


Figure 87: Fracture simulation with P_{10} values (From top left to bottom right: Sh, ShNE, SvSE, SvNE).

➤ Second campaign

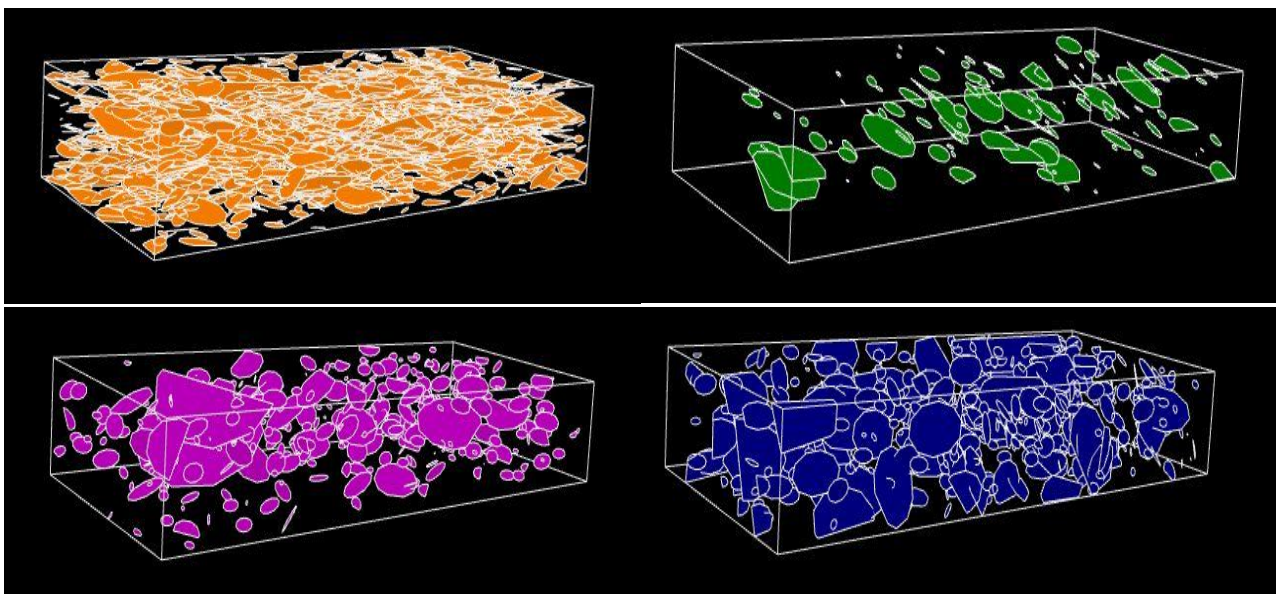


Figure 88: Fracture simulation with P_{21} values (From top left to bottom right: Sh, ShNE, SvSE, SvNE).

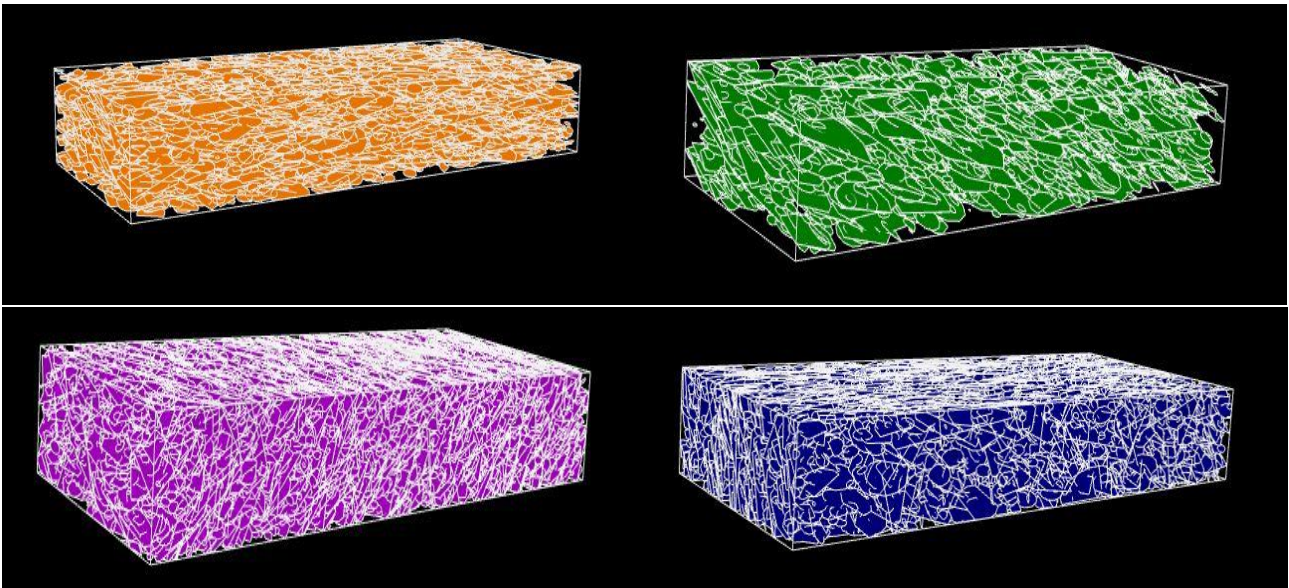


Figure 91: Fracture simulation with P_{10} values (From top left to bottom right: Sh, ShNE, SvSE, SvNE).